RARE NONLEPTONIC DECAYS OF THE OMEGA HYPERON: MEASUREMENTS OF THE BRANCHING RATIOS FOR $\Omega^{\mp} \to \Xi^{*0}_{1530}(\overline{\Xi^{*0}_{1530}})\pi^{\mp}$ AND $\Omega^{\mp} \to \Xi^{\mp}\pi^{\pm}\pi^{\mp}$

BY

OLEG KAMAEV

Submitted in partial fulfillment of the
requirements for the degree of
Doctor of Philosophy in Physics
in the Graduate College of the
Illinois Institute of Technology

Approved _____
Advisor

Chicago, Illinois
December 2007

ACKNOWLEDGMENT

First of all, I would like to thank Nick Solomey for inspiring me to look at the rare decays of the Ω hyperon and Dan Kaplan for continuous support and encouragement over the last three years. Dan shared with me a lot of his bright ideas about analysis improvements and also showed me how to write with proper style. I am grateful to Chris White for his important comments about my analysis and his patience while I was a teaching assistant for his class during my first semester at IIT and was accommodating to a different cultural environment. I also would like to thank the other members of the high energy physics group at IIT, in particular, Howie Rubin for his continuous attention towards my work, Yagmur Torun, and Jeff deJong for many interesting discussions.

This thesis would not have been possible without the data from the HyperCP experiment. I acknowledge all HyperCP collaborators and Fermilab staff for constructing and running the experiment. I would like to thank Craig Dukes, Kam-Biu Luk, Mike Longo, Piotr Zyla, Lanchun Lu and Tim Holmstrom for their comments on and interest in my work. I especially thank Durga Rajaram for many stimulating discussions.

Special thanks go to all my fellow graduate students, in particular to Brandon Seilhan and Alex Weiss, for bringing a lot of fun into my life.

Last but not least, I thank my wife Liubov, my daughter Anna, and my parents for their support, encouragement and patience.

TABLE OF CONTENTS

LIST OF TABLES

LIST OF FIGURES

ABSTRACT

A clean signal of 78 (24) events has been observed in the rare nonleptonic particle (antiparticle) decay modes $\Omega^{\mp} \to \Xi^{\mp}\pi^{\pm}\pi^{\mp}$ using data collected with the HyperCP spectrometer during Fermilab's 1999 fixed-target run. We obtain $B(\Omega^- \to \Xi^-\pi^+\pi^-) = [4.32 \pm 0.56(\text{stat}) \pm 0.28(\text{syst})] \times 10^{-4}$ and $B(\Omega^+ \to \Xi^+\pi^-\pi^+) = [3.13 \pm 0.71(\text{stat}) \pm 0.20(\text{syst})] \times 10^{-4}$. This is the first observation of the antiparticle mode. Our measurement for the particle mode agrees with the previous experimental result and has an order-of-magnitude better precision. We extract the contribution from the resonance decay mode $\Omega^{\mp} \to \Xi^{*0}_{1530}(\overline{\Xi^{*0}_{1530}})\pi^{\mp}$ to the final state $\Xi^{\mp}\pi^{\pm}\pi^{\mp}$. This, the first actual measurement of the resonance-mode branching ratios, gives $B(\Omega^- \to \Xi^{*0}_{1530}\pi^-) = [4.55 \pm 2.33(\text{stat}) \pm 0.38(\text{syst})] \times 10^{-5}$, $B(\Omega^+ \to \overline{\Xi^{*0}_{1530}}\pi^+) = [1.40 \pm 2.83(\text{stat}) \pm 0.12(\text{syst})] \times 10^{-5}$ and disagrees with the current Particle Data Group review value, being ≈ 14 times smaller. Since the central value of the resonance-mode branching ratio is less than two standard deviations away from zero, we also calculate branching ratio upper limits at 90% confidence level: $B(\Omega^- \to \Xi^{*0}_{1530}\pi^-) < 7.61 \times 10^{-5}$ and $B(\Omega^+ \to \overline{\Xi^{*0}_{1530}}\pi^+) < 5.61 \times 10^{-5}$. This analysis provides new data on nonleptonic hyperon decays which allows studies of how weak interaction processes occur in the presence of strong interactions.

CHAPTER 1

INTRODUCTION

Elementary particle physics investigates what matter is made of on the fundamental level. Nonleptonic decays of the Ω (pronounced "o-mé-ga") hyperon might be among the most useful tools to probe the structure of the hadronic weak interactions.

The first section of this chapter provides the background, necessary for understanding the rest of the dissertation, and briefly describes the Standard Model. The second section explains what rare nonleptonic decays of the Ω hyperon are and presents our motivations for studying them. Theoretical predictions are summarized in the third section. Finally, the fourth section discusses existing experimental results and explains why we think that data collected by the HyperCP experiment are a good place to study the decays of interest.

1.1 Elementary Particle Physics and the Standard Model

Elementary particle physics studies matter and its interactions on the smallest scale. It is also often called high energy physics. To see an object, the wavelength of a probe (λ) must be comparable to or smaller than the size of the object. The relation between momentum (p) and λ is given by the de Broglie equation $\lambda = h/p$, where h is Planck's constant. For the typical beam particle momentum of hundreds of GeV/c, experiments in high energy physics act as nanonanoscale microscopes!

Today we know that the fundamental particles of the Universe are six quarks and six leptons. There is no evidence for sub-quarks or sub-leptons. There are four forces in nature. Listed in descending order by strength, they are strong, electromagnetic, weak, and gravity. The strength of an interaction should be thought of as a probability for this interaction to occur, rather than the actual strength in classical physics. Fundamental particles are fermions, whereas carriers of the forces are bosons.

There are hundreds of observed elementary particles. Particles can be classified into hadrons and leptons. Hadrons participate in all four interactions, while leptons interact through the electromagnetic (except neutrinos), weak, and gravitational forces, but not the strong force. Hadrons can be further classified into baryons and mesons. Baryons are fermions that consist of three valence quarks in either qqq or $\overline{qqq}$ combinations. Mesons are bosons that consist of two valence quarks in a $q\bar{q}$ combination. Decay properties of quarks inside a hadron are greatly influenced by the strong force between quarks, in spite of the fact that "free" quarks decay via the weak force. Each particle has its corresponding antiparticle with the same mass and spin, but with other quantum numbers opposite.

Almost all of our current knowledge about elementary particles can fit into the Standard Model. It was extremely successful in predicting the $W^{\pm}$ and Z bosons, the top quark and the charm quark before they were observed. During my years of graduate study in elementary particle physics, I attended dozens of talks where results probing the Standard Model, primarily from collider experiments, were reported. I was always fascinated by how accurately experiment agrees with theory. However, the Standard Model is not a complete theory of fundamental interactions. One of the main problems is that it does not include gravity. The observed nonzero neutrino mass is another pitfall. In addition, values for many parameters are put into the Standard Model and are not derived from first principles.

Quarks and leptons are grouped into generations:

$$\begin{pmatrix} u \\ d \end{pmatrix} \quad \begin{pmatrix} c \\ s \end{pmatrix} \quad \begin{pmatrix} t \\ b \end{pmatrix}, \quad \begin{pmatrix} e \\ \nu_e \end{pmatrix} \quad \begin{pmatrix} \mu \\ \nu_\mu \end{pmatrix} \quad \begin{pmatrix} \tau \\ \nu_\tau \end{pmatrix}.$$

Quarks carry fractional electric charges of $+2/3|e|$ and $-1/3|e|$, while the leptons carry integral electric charges, 0 or $\pm|e|$. The quark mass eigenstates differ from the quark weak eigenstates. The relation between the two sets of eigenstates is given by

the Cabibbo-Kobayashi-Maskawa (CKM) quark-mixing matrix:

$$\begin{pmatrix} d' \\ s' \\ b' \end{pmatrix} = \mathrm{V_{CKM}} \begin{pmatrix} d \\ s \\ b \end{pmatrix}$$

where primed (nonprimed) quarks correspond to the weak (mass) eigenstates. The CKM matrix is a 3×3 unitary matrix with four parameters. At the 90% confidence level, its experimentally measured values are [32][1]

$$\mathrm{V_{CKM}} = \begin{pmatrix} 0.9739 \text{ to } 0.9751 & 0.221 \text{ to } 0.227 & 0.0029 \text{ to } 0.0045 \\ 0.221 \text{ to } 0.227 & 0.9730 \text{ to } 0.9744 & 0.039 \text{ to } 0.044 \\ 0.0048 \text{ to } 0.014 & 0.037 \text{ to } 0.043 & 0.9990 \text{ to } 0.9992 \end{pmatrix}.$$

For example, according to these values, the u-quark is more likely to convert to the d-quark, but has nonzero coupling to the s-quark as well. It very rarely converts to the b-quark. The matrix can be described by four real parameters, i.e., three angles and one phase. In the Kobayashi-Maskawa theory the nonzero phase value is responsible for the observed CP violation in the K and B meson systems. For leptons, the analog of the CKM matrix is the Pontecorvo-Maki-Nakagawa-Sakata matrix.

1.1.1 Experimental observables. In high energy physics new particles or bound states are produced either by a beam of accelerated particles interacting with a stationary target (fixed-target experiments) or by two beams of accelerated particles flying in opposite directions and colliding (collider experiments). To describe the scattering of a particle, experimentalists measure a cross section. If a new particle is created after the collision, it can be described by the measurement of its quantum

[1]Corresponding to references in the Bibliography.

numbers, e.g., spin, parity, etc. Then, typically, the particle decays and one can measure its lifetime.

The scattering cross section and inverse mean lifetime of a particle are proportional to the square of the amplitude for the process (matrix element) and the available phase space. An amplitude can be calculated by evaluating the corresponding Feynman diagrams. The phase space depends on the four-momenta of the participating particles.

Often, instead of lifetime, high energy physicists use decay rate (Γ), which is the probability per unit time that any given particle of this sort will disintegrate. Decay rate is the reciprocal of mean lifetime: $\Gamma = 1/\tau$. Typically, a particle can decay via different paths each with its own decay rate. The total decay rate is the sum of the individual decay rates, i.e., $\Gamma = \sum_{i=1}^{n} \Gamma_i$. Each decay path is described by the branching ratio which is the ratio of the individual decay rate to the total, i.e., $B_i = \Gamma_i/\Gamma$. In other words, the branching ratio for the ith decay mode is the probability that the particle will decay via the ith path.

More detailed information about elementary particle physics and the Standard Model at the introductory level can be found, for example, in [13] and [24].

1.2 Rare Nonleptonic Decays of the Ω Hyperon

Hyperons are baryons with at least one strange quark, but without charm, bottom, and top quarks. The Ω hyperon consists of three strange quarks (sss) and is thus ideal for studying strange-quark decay properties. Any Ω decay requires a change in the strangeness quantum number, which can happen only through the weak interaction. In spite of the fact that the weak interaction is well understood, the decay properties of strange quarks inside hadrons are not. Experimental measurements of hyperon decay properties, together with the corresponding theoretical calculations,

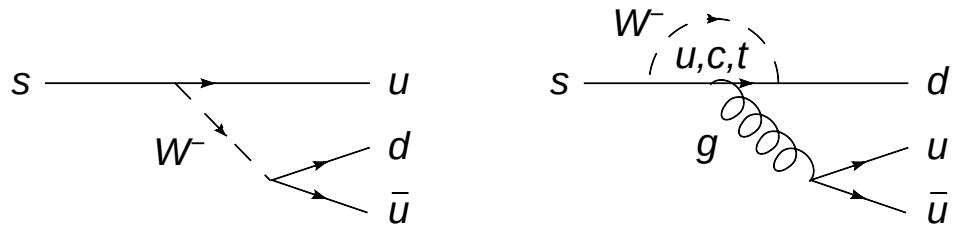

Figure 1.1. Tree-level (left graph) and penguin (right graph) Feynman diagrams for the nonleptonic weak decays $\Omega^- \to \Lambda K^-$ and $\Omega^- \to \Xi^{*0}_{1530}\pi^-$.

can shed light on the subject.

We study how the strong interaction influences weak decays, and it is preferable not to have leptons among the decay products. Thus, we need to study nonleptonic decays. As emphasized by D. Wu and J. L. Rosner [31], nonleptonic decays of hyperons are essential for the study of how weak interaction processes occur in the presence of strong interactions.

The dominant decay mode for the Ω hyperon is

$$\Omega^{\mp} \to \Lambda(\overline{\Lambda})K^{\mp} \tag{1.1}$$

with branching ratio equal to 0.678 ± 0.007. The basic Feynman diagrams for this mode are shown in Figure 1.1. The strange (s) quark in the parent hyperon converts into an up (u) or down (d) quark. This involves the "tree-level" diagram for the former and the "penguin-type" diagram for the latter case. The "W" and "Z" are charged and neutral vector bosons, respectively. They are carriers of the weak force. The "g" is the gluon, which is a carrier of the strong force. This decay mode has been extensively studied over the last 40 years. The Ω decay properties, including the branching ratio and a parity-violation parameter, have been measured to great precision [32].

Rare decay modes, in contrast to the dominant mode, have much smaller branching ratios and are thus harder to study, primarily because of their smaller

Table 1.1. Particle properties.

Particle	Quark content	Spin	P-parity	Isospin	G-parity
Ω^-	sss	1.5	+1	0	–
Ξ^{*0}_{1530}	uss	1.5	+1	0.5	–
Ξ^{*-}_{1530}	dss	1.5	+1	0.5	–
Ξ^-	dss	0.5	+1	0.5	–
Ξ^0	uss	0.5	+1	0.5	–
π^+	$u\overline{d}$	0	−1	1	−1
π^-	$\overline{u}d$	0	−1	1	−1
π^0	$(u\overline{u} - d\overline{d})/\sqrt{2}$	0	−1	1	−1

event samples. They have potential to provide new information in an area where the knowledge is sparse. Moreover, studies of rare phenomena can bring intriguing surprises along the way. That is why we are highly motivated to examine rare nonleptonic decays of the Ω hyperon.

The following rare nonleptonic modes are allowed by the energy, charge, and baryon number conservation laws:

$$\begin{aligned}
\Omega^- &\rightarrow \Xi^{*0}_{1530}\pi^- , \\
\Omega^- &\rightarrow \Xi^{*-}_{1530}\pi^0 , \\
\Omega^- &\rightarrow \Xi^-\pi^+\pi^- , \\
\Omega^- &\rightarrow \Xi^-\pi^0\pi^0 , \\
\Omega^- &\rightarrow \Xi^0\pi^0\pi^- ,
\end{aligned}$$

along with the corresponding antiparticle modes. We exclude second-order weak decays because their decay rates are predicted to be extremely small within the Standard Model. For example, it is predicted that $B(\Omega^- \rightarrow \Lambda\pi^-) \simeq 10^{-17}$ [14], which is in agreement with the most recent experimental upper limit of 2.9×10^{-6} [30]. Quark content and quantum numbers for the involved particles are given in Table 1.1.

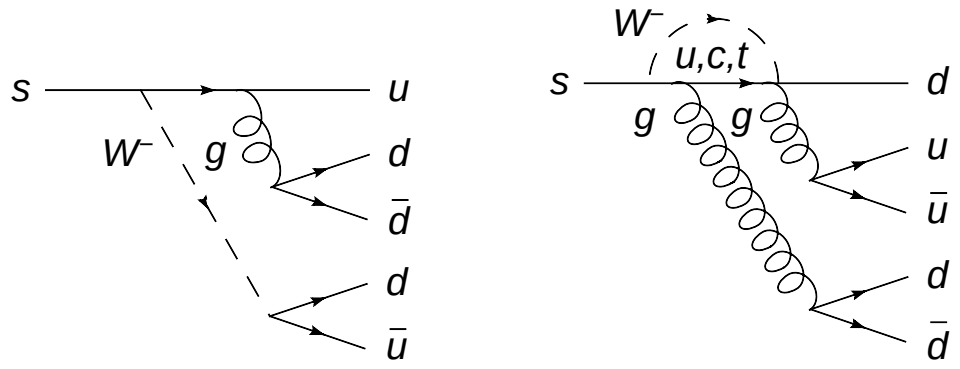

Figure 1.2. Tree-level (left graph) and penguin (right graph) Feynman diagrams for the nonleptonic weak decay $\Omega^- \to \Xi^-\pi^+\pi^-$.

The main decay mode of the π^0 is $\pi^0 \to \gamma\gamma$ which has the branching ratio of 0.98798 ± 0.00032 [32]. Anticipating the discussion in Section 2.1.13, I point out here that the HyperCP spectrometer was not designed to detect γ-particles and, consequently, reconstruction of π^0 particles was not efficient. Thus, there are two decays of interest to us:

$$\Omega^\mp \to \Xi^{*0}_{1530}(\overline{\Xi^{*0}_{1530}})\pi^\mp\,, \tag{1.2}$$

$$\Omega^\mp \to \Xi^\mp\pi^\pm\pi^\mp\,. \tag{1.3}$$

The basic Feynman diagrams for the particle modes are given in Figure 1.1 and Figure 1.2 respectively. Strange quark conversion can occur purely at tree-level or can involve, in addition, a penguin-type diagram. We discuss the theoretical description for both modes in the next section.

1.3 Theoretical Predictions

Theory predicts the branching ratio $B(\Omega^- \to \Xi^{*0}(1530)\pi^-)$ to be at the 10^{-3} level [9, 10]. Since the Ξ^{*0}_{1530} is a resonance with $c\tau \approx 10^{-12}$ cm [32], it decays promptly via the strong force with $B(\Xi^{*0}_{1530} \to \Xi^-\pi^+) \simeq 2/3$, where the branching ratio is estimated from isospin considerations. The same final state can be reached directly through the 3-body decay channel (1.3). However, theorists expected that the final

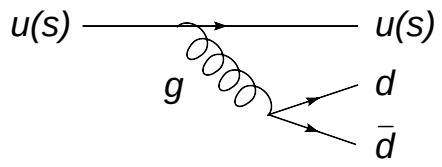

Figure 1.3. Feynman diagram for the strong decay $\Xi^{*0}_{1530} \to \Xi^-\pi^+$.

state $\Xi^-\pi^+\pi^-$ would be completely dominated by the Ξ^{*0}_{1530} intermediate state [9, 10]. This suggests a decay chain $\Omega^- \to \Xi^{*0}_{1530}\pi^- \to \Xi^-\pi^+\pi^-$ with a consequent direct relation between modes (1.2) and (1.3): $B(\Omega^- \to \Xi^{*0}_{1530}\pi^-) = 1.5B(\Omega^- \to \Xi^-\pi^+\pi^-)$.

One of the earliest calculations of Ω nonleptonic decay rates was done in the phenomenological chiral-Lagrangian model [12]. The decay amplitude for the mode (1.3) includes tree-level diagrams with (in the authors' notation) type-1 and type-2 weak vertices. Type-1 weak interaction involves two decuplet lines, while type-2 weak interaction involves a decuplet line and a baryon-octet line. Thus, only diagrams with type-1 vertices contribute to the decay amplitude of mode (1.2).

At the time of the paper [12], neither mode of interest had yet been observed. The type-1 weak interaction was thought to dominate and the rough estimate of the decay-rate ratio yielded

$$R = \frac{\Gamma(\Omega \to \Xi\pi\pi)}{\Gamma(\Omega \to \Lambda K)} \simeq \frac{\Gamma(\Omega \to \Xi^{*0}_{1530}\pi)}{\Gamma(\Omega \to \Lambda K)} \simeq 0.05\,. \tag{1.4}$$

It was stated that if R turned out to be much smaller than this, it could mean that the type-1 weak interaction was very small in comparison to the type-2. Consequently, it was an open possibility that the final state $\Xi^-\pi^+\pi^-$ could be created directly, without the formation of the Ξ^{*0}_{1530} intermediate state.

A standard QCD-inspired description was examined in [10]. It was assumed that the decay proceeds through the resonance channel (1.2), "as suggested by the data" from [2], where a search for $\Omega^- \to \Xi^-\pi^+\pi^-$ had yielded one clear event with

a $\Xi^-\pi^+$ reconstructed invariant mass of 1533 MeV/c^2, close to the Ξ^{0*}_{1530} resonance mass. The prediction was

$$B(\Omega^- \to \Xi^{*0}_{1530}\pi^-) \simeq \frac{3}{1070} \simeq 2.8 \times 10^{-3}\,, \tag{1.5}$$

$$B(\Omega^- \to \Xi^-\pi^+\pi^-) = \frac{2}{3} B(\Omega^- \to \Xi^{*0}_{1530}\pi^-)\,. \tag{1.6}$$

Due to its relative simplicity, the rare nonleptonic hyperon 2-body decay (1.2) continues to attract theorists' attention. Recently, an attempt to estimate the branching ratio with an effective weak Hamiltonian in the SU(3) Skyrme model was made [9]. The work was stimulated by the results from the HyperCP experiment [29]. The calculated decay rate depends on the value of the Skyrme charge and strength of the QCD correction contribution. The prediction closest to the existing experimental data gives

$$B(\Omega^- \to \Xi^{*0}_{1530}\pi^-) = 8.58 \times 10^{-4}\,. \tag{1.7}$$

Lately, our reported preliminary results [16] have motivated theorists to revisit decays (1.2) and (1.3) yet again [1]. Derivations were performed within heavy-baryon chiral perturbation theory (χPT). At leading order, the decay (1.3) is completely dominated by the Ξ^{*0}_{1530} state with estimated $B(\Omega^- \to \Xi^-\pi^+\pi^-) = (6.5 \pm 4.1) \times 10^{-3}$. This, to a considerable extent, reproduces earlier theoretical results and is an order of magnitude larger than experimental results. However, at next-to-leading order, it is possible to soften the Ξ^{*0}_{1530} dominance and lower the $\Omega^- \to \Xi^-\pi^+\pi^-$ branching ratio.

1.4 Experimental Results

The current Particle Data Group (PDG) [32] branching ratio is based on the four observed events [3] and for each mode is:

$$B(\Omega^- \to \Xi^{*0}_{1530}\pi^-) \;\; = \;\; (6.4^{+5.1}_{-2.0}) \times 10^{-4}\,,$$

$$B(\Omega^- \to \Xi^-\pi^+\pi^-) \;=\; (4.3^{+3.4}_{-1.3}) \times 10^{-4}\,.$$

The experiment [2, 3] had neither the statistics nor sufficient momentum resolution to distinguish between these two mechanisms; that is why the same four events were used to calculate the branching ratio for each process. The current PDG resonance-channel (1.2) branching ratio was deduced using the branching ratio of 2/3 for $\Xi^{*0}_{1530} \to \Xi^-\pi^+$ and by the assumption that the four events are $\Omega^- \to \Xi^{*0}_{1530}\pi^-$. It is thus not necessarily trustworthy.

Preliminary analysis of the HyperCP data set gave $B(\Omega^- \to \Xi^-\pi^+\pi^-) = (3.56 \pm 0.33(\text{ stat})) \times 10^{-4}$ and is based on 137 events [29]. However, it was done for the 3-body decay mode (1.3) only, without numerical estimation of the resonance decay channel contribution to the final state.

Using the HyperCP data sample — currently the world's largest hyperon sample, with $\sim 10^{10}$ hyperon decays, including $\sim 10^7$ total Ω decays — we are able to measure the branching ratio for the resonance decay mode and to understand what (if anything) resonance decays could be contributing to the $\Omega^- \to \Xi^-\pi^+\pi^-$ branching ratio. The unclear theoretical situation together with the poor existing experimental data [32] bring additional motivation towards investigating the resonance-mode decay (1.2) and the three-body decay channel (1.3).

CHAPTER 2
HYPERCP EXPERIMENT

2.1 Spectrometer Overview

The HyperCP experiment (FNAL E871) was a fixed-target experiment at the Fermi National Accelerator Laboratory (FNAL or Fermilab) in Batavia, Illinois. It took data in 1996–1997 and 1999–2000. Data from the 1999–2000 run were used in this analysis. Thus, we will describe the spectrometer as it existed in 1999–2000.

The full description of the HyperCP spectrometer may be found elsewhere [4]. Figure 2.1 shows schematic representations of the elevation and plan views of the HyperCP spectrometer. In a nutshell, the 800 GeV/c primary proton beam interacted with a copper target and created various particles such as muons, pions, kaons, Ξ, Ω, and others. Secondary beam rate and position were monitored by the beam hodoscope. The hyperon magnet and collimator performed momentum selection of charged secondary particles and directed them into the spectrometer. The particles then passed into the vacuum decay region. Event reconstruction was performed in three dimensions using a series of multiwire proportional chambers (MWPCs) arrayed on both sides of the Analyzing Magnets. The hodoscopes and the calorimeter served as the main trigger elements for data acquisition. Muon stations were used to identify and reconstruct muon tracks.

To switch from particle to antiparticle decay modes, one needed to reverse the magnetic field directions in both the Hyperon and Analyzing Magnets. This reduced many systematic differences between particle and antiparticle runs and was essential for CP-violation parameter measurement. Particles with the same (opposite) charge as the primary secondary-beam particles were deflected by the Analyzing Magnets to the spectrometer side that was called "same-sign" ("opposite-sign"). This nota-

tion makes the spectrometer description equally correct for particle and antiparticle modes.

2.1.1 Beam Description. Primary protons were accelerated to 800 GeV/c in the Fermilab Tevatron. A small fraction of them, less than 4%, were sent to the Meson Center beamline, where the experiment was located. Beam was delivered in a 40-second spill with a 40-second interspill (no beam) period. Approximately 3×10^{11} protons hit the target during each cycle.

Primary beam position and shape were measured with eight segmented-wire ion chambers (SWICs). Each SWIC had one vertical and one horizontal plane of wires. The two SWICs closest to the target had 0.5 mm wire pitch, whereas the others had 1.0 mm. The shape of the beam at the target was approximately Gaussian with $\sigma_x = 0.45 \pm 0.08$ mm and $\sigma_y = 0.38 \pm 0.08$ mm. For all data used in this analysis, the beam was centered on a line that went through the target and the center of the collimator entrance.

2.1.2 Target. Two targets, identical except for their length, were used. To produce negative (positive) secondary beam, the copper target of 60 mm (20 mm) length was secured in a target holder. Different lengths were necessary to get comparable secondary beam intensities for both polarities. Target transverse dimensions were 2 mm $\times$ 2 mm. A remotely controlled precision manipulator could move the target holder in the vertical and horizontal directions. The target center was lined up with the center of the collimator entrance.

2.1.3 Hyperon Magnet. The Hyperon Magnet was an 11455 kg, 6.071 m long dipole magnet built at Fermilab for the "Main Ring" accelerator. The field of 1.667 T was oriented in the horizontal direction. The magnetic field was monitored by two Hall probes and was found to be very stable.

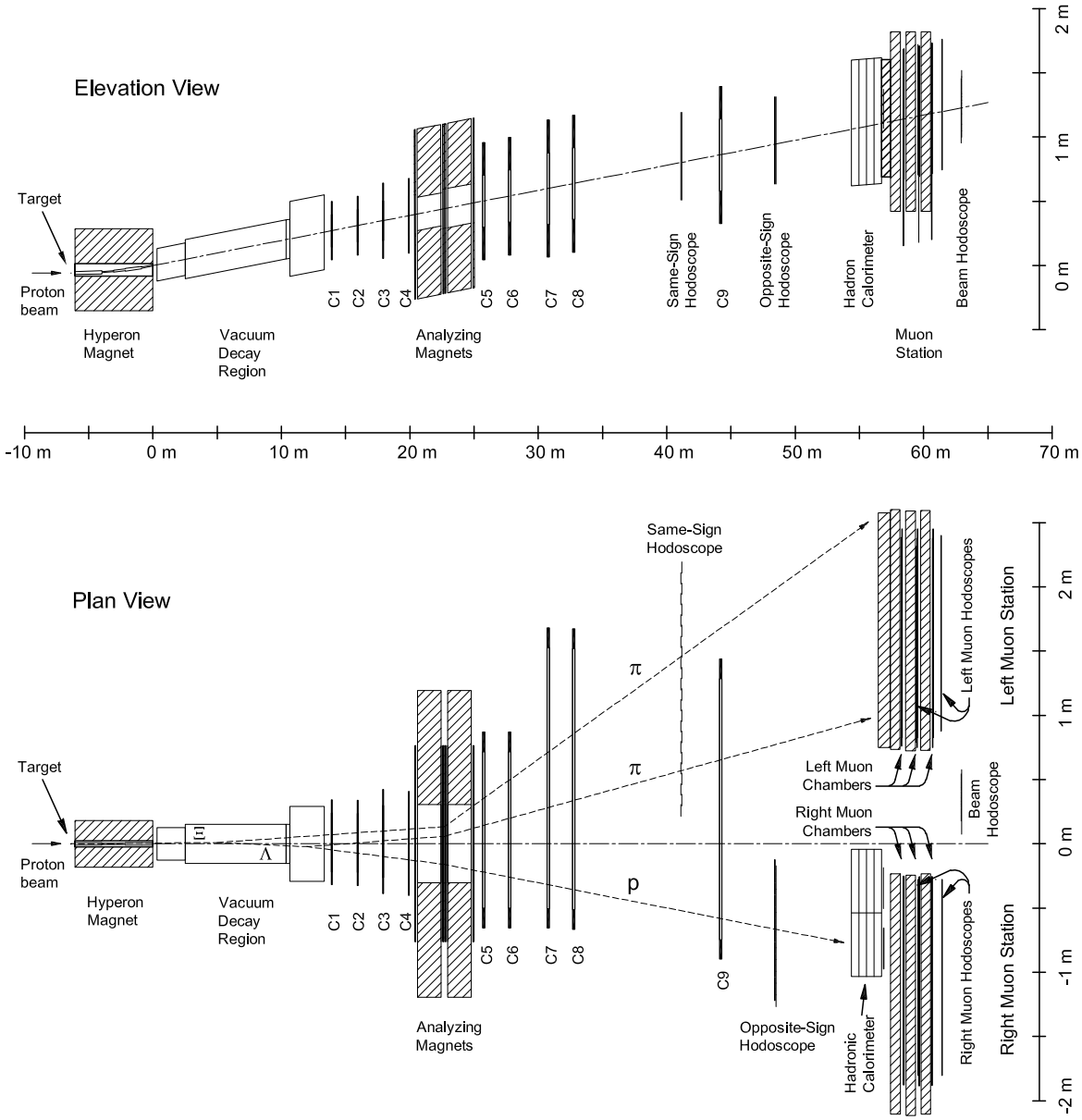

Figure 2.1. Elevation and plan views of the HyperCP spectrometer.

A 6.096 m long collimator was installed within the Hyperon Magnet. The collimator was made of five segments. Each segment was a block of brass or tungsten with the curved channel inside. Secondary beam particles from the target were deflected into the collimator channel by the Hyperon Magnet. A particle with a trajectory along the center of the collimator channel entered the collimator at zero horizontal angle and exited at an angle of 19.51 mrad above the horizontal. The central-orbit momentum for the Hyperon Magnet field was 156.2 GeV/c. The charge of the secondary beam was changed by reversing the Hyperon Magnet field direction.

The collimator and Hyperon Magnet served as the dump for neutral and off-momentum charged secondary beam particles and for primary-beam protons that did not interact in the target. To reduce radiation, the entire assembly was enclosed in massive iron and concrete shielding.

2.1.4 Decay region. A decay pipe was situated downstream of the collimator. It consisted of three joined cylindrical tubes and was 13 m long. Monte Carlo simulations had shown that most of the decays of interest occurred completely inside the pipe. To eliminate multiple scattering and interactions with matter, the pipe was evacuated.

2.1.5 Analyzing Magnets. Charged particles were deflected in the x-z plane while passing through the apertures of a pair of dipole magnets, which were called the Analyzing Magnets. The aperture dimensions of the first (upstream) magnet were 61.0 cm (width) by 25.9 cm (height). A field of 1.345 T (1.136 T) was produced in the vertical direction by the upstream (downstream) magnet. The magnetic fields were found to be quite stable. The rms deviation of all spills was 4.3 G (4.7 G) for the upstream (downstream) magnet. The combined kick to the transverse momentum of charged particles passing through the magnet was 1.43 GeV/c, and hence, sufficiently downstream of the Analyzing Magnets, decay products were well separated from the secondary beam.

When the charge of the secondary beam was reversed by reversing the direction of the Hyperon Magnet field, the direction of the magnetic field in the Analyzing Magnets was also reversed. To achieve equal acceptances for hyperon and antihyperon decays and to minimize potential biases in the CP-violation analysis, it was essential to have the same magnetic field magnitudes for positive and negative secondary beam runs. Differences were indeed small. Averaged on a spill-by-spill basis the difference between magnetic fields for Positive99 and Negative99 runs was equal to -3.3 G (-0.9 G) for the upstream (downstream) magnet.

2.1.6 Multiwire proportional chambers. Charged particles were tracked by MWPCs. Four of them were located upstream of the Analyzing Magnet and five downstream. Each chamber had four anode-wire planes with cathode planes between them. Operating voltages were in the range of 2 to 3 kV. Wire pitch varied from 1.016 mm for the two most upstream chambers to 2.000 mm for the three most downstream chambers. Such a narrow pitch enabled precise space-point reconstruction and reduced individual wire rates.

2.1.7 Hodoscopes. The same-sign (SS) and opposite-sign (OS) hodoscopes were the key elements in all HyperCP physics triggers. The SS and OS hodoscopes had 24 scintillators each. Each SS (OS) scintillator was 68 cm long, 9 cm wide, and 2 cm (1 cm) thick. For each hodoscope, scintillators were arranged into two planes with 12 counters each. In each SS (OS) plane adjacent counters were separated by 7 cm (0 cm) and, consequently, the overlap between counters from different planes was 1 cm (4.5 cm) at each counter edge.

2.1.8 Hadronic calorimeter. The hadronic calorimeter served as another trigger element. Most hits in SS and OS hodoscopes were due to the interaction of secondary beam particles with the spectrometer material. The calorimeter required some minimum energy deposit and, thus, reduced the number of triggers from background

events.

The calorimeter comprised 64 layers of 24.1 mm thick Fe sandwiched with 5 mm thick scintillator. Each scintillator layer had 32 waveshifting fibers that brought the light to the light guide and photomultiplier. Since the calorimeter was used only for the trigger and not for particle trajectory reconstruction, good shower-position resolution was not necessary.

The energy threshold for the proton or antiproton from $\Xi^{\mp} \rightarrow \Lambda(\overline{\Lambda})\pi^{\mp} \rightarrow p(\overline{p})\pi^{\mp}\pi^{\mp}$ decays was set at 60 GeV. The requirement to have the energy above the threshold for at least one opposite-sign particle formed the CAL(CAS) trigger. The energy threshold for the opposite-sign pion from $K^{\mp} \rightarrow \pi^{\mp}\pi^{\pm}\pi^{\mp}$ decays was 45 GeV and formed the CAL(K) trigger. It might seem meaningless to have the CAL(CAS) trigger since it was satisfied by every event that satisfied the CAL(K) threshold. However, the prescale factor was set to one for CAL(CAS) and to two for the CAL(K) trigger. This explains why both thresholds were used.

2.1.9 Muon system. The purpose of the Muon Stations was to identify and reconstruct muon tracks. Each station contained three 0.75 m thick iron blocks sandwiched with proportional tube planes in the x and y directions. Muon hodoscopes served as the main trigger element for muonic modes. The vertical muon hodoscope was situated between the second and third iron blocks whereas the horizontal hodoscope was mounted behind the third block. Such a spatial separation reduced muon trigger sensitivity to hadron punch-through and secondary beam halo.

2.1.10 Beam Hodoscope. The Beam Hodoscope was used to monitor the position and intensity of the secondary beam. It consisted of scintillation counters arranged in vertical and horizontal planes.

2.1.11 Triggers. To minimize biases simple triggers were designed. All decays

of interest had at least one particle track on the same-sign side of the spectrometer and one on the opposite-sign side. Thus, the basic trigger required the left-right coincidence of charged particles in the SS and OS hodoscopes and was called the LR trigger.

To reject background events from interactions of the secondary beam with the spectrometer material, the CAL(CAS) and CAL(K) triggers were formed as described in subsection 2.1.8. The cascade trigger (CAS) was formed by requiring both LR and CAL(CAS) triggers. It was used to obtain the data for this analysis.

2.1.12 Data acquisition system (DAQ). To perform the most precise CP violation measurement and not "throw the baby out with the bath water," one needed to collect as many candidate events as possible. Subsequent offline event reconstruction would reject bad candidate events. The HyperCP DAQ was designed to record up to 10^5 events per spill-second and to have data-to-tape rate of at least 23 MB/s. The events were small, typically 500 bytes.

2.1.13 Track reconstruction. Since the HyperCP experiment did not have any particle identification systems (e.g., time projection chamber, ring imaging Cherenkov detector, etc.), the only available information for further physics analyses was spatial position and momentum of every charged track. First, spacepoints were determined from hits in MWPCs, then track segments upstream and downstream of the Analyzing Magnets were reconstructed. Finally, track segments were matched, the complete track was formed and track momentum was calculated.

Each MWPC had four wire planes with different wire directions (two of the four planes had the same wire direction, but shifted wire positions). Spacepoints were found by minimizing

$$\chi^2 = \sum_{i=1}^{4} \frac{\left(\cos\theta_i x + \sin\theta_i y - m_i\right)^2}{\sigma_i^2}\,, \tag{2.1}$$

where θ is the "stereo angle" and defines the wire direction for plane i and m_i is the hit coordinate with error σ_i. Equation (2.1) is true only when we neglect the 6-mm gap between the wire planes in the MWPCs. It was found that due to this assumption, low momentum track reconstruction was not efficient. This problem was fixed after the initial reconstruction. Data used in this analysis were processed with the correct spacepoint-finding algorithm.

Separate reconstruction of tracks upstream and downstream of the Analyzing Magnet was performed. Every track candidate was required to have at least three spacepoints. Track parameters were found by minimizing the corresponding χ^2 function. Tracks with poor χ^2/dof were rejected. Rejection/acceptance cut value was different for the upstream and downstream tracks. It was more relaxed for the upstream track candidates in order to have a high efficiency for reconstructing closely spaced upstream tracks. Thus, upstream tracks had more fake tracks (also known as "ghosts"). Most ghosts were rejected during the matching of the upstream with the downstream track segments.

A complete track was constructed by matching upstream and downstream candidates at the bend plane of the Analyzing Magnets. Complete tracks with poor χ^2/dof were rejected. A global constrained fit, with the requirement that the upstream and downstream track segments intercept the bend plane at the same point, was performed for accepted tracks.

Track momentum was calculated using the single-bend-plane approximation. Monte Carlo studies had shown that this approximation did not bias the momentum measurement and was much faster than using the full field map.

2.2 Summary of Data Collected

In 12 months of data taking during 1997–2000, HyperCP recorded one of

the largest data samples ever by a particle-physics experiment: 231 billion events (triggers), 29,401 tapes, and 119.5 TB of data. A series of steps were performed to separate the data into different "streams" that were used for further physics analysis. A first analysis pass with very loose track-finding and invariant mass requirements was done at FNAL. This reduced the data volume by a factor of eight. Output from the first step was separated into different "streams:"

- Main Stream
- Prescaled Stream
- Muon Stream
- Monitor Stream.

All streams contained raw-event information (e.g., what wires were hit in the MWPCs) as well as information from track reconstruction (e.g., x slope for the track's upstream segment). Only the Main Stream and the Muon Stream were created for actual physics analyses. The Main Stream occupied 334 AIT2 tapes, with 50 GB capacity each, and contained approximately 26 billion events. It was further reduced with tighter selection criteria and separated into Data Summary Tape (DST) substreams named "Ξ," "Ω," "$K \to \pi\pi\pi$" and "Rare Decays."

From the Fermilab computer-"farm" processing with loose track-finding and invariant-mass selection criteria, a total of $\sim 14 \cdot 10^6$ $\Omega \to \Lambda K \to p\pi K$ events were reconstructed for the negative-polarity mode and $\sim 5 \cdot 10^6$ for the positive (antiparticle) mode. This, the world's largest sample of Ω hyperons, is ideal for searching for rare Ω decays.

CHAPTER 3

DATA SELECTION

3.1 Analysis Approach and Decays of Interest

We select data according to our ultimate goal, which is to calculate branching ratios for $\Omega^{\mp} \to \Xi^{*0}_{1530}(\overline{\Xi^{*0}_{1530}})\pi^{\mp}$ and $\Omega^{\mp} \to \Xi^{\mp}\pi^{\pm}\pi^{\mp}$. For any particle decay mode, the number of events observed in a spectrometer is determined as

$$N_{obs} = N_{exit} \cdot A \cdot \prod_{i=1}^{n} B_i \,, \tag{3.1}$$

where N_{exit} is the number of Ω-particles exiting the hyperon magnet, A is the spectrometer acceptance which is calculated from Monte Carlo simulations, and B_i are all subsequent branching ratios. To cancel the unknown N_{exit} we write equation (3.1) for signal and "normalizing" modes and divide one by the other. Thus, the equations for branching ratios:

$$B(\Omega^- \to \Xi^{*0}_{1530}\pi^-) = \frac{N_{\Omega^- \to \Xi^{*0}_{1530}\pi^-}}{N_{\Omega^- \to \Lambda K^-}} \cdot \frac{A_{\Omega^- \to \Lambda K^-}}{A_{\Omega^- \to \Xi^{*0}_{1530}\pi^-}} \cdot \frac{B_{\Omega^- \to \Lambda K^-} \cdot B_{K^- \to \pi^+\pi^-\pi^-}}{B_{\Xi^{*0}_{1530} \to \Xi^-\pi^+} \cdot B_{\Xi^- \to \Lambda\pi^-}} \,, \tag{3.2}$$

$$B(\Omega^- \to \Xi^-\pi^+\pi^-) = \frac{N_{\Omega^- \to \Xi^-\pi^+\pi^-}}{N_{\Omega^- \to \Lambda K^-}} \cdot \frac{A_{\Omega^- \to \Lambda K^-}}{A_{\Omega^- \to \Xi^-\pi^+\pi^-}} \cdot \frac{B_{\Omega^- \to \Lambda K^-} \cdot B_{K^- \to \pi^+\pi^-\pi^-}}{B_{\Xi^- \to \Lambda\pi^-}} \,, \tag{3.3}$$

and similarly for antiparticle modes.

The sequences of five-track decays that we need to reconstruct and study are as follows:

- Signal-mode resonance decay:

$$\Omega^{\mp} \to \Xi^{*0}_{1530}(\overline{\Xi^{*0}_{1530}})\pi^{\mp}$$

$$\Xi^{*0}_{1530}(\overline{\Xi^{*0}_{1530}}) \to \Xi^{\mp}\pi^{\pm} \,. \tag{3.4}$$

$$\Xi^{\mp} \to \Lambda(\overline{\Lambda})\pi^{\mp} \,, \tag{3.5}$$

$$\Lambda(\overline{\Lambda}) \to p(\overline{p})\pi^{\mp} \,; \tag{3.6}$$

Table 3.1. Particle properties (from [32]).

Particle	Mass (MeV/c^2)	Lifetime (cm/c)	Spin
$\Omega^{\pm}$	1672.45 ± 0.29	2.461 ± 0.033	1.5
$\Xi^{\pm}$	1321.31 ± 0.13	4.914 ± 0.045	0.5
$\Lambda(\overline{\Lambda})$	1115.683 ± 0.006	7.888 ± 0.060	0.5
$K^{\pm}$	493.677 ± 0.016	371.293 ± 0.720	0
$\pi^{\pm}$	139.570 ± 0.00	780.450 ± 0.150	0
$p(\overline{p})$	938.272 ± 0.00	stable	0.5

- Signal-mode 3-body decay:

$$\Omega^{\mp} \to \Xi^{\mp}\pi^{\pm}\pi^{\mp}\,.$$

$$\Xi^{\mp} \to \Lambda(\overline{\Lambda})\pi^{\mp}\,, \quad \Lambda(\overline{\Lambda}) \to p(\overline{p})\pi^{\mp}\,;$$

- Normalizing-mode decay:

$$\begin{aligned} &\Omega^{\mp} \to \Lambda(\overline{\Lambda})K^{\mp}\,, \\ &K^{\mp} \to \pi^{\mp}\pi^{\mp}\pi^{\pm}\,, \\ &\Lambda(\overline{\Lambda}) \to p(\overline{p})\pi^{\mp}\,. \end{aligned} \tag{3.7}$$

For all three particle (antiparticle) modes the final state is $p\pi^+\pi^-\pi^-\pi^-$ ($\overline{p}\pi^-\pi^+\pi^+\pi^+$). Particle properties are listed in Table 3.1. Decay topologies are indicated in Figures 3.1 and 3.2.

3.2 Selection of Event Candidates

The Rare Decay data subset was used for the analysis. All events in the Main Stream that were suitable for forbidden decay searches (i.e., $\Omega \to \Lambda\pi$, $\Xi^0 \to p\pi^-$, $\Omega \to pK\pi$, $\Omega \to p\pi\pi$) or contained five or more fully reconstructed charged tracks were saved to the Rare Decay substream. This procedure greatly reduced the size of the data set with the candidate events going from 334 AIT2 tapes to only four.

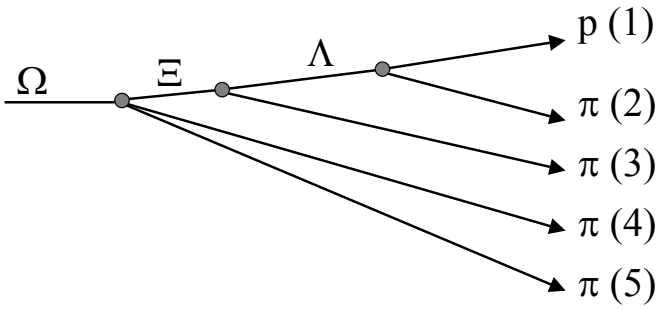

Figure 3.1. Signal-mode decay topology.

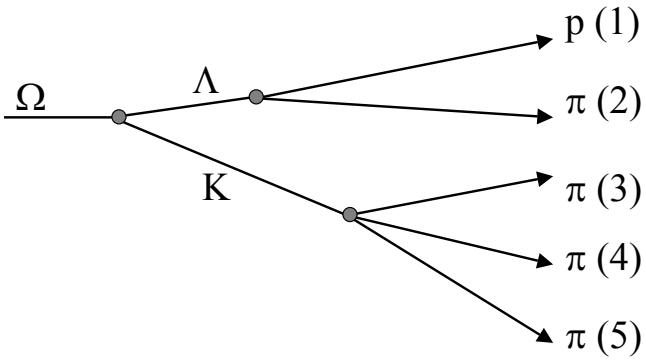

Figure 3.2. Normalizing-mode decay topology.

Conditions of the experiment as well as the experimental setup were different for the 1997 and 1999 run periods. For example, in 1997 the target was mispositioned due to alignment errors, and its position was corrected for the 1999 run. This implies that the 1997 and 1999 runs should be analyzed separately. Systematic errors are also different. Since the 1999 run has roughly twice as much data as the 1997, we have analyzed data only from the 1999 run period.

The quality of the runs was checked by the members of the HyperCP collaboration. Some runs were identified as bad for various reasons, e.g., low efficiency in hodoscopes, MWPCs or the calorimeter, movement of the target during the run, etc. We excluded bad runs from the analysis.

We also excluded "polarized" runs, i.e., runs where $\Omega^{\mp}$ were created with nonzero polarization. Since the asymmetry parameters for both signal modes are unknown, polarized runs may introduce errors in the branching ratio calculations. Moreover, polarized runs are only 10% of the data set. Runs that we have used in the analysis are listed in Appendix A.

The next step was to create a data set with events that could be potentially reconstructed as one of the signal (1.2, 1.3) or normalizing (1.1) modes (this procedure is also known as "skimming"). Candidate events were selected from the Rare Stream, which also contains data for other searches, and saved on the local IIT hard drive. To be saved, events were required to satisfy the following criteria:

1. have at least two opposite sign (OS) and at least three same sign (SS) fully reconstructed tracks;

2. have the best $\Omega^{\mp}$ reconstructed invariant mass within 50 MeV/c^2 from its PDG value.

We found that $388,909$ $(195,928)$ particle (antiparticle)-mode events passed the requirements above. This includes $133,175$ $(60,968)$ events with more than five fully reconstructed tracks. The size of the data set for the actual analysis was thus reduced from 151 GB to 811 MB.

The $\Omega^{\mp}$ invariant mass was reconstructed for every possible track combination as

$$M_{\Omega}^2 = (p_p^i + p_\pi^j + p_\pi^k + p_\pi^l + p_\pi^m)^2 \,, \tag{3.8}$$

where p_p^i is the energy-momentum four-vector and the i-th track is a proton. The index i varies from one to the number of OS tracks (in short, $i = 1, \ldots n_{OS}$). Given such a notation we supplement equation (3.8) with

$$i = 1, \ldots n_{OS} \,, \quad j = 1, \ldots n_{OS} \,, \quad i \neq j \,,$$

$$k = 1, \ldots n_{SS} - 2 \,, \quad l = k + 1, \ldots n_{SS} - 1 \,, \quad m = l + 1, \ldots n_{SS} \,.$$

We picked the combination that gave Ω mass closest to its PDG value. If the reconstructed $\Omega^{\mp}$ mass was within 50 MeV from the PDG value, then this event passed the second requirement and was saved.

The difference between the reconstructed Ω^- (Ω^+) invariant mass and the corresponding PDG value is shown in Figure 3.3 (3.4). Both distributions indicate an enhancement of events near the $\Omega^{\mp}$ mass. We fit the distributions with the Gaussian plus polynomial of order one function, which returns $4,768 \pm 276$ $(1,814 \pm 167)$ particle (antiparticle)-mode events under the peak.

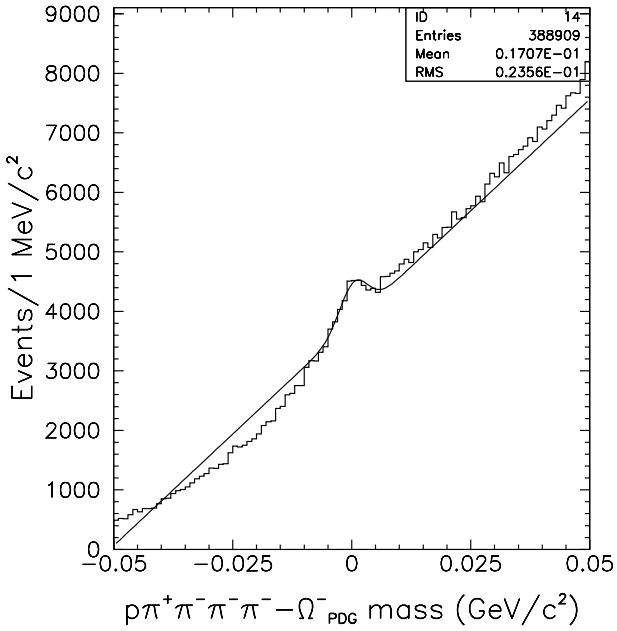

Figure 3.3. Difference between reconstructed Ω^- invariant mass and PDG value. Solid line is Gaussian plus polynomial of order one fit, which returns $N = 4,768 \pm 276$ events under the peak.

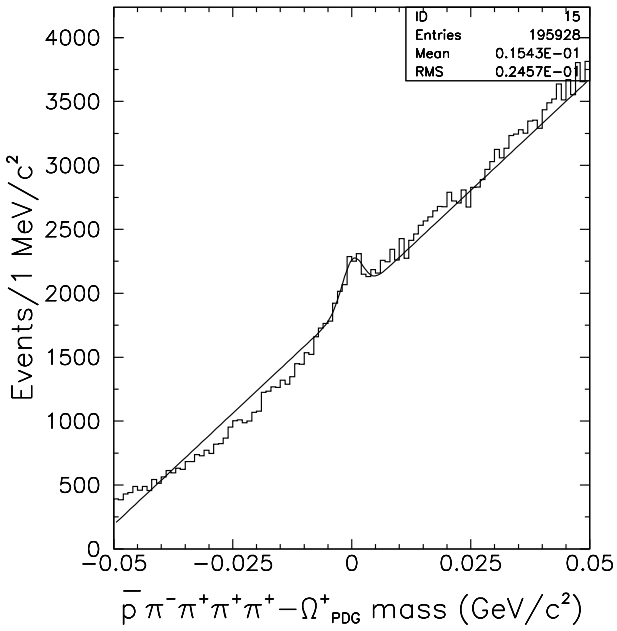

Figure 3.4. Difference between reconstructed Ω^+ invariant mass and PDG value. Solid line is Gaussian plus polynomial of order one fit, which returns $N = 1,814 \pm 167$ events under the peak.

CHAPTER 4

ANALYSIS

4.1 Monte Carlo Simulation

Monte Carlo (MC) simulation is one of the most popular techniques for parameter estimation in elementary particle physics. For example, it provides information about what fraction of particles emitted from the target decayed and were accepted by the spectrometer. This value is necessary for the correct calculation of branching ratios. The Monte Carlo method is widely used to test event reconstruction and analysis procedures in general.

We used the so-called External Monte Carlo (EMC) technique in this analysis. In a nutshell, we

1. generate parent particle at the target by specifying its momentum (p_x, p_y, p_z) and position (x, y, z);
2. trace the particle through the spectrometer collimator;
3. simulate the particle decay in the mode of interest;
4. trace decay products through the spectrometer;
5. digitize decay product hits in the detector;
6. save the event if it satisfies trigger requirements.

To minimize the difference between EMC events and data, EMC output has the same form as the data. To simulate decays of interest we make modifications to steps one and three. All other steps are performed with the HyperCP MC package to which many people have contributed. More information about the HyperCP MC may be found elsewhere [4].

The following sections describe in detail how we generate the parent particle at the target and simulate decays via the signal and normalizing modes. To launch the MC one has to provide values for various run-dependent variables, e.g., position of the peak of the beam distribution at the target, standard deviation (σ) of the beam distribution at the target, position of the center of the target, target size, etc. To fill them out we have chosen run #4062 (#4063) as a typical Negative'99 (Positive'99) run with average $\sigma_x = 2.90$ mm, $\sigma_y = 2.80$ mm ($\sigma_x = 2.34$ mm, $\sigma_y = 2.45$ mm) for the beam distribution. The standard deviations of the beam distribution in x and y, averaged over spills, for unpolarized good '99 runs is shown in Figure 4.1. To make the MC simulation as realistic as possible, multiple scattering, accidental hits, and detector inefficiencies were incorporated.

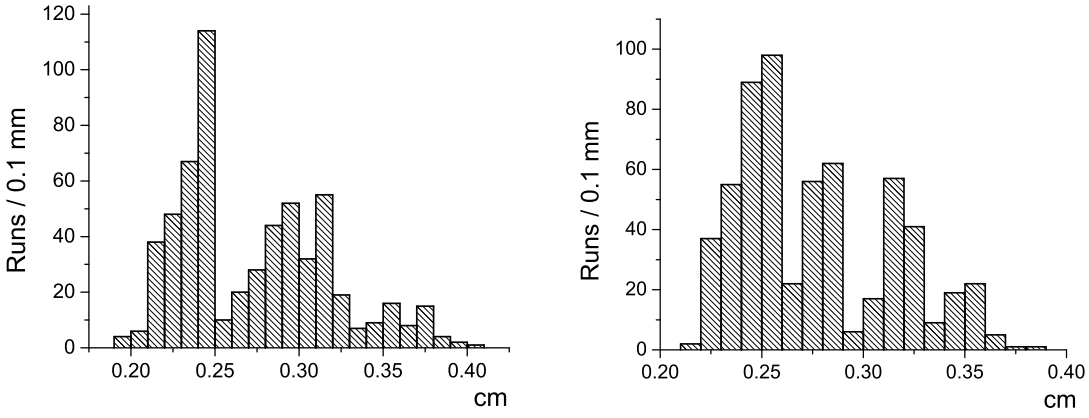

Figure 4.1. Average standard deviation of beam distribution in x (left plot) and y (right plot). Only unpolarized good '99 runs have been used.

4.1.1 Particle Polarization and Decay Parameters. First, let us give a brief overview of particle polarization and decay parameters since we will often refer to these concepts.

The state of spin-J particles at rest is specified by $(2J+1)^2$ real numbers t_L^M which are multipole parameters with $0 \leq L \leq 2J$ and $-L \leq M \leq L$. They

are determined by the process that formed the spin-J particles and are expectation values of tensors built from the components of spin operators $\vec{S}$ [5, 28]. For example, polarization of spin-1/2 particles is described by a vector, whereas polarization of spin-3/2 particles must be described by a vector (tensor of order one), quadrupole, and octupole tensors.

For any decay that can be described as a spin-J to spin-J' transition the orbital angular momentum of the final state L can be any value that satisfies $|J - J'| \leq L \leq (J + J')$. The decay can be characterized by $2(2J'+1)-1$ real constants of our choice (if $J < J'$, then by $2(2J + 1) - 1$ real constants). For example, the orbital angular momentum of the final state for a spin-1/2 to spin-1/2 transition (such decays as $\Xi^{\mp} \to \Lambda(\overline{\Lambda})\pi^{\mp}$ and $\Lambda(\overline{\Lambda}) \to p(\overline{p})\pi^{\mp}$) can be parity-violating S state ($L = 0$) with amplitude $S = se^{i\delta_s}$ or parity-conserving P state ($L = 1$) with amplitude $P = pe^{i\delta_p}$. The decay can be characterized by three real constants. Parameters s, p, and $\delta_p - \delta_s$ can be chosen or Lee–Yang variables [18],

$$\alpha = \frac{2\mathrm{Re}(S^*P)}{|S|^2 + |P|^2}\,, \quad \beta = \frac{-\mathrm{Im}(S^*P)}{|S|^2 + |P|^2}\,, \quad \gamma = \frac{|S|^2 - |P|^2}{|S|^2 + |P|^2}\,, \tag{4.1}$$

can be introduced.

4.1.2 Position of Parent Particle at Target. The position of the parent particle at the target was generated using Gaussian distributions for the x and y projections. Mean positions of the distributions were determined by matching data with the Monte Carlo for the normalizing mode. The z coordinate of the particle production point at the target was generated with an exponential probability density function (pdf):

$$p(z) \sim e^{-z/z_{int}}\,, \tag{4.2}$$

where z_{int} is the interaction length. For copper z_{int} is equal to 15.06 cm.

4.1.3 Momentum of Parent Particle at Target. The $\Omega^{\mp}$ was generated unpolarized, in the momentum range 110 to 240 GeV/c. We did not employ a model

to generate the momentum of the parent particle at the target in the laboratory frame. Rather, we tried various distributions until we achieved a reasonable match between MC and normalizing-mode data. This is described in greater detail in Section 4.4.

The momenta in the x and y projections were generated with uniform probability density functions, ranging from -0.35 to 0.35 GeV/c in x and from -1 to 1 GeV/c in y. We employed a more complicated pdf to generate the momentum z component. It is plotted in Figure 4.2.

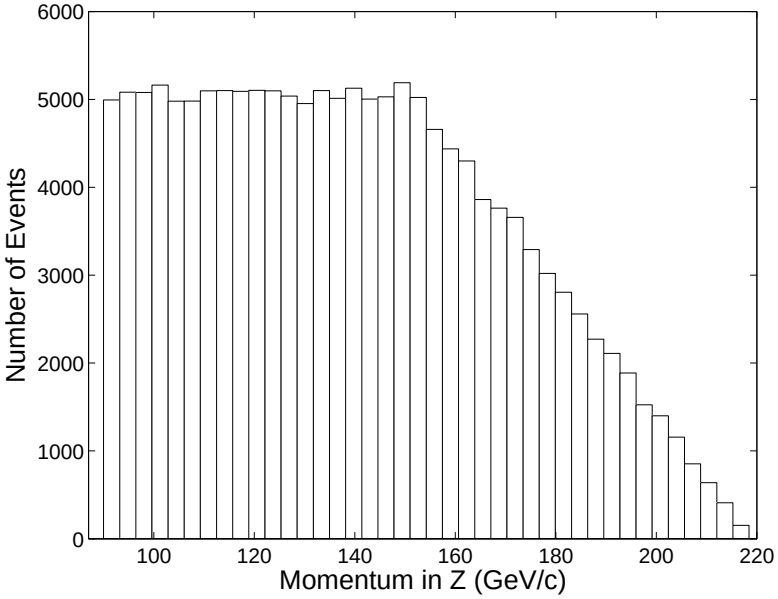

Figure 4.2. Monte Carlo generated z projection of the Ω momentum at the target.

4.1.4 Resonance Mode Decay Chain. The resonance mode decay chain is

$$\Omega^{\mp} \rightarrow \Xi^{*0}_{1530}(\overline{\Xi^{*0}_{1530}})\pi^{\mp} \rightarrow \Xi^{\mp}\pi^{\pm}\pi^{\mp} \rightarrow \Lambda(\overline{\Lambda})\pi^{\mp}\pi^{\pm}\pi^{\mp} \rightarrow p(\overline{p})\pi^{\mp}\pi^{\mp}\pi^{\pm}\pi^{\mp}\,. \qquad (4.3)$$

4.1.4.1 $\Omega^{\mp} \rightarrow \Xi^{*0}_{1530}(\overline{\Xi^{*0}_{1530}})\pi^{\mp}$ decay. This is a spin-3/2 to spin-3/2 transition. There are no published theoretical equations for the angular distribution and polarization of a daughter-particle for such a case. Thus, we will rely on general considerations. It is expected that all $\Omega^{\mp}$ decays are nearly parity-conserving [19, 23] and the

asymmetry parameter α is thus expected to be small. For all major $\Omega^{\mp}$ decay modes this is confirmed by various experiments [32]. Thus, it is natural to assume negligibly small asymmetry parameters for the resonance decay mode and zero polarization for the resulting $\Xi^{*0}_{1530}(\overline{\Xi^{*0}_{1530}})$.

Since the $\Omega^{\mp}$ is unpolarized, we generate the resonance-mode decay isotropically in the Ω rest frame. For a two-body decay, where particle *1* decays into particles *2* and *3*, the magnitude of the daughter-particle momentum in the parent-particle rest frame is completely determined by their masses:

$$|\mathbf{p}| = \left(\frac{(m_1^2 + m_2^2 - m_3^2)^2}{4m_1^2} - m_2^2 \right)^{1/2} . \tag{4.4}$$

The components of the daughter-particle momentum are generated as

$$p_x = |\mathbf{p}| \sin\theta \cos\varphi \,, \quad p_y = |\mathbf{p}| \sin\theta \sin\varphi \,, \quad p_z = |\mathbf{p}| \cos\theta \,, \tag{4.5}$$

where θ and φ are random angles. The momentum of the second daughter particle has the opposite direction.

The $\Xi^{*0}_{1530}(\overline{\Xi^{*0}_{1530}})$ mass was simulated with a Breit–Wigner probability density function:

$$p(E) = A \frac{\Gamma/2}{(E - E_0)^2 + (\Gamma/2)^2} \,, \tag{4.6}$$

where A is a normalizing constant, $E_0 = 1531.8$ MeV, $\Gamma = 9.1$ MeV (values from [32]). The normalizing constant was derived from the requirement $\int_{E_{min}}^{E_{max}} p(E)dE = 1$, where $E_{min} = 1460.88$ MeV, $E_{max} = 1532.88$ MeV are determined from the allowed phase space of the decay mode.

4.1.4.2 $\Xi^{*0}_{1530}(\overline{\Xi^{*0}_{1530}}) \to \Xi^{\mp}\pi^{\pm}$ decay. This is a spin-3/2 to spin-1/2 transition. For this type of transition, the daughter-particle ($\Xi^{\mp}$) polarization is described in [17] and the angular distribution is described in [27]. The decay is completely dominated by the strong force. In strong interactions only parity-conserving amplitudes are

allowed, which gives the following values for the Lee–Yang variables: $\alpha = \beta = 0$, $\gamma = 1$. Substituting these values together with zero polarization for the $\Xi^{*0}_{1530}(\overline{\Xi^{*0}_{1530}})$ into equation (28) in [17] and equation (13) in [27], we obtain $\hat{\mathbf{s}} = 0$ for the $\Xi^{\mp}$ polarization and $R = 1$ for the transition rate. The latter means that the momentum distribution of the $\Xi^{\mp}$ is isotropic in the $\Xi^{*0}_{1530}(\overline{\Xi^{*0}_{1530}})$ rest frame. Thus, we generate the decay $\Xi^{*0}_{1530}(\overline{\Xi^{*0}_{1530}}) \rightarrow \Xi^{\mp}\pi^{\pm}$ with uniform phase space (for details see second paragraph in section 4.1.4.1). The $\Xi^{\mp}$ is unpolarized.

4.1.4.3 $\Xi^{\mp} \rightarrow \Lambda(\overline{\Lambda})\pi^{\mp}$ **and** $\Lambda(\overline{\Lambda}) \rightarrow p(\overline{p})\pi^{\mp}$ **decays.** Both decays are spin-1/2 to spin-1/2 transitions. The polarization of the daughter particle is given by equation (3) in [18] whereas the angular distribution is described in [8]. These decays are dominated by the weak force. Their asymmetry parameters are given in Table 4.1. There is no observed *CP* violation in hyperons and we therefore assume here that $\alpha = \overline{\alpha}$ for all hyperon decays. However, we use measured (different) values for the Ω^- and the Ω^+ parity-violating parameters.

Because the $\Xi^{\mp}$ is unpolarized, we generate the decay $\Xi^{\mp} \rightarrow \Lambda(\overline{\Lambda})\pi^{\mp}$ isotropically. The polarization of the $\Lambda(\overline{\Lambda})$ after the decay is

$$\mathbf{P}_{\Lambda} = \alpha_{\Xi}\hat{\mathbf{p}}_{\Lambda}\,, \tag{4.7}$$

where $\hat{\mathbf{p}}_{\Lambda}$ is a unit vector in the direction of the $\Lambda(\overline{\Lambda})$ in the $\Xi^{\mp}$ rest frame. The transition rate [8] is

$$R = 1 + \alpha_{\Lambda}\mathbf{P}_{\Lambda}\hat{\mathbf{p}}_{p}\,, \tag{4.8}$$

where $\hat{\mathbf{p}}_p$ is a unit vector in the proton (antiproton) direction in the $\Lambda(\overline{\Lambda})$ rest frame. The corresponding angular distribution of the $p(\overline{p})$ in the $\Lambda(\overline{\Lambda})$ rest frame is

$$\frac{dN}{d\cos\theta} = \frac{N_0}{2}(1 + \alpha_{\Lambda}\mathbf{P}_{\Lambda}\hat{\mathbf{p}}_{p})\,, \tag{4.9}$$

where θ is the polar angle of the $p(\overline{p})$ and N_0 is the total number of events. We generate the decay $\Lambda(\overline{\Lambda}) \rightarrow p(\overline{p})\pi^{\mp}$ according to equation 4.8.

Table 4.1. Asymmetry decay parameters (from [32]).

Decay mode	Parameter
$\Omega^- \to \Lambda K^-$	$\alpha = 0.0175 \pm 0.0024$
$\Omega^+ \to \overline{\Lambda} K^+$	$\alpha = -0.0181 \pm 0.0038$
$\Xi^\mp \to \Lambda(\overline{\Lambda})\pi^\mp$	$\alpha(\overline{\alpha}) = -0.458 \pm 0.012$
$\Lambda(\overline{\Lambda}) \to p(\overline{p})\pi^\mp$	$\alpha(\overline{\alpha}) = 0.642 \pm 0.013$
$K^- \to \pi^-\pi^+\pi^-$	$g_- = -0.2170 \pm 0.0070, h = 0.010 \pm 0.006, k = -0.0084 \pm 0.0019$
$K^+ \to \pi^+\pi^+\pi^-$	$g_+ = -0.2154 \pm 0.0035, h = 0.012 \pm 0.008, k = -0.0101 \pm 0.0034$

4.1.5 Three-Body-Mode Decay Chain. The three-body-mode decay chain is

$$\Omega^\mp \to \Xi^\mp \pi^\pm \pi^\mp \to \Lambda(\overline{\Lambda})\pi^\mp\pi^\pm\pi^\mp \to p(\overline{p})\pi^\mp\pi^\mp\pi^\pm\pi^\mp \,. \tag{4.10}$$

4.1.5.1 $\Omega^\mp \to \Xi^\mp\pi^\pm\pi^\mp$ decay. We generate this decay with uniform phase space, since it is a standard practice in the absence of a theoretical model. We assume zero polarization for the $\Xi^\mp$.

To generate the 3-body decay with a uniform phase space we employ GENBOD, the CERN library N-body Monte Carlo event generator [6], and transfer the generated momenta to the HyperCP MC arrays. For the correct transformation one must take into account the "weight" of each event, which is an output parameter from GENBOD labelled as WT. To test the routine we generate the 3-body decay $\Omega^- \to \Xi^-\pi^+\pi^-$ with a uniform phase space and look at the pure decay kinematics without the HyperCP spectrometer distortions. In other words, plots presented here are directly from the decay-generator output. The Dalitz plot of reconstructed $\Xi^-\pi^+$ mass vs. $\pi^+\pi^-$ mass is shown in Figure 4.3. For uniform decay it must be uniformly populated with events (for details see e.g. [32], page 322) and one can see that it is. The reconstructed $\Xi^-\pi^+$ invariant mass distribution is given in Figure 4.4.

4.1.6 Normalizing-Mode Decay Chain. The normalizing-mode decay chain is

$$\Omega^\mp \to \Lambda(\overline{\Lambda})K^\mp \to p(\overline{p})\pi^\mp\pi^\mp\pi^\pm\pi^\mp \,. \tag{4.11}$$

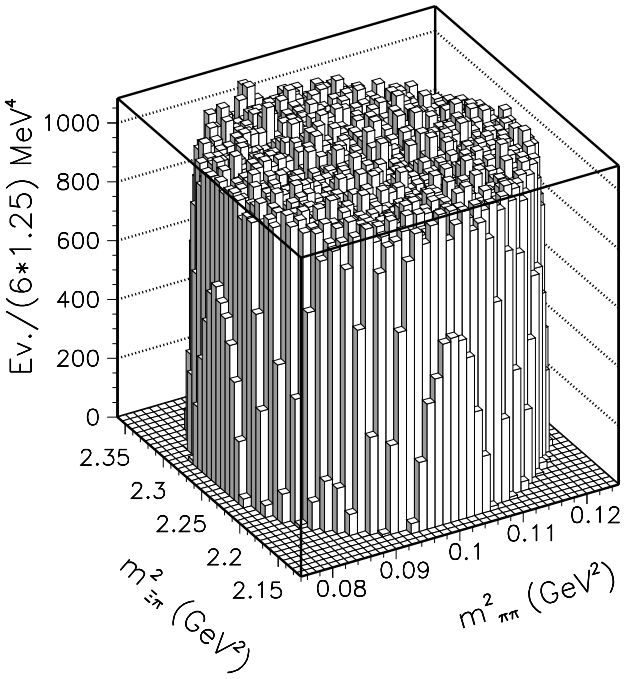

Figure 4.3. Dalitz plot of reconstructed $\Xi^-\pi^+$ mass vs. $\pi^+\pi^-$ mass for the decay $\Omega^- \to \Xi^-\pi^+\pi^-$, generated with uniform phase space using GENBOD [6].

4.1.6.1 $\Omega^\mp \to \Lambda(\overline{\Lambda})K^\mp$ **and** $\Lambda(\overline{\Lambda}) \to p(\overline{p})\pi^\mp$ **decays.** The first decay in this sequence is a spin-3/2 to spin-1/2 transition, whereas the second decay is a spin-1/2 to spin-1/2 transition. Their asymmetry parameters are given in Table 4.1. For the unpolarized $\Omega^\mp$, equation (13) from [27] simplifies to $R = 1$ and we generate the $\Lambda(\overline{\Lambda})$ isotropically in the Ω rest frame. Again, since we have unpolarized $\Omega^\mp$, equation (28) from [17] simplifies and the polarization of the $\Lambda(\overline{\Lambda})$ after the decay is given by

$$\mathbf{P}_\Lambda = \alpha_\Omega \hat{\mathbf{p}}_\Lambda \,, \tag{4.12}$$

where $\hat{\mathbf{p}}_\Lambda$ is a unit vector in the direction of the $\Lambda(\overline{\Lambda})$ in the $\Omega^\mp$ rest frame[2]. The angular distribution of the proton in the $\Lambda(\overline{\Lambda})$ rest frame is given by equation (4.8).

[2]Please note that for the joint decay chain of the spin-3/2 hyperon after integration over the full solid angle, one obtains $\mathbf{P}_\Lambda = -0.6\mathbf{P}_\Omega$, if $\gamma_\Omega = -1$. This was shown in [20] and [21]. We emphasize that the case of the joint decay chain has nothing to do with our task of generating the decay sequence (4.11).

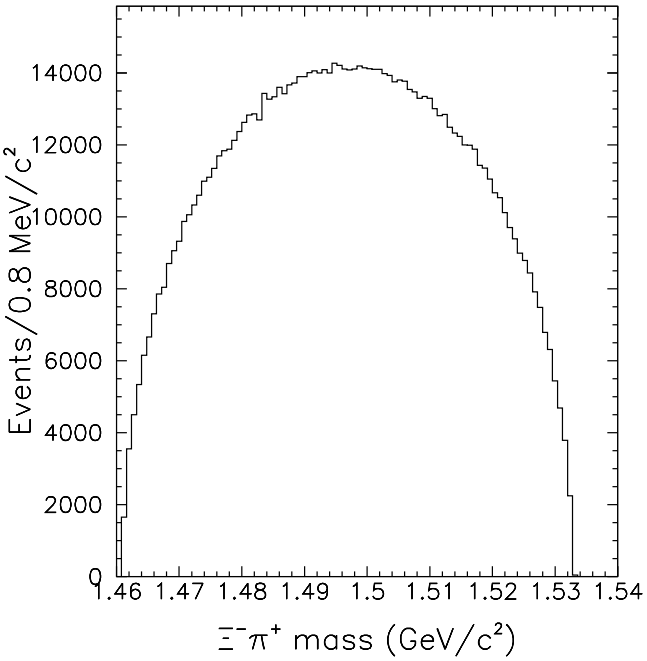

Figure 4.4. Reconstructed $\Xi^-\pi^+$ invariant mass for the decay $\Omega^- \to \Xi^-\pi^+\pi^-$, generated with uniform phase space using GENBOD [6].

Thus, the transition rate is

$$R = 1 + \alpha_\Omega \alpha_\Lambda \cos\theta \,, \tag{4.13}$$

and the angular distribution of the proton is given by a well-known equation (see e.g. [19]):

$$\frac{dN}{d\cos\theta} = \frac{N_0}{2}(1 + \alpha_\Omega \alpha_\Lambda \cos\theta) \,, \tag{4.14}$$

where θ is the polar angle of the proton in the $\Lambda(\overline{\Lambda})$ helicity frame.

To test the decay routine we looked at the angular distribution of the proton in the Λ rest frame without the HyperCP spectrometer distortions. We then fit the $\cos\theta$ distribution with a linear function and found that the value returned from the fit is $\alpha_\Omega = (1.62 \pm 0.27) \times 10^{-2}$, which is consistent with the input value $\alpha_\Omega = 1.75 \times 10^{-2}$. The distribution of $\cos\theta$ is given in Figure 4.5.

4.1.6.2 $K^\mp \to \pi^\mp\pi^\pm\pi^\mp$ **decay.** We generate this 3-body weak decay with the

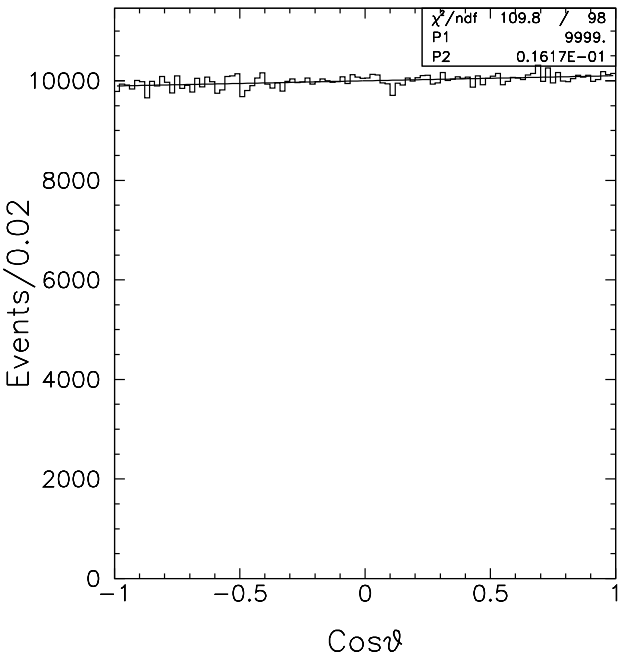

Figure 4.5. Distribution of $\cos\theta$, where θ is the polar angle of the proton in the Λ helicity frame. Solid line is a linear fit, which returns $\alpha_\Omega = (1.62 \pm 0.27) \times 10^{-2}$.

parametrization described in [32]:

$$|M|^2 = 1 + gu + hu^2 + kv^2\,, \tag{4.15}$$

$$u = \frac{(s_3 - s_0)}{m_\pi^2}\,, \qquad v = \frac{(s_2 - s_1)}{m_\pi^2}\,,$$

$$s_i = (p_K - p_i)^2\,, \qquad s_0 = \frac{1}{3}\sum_{i=1}^{3} s_i\,,$$

where p_i are four-vectors and index 3 is used for the odd-charge pion. The Dalitz-plot parameters g, h, and k are given in Table 4.1.

4.2 Event Reconstruction

The signal (1.2, 1.3) and normalizing (1.1) modes have five charged particles in their "final" state $p(\overline{p})\pi^\pm\pi^\mp\pi^\mp\pi^\mp$. The particle tracks can thus be completely reconstructed using only information from the hits in the MWPCs. Once the tracks have been reconstructed, each event is tested with a signal or normalizing-mode hypothesis using geometric or kinematic constraints.

As described in Section 3.2, we preselected events with five or more fully reconstructed tracks and reconstructed $\Omega^{\mp}$ mass within 50 MeV of its PDG value. Each event belongs to one of the following categories: signal mode, normalizing mode, or background. For the reconstruction step, our goal is to associate each of the five final-state particles for the given event with the corresponding charged track for the signal and the normalizing-mode event hypotheses.

There are many methods to reconstruct such events. The technique that is used in this analysis is based on the "best mass" hypothesis. For example, to reconstruct the decay $\Omega^- \to \Xi^-\pi^+\pi^-$, followed by $\Xi^- \to \Lambda\pi^-$ and $\Lambda \to p\pi^-$, we sequentially reconstruct invariant masses for Λ, Ξ^-, and Ω^- by choosing the track combination that gives each mass closest to the PDG value. This method was used in other HyperCP analyses as well, for example in [30].

4.2.1 Reconstruction Details. After the track reconstruction step, for each event information is saved about the total number of fully reconstructed tracks and the numbers of OS, SS, and beam tracks. For each track in the event following values are saved:

- x and y slopes for track segments upstream and downstream of the Analyzing Magnets;
- coordinates of track interception with the bend plane;
- coordinates of hits in the MWPCs.

Knowing the magnetic field in the analyzing magnet together with track slopes, we calculate the momentum for each track. The following sections explain how these values were used for event reconstruction.

4.2.1.1 Mass and momentum calculation. When a particle decays to N

daughter particles, its mass and momentum can be calculated from

$$M^2 = (\sum_{i=1}^{N} p_i)^2 \,, \quad \mathbf{p} = \sum_{i=1}^{N} \mathbf{p}_i \,, \tag{4.16}$$

where p_i are four-vectors. To form a daughter-particle four-vector we use its PDG mass if the daughter-particle is the final particle in the decay chain; otherwise we use its reconstructed invariant mass.

4.2.1.2 Decay vertex calculation. To calculate the decay vertex, one needs values of the x and y slopes and the coordinates of a point on the track for each daughter particle.

Since upstream and downstream track segments are straight lines, the i-th track segment is described by

$$\frac{x - x_{0i}}{m_i} = \frac{y - y_{0i}}{n_i} = z - z_{0i} \,, \tag{4.17}$$

where m and n are x and y slopes correspondingly (they form the directional vector $\mathbf{v} = (m_i, n_i, 1)$), and point $A_0 = (x_{0i}, y_{0i}, z_{0i})$ belongs to the track. To simplify calculations, instead of A_0, we can always use $A = (x_i; y_i; 0)$, which is another point on the track, where

$$x_i = x_{0i} - m_i z_{0i} \,, \quad y_i = y_{0i} - n_i z_{0i} \,.$$

For a decay with N daughter particles we can define the average vertex coordinate at closest approach as

$$Z = -\frac{\sum_{i=1}^{N-1} \sum_{j=i+1}^{N} [(m_i - m_j)(x_i - x_j) + (n_i - n_j)(y_i - y_j)]}{\sum_{i=1}^{N-1} \sum_{j=i+1}^{N} [(m_i - m_j)^2 + (n_i - n_j)^2]} \,, \tag{4.18}$$

$$X = \frac{1}{N} \sum_{i=1}^{N} (x_i + m_i Z) \,, \quad Y = \frac{1}{N} \sum_{i=1}^{N} (y_i + n_i Z) \,. \tag{4.19}$$

and average distance among the pairs of track combinations at closest approach as

$$D = \frac{1}{N_{cb}} \sum_{i=1}^{N-1} \sum_{j=i+1}^{N} \sqrt{[x_i - x_j + (m_i - m_j)Z]^2 + [y_i - y_j + (n_i - n_j)Z]^2} \,, \tag{4.20}$$

where N_{cb} is the binomial coefficient

$$N_{cb} = \frac{N!}{2(N-2)!}\,.$$

Unfortunately, this method does not tell us how good the found vertex parameters are.

4.2.1.3 Decay geometry fit with GFIT. Another method to find the decay vertex is to use the geometric fitting routine GFIT, which was written in the 1970s and has been exploited by many experiments. The user must provide the coordinates of every point in the MWPCs that was used to form each of the tracks. The routine returns not only vertex coordinates, but also a χ^2 probability for the fit, which allows us to judge whether or not the reconstructed event geometry is consistent with our hypothesis. It also recalculates upstream and downstream slopes and intercepts of the tracks which can be used to update the momentum calculation.

The limitation of GFIT is that it was designed to fit sequences of two two-body decays such as $\Xi^{\mp} \to \Lambda(\overline{\Lambda})\pi^{\mp}$, $\Lambda(\overline{\Lambda}) \to p(\overline{p})\pi^{\mp}$. In other words it does the geometric fit to a three-track, two-decay-vertex topology only. Besides the reconstruction of $\Xi^{\mp}$, we use GFIT for the $K^{\mp} \to \pi^{\mp}\pi^{\pm}\pi^{\mp}$ decay. Since this is a single-vertex decay, the two vertices found by GFIT are expected to be equal.

4.2.1.4 Signal-mode geometric fit. In the steps described above we find decay vertices for Λ, Ξ, and Ω and calculate the average distance of closest approach (equation (4.20)) for each of them. Now we would like to use the found decay vertex coordinates and construct some variable to distinguish events with good signal-mode topology from others with poor topology. We test event topology with the signal-mode geometry hypothesis and calculate

$$\chi^2 = \sum_{i=1}^{4}\sum_{j=1}^{4}\sum_{k=1}^{5}\left(\frac{X^{ijk} - X^{ijk}_{hit}}{\sigma^{ij}}\right)^2\,, \tag{4.21}$$

$$N_{ndof} = N_{hits} - 5\,, \tag{4.22}$$

where index i loops through four upstream wire chambers, index j loops through four wire planes in each of the wire chambers, index k loops through five reconstructed tracks, and X_{hit}^{ijk} is the coordinate of the hit in chamber i, wire plane j used by track k. Coordinate X is measured in the wire plane local coordinate system. Thus,

$$X = x\cos\theta + y\sin\theta\,, \tag{4.23}$$

where x and y are coordinates of the track's interception with the wire plane in the laboratory frame and θ is the "stereo angle" of the wire plane. The rms uncertainty in the individual hit position is defined as $\sigma = (\text{pitch of the wire plane})/\sqrt{12}$.

We calculate the number of degrees of freedom (dof) as $N_{dof} = N_{hits} - (N_{var} - N_c)$, where N_{hits} is the total number of hits that were used in the fit in upstream MWPCs and N_{var} is the number of fit variables with N_c constraints on them. In more detail, there are two variables for each track, which are x and y slopes, and three coordinates for each vertex. The total number of variables for the signal mode-geometry fit is 19. For example, the constraints for the proton track are

$$x_\Lambda = z_\Lambda\frac{p_x}{p_z} + b_x\,, \quad y_\Lambda = z_\Lambda\frac{p_y}{p_z} + b_y\,, \tag{4.24}$$

where x_Λ, y_Λ, z_Λ are the coordinates of the Λ vertex, p_x, p_y, p_z are the components of the proton momentum, and b_x and b_y are the known coordinates of the proton track interception with the bend plane. We can write similar equations for each of the five tracks plus the Λ and Ξ tracks, which gives us 14 constraints in total. Thus, we obtain $N_{var} - N_c = 5$ for the signal-mode fit.

4.2.1.5 Normalizing-mode geometric fit. For the normalizing mode we cannot construct just one χ^2 variable in analogy to the signal-mode geometry test described above. This is because there are no saved hits in the upstream MWPCs for the Λ and K tracks. Typically both particles decay before they reach the third wire chamber, and their tracks are not directly reconstructed.

Table 4.2. Numbers of degrees of freedom for upstream-hit fits.

Decay	N_{var}	N_c	N_{dof}
$\Omega^{\mp} \to \Xi^{\mp}\pi^{\pm}\pi^{\mp}$, $\Xi^{\mp} \to \Lambda(\overline{\Lambda})\pi^{\mp}$, $\Lambda(\overline{\Lambda}) \to p(\overline{p})\pi^{\mp}$	19	14	$N_{hits} - 5$
$K^{\mp} \to \pi^{\mp}\pi^{\mp}\pi^{\pm}$	9	6	$N_{hits} - 3$
$\Lambda(\overline{\Lambda}) \to p(\overline{p})\pi^{\mp}$	7	4	$N_{hits} - 3$

Instead, we calculate χ^2 and N_{dof} separately for the decays $K^{\mp} \to \pi^{\mp}\pi^{\mp}\pi^{\pm}$ and $\Lambda(\overline{\Lambda}) \to p(\overline{p})\pi^{\mp}$. These can be used in addition to decay vertex parameters. To calculate them we use the same technique as for the signal mode. Details on how we derive the numbers of degrees of freedom are given in Table 4.2.

4.2.1.6 Particle at target calculation. To calculate the particle position at the target we trace the particle backwards through the collimator. We start with the reconstructed particle momentum $\mathbf{p} = (p_x; p_y; p_z)$ and coordinates of the point $A_0 = (x_0; y_0; z_0)$ on the track, which is typically the reconstructed particle vertex. First, we trace the particle to the exit of the collimator which is straightforward due to the absence of magnetic field in the decay region. The next step is to trace the particle back through the Hyperon Magnet field, from the collimator's exit to its entrance. While our considerations are simple, they are commonly utilized in experimental particle physics. For clarity, let us consider the reverse situation, when the particle moves from the collimator entrance (point a) to the exit (point b). Inside the collimator, the magnetic force $\mathbf{F} = q[\mathbf{v} \times \mathbf{B}]$ acts on the particle and rotates its momentum vector. We write for the y-projection

$$\int_{p_{ya}}^{p_{yb}} dp_y = \int_0^{(z_b - z_a)/v_z} F_y dt \tag{4.25}$$

and can introduce a "transverse kick" of the Hyperon Magnet,

$$p_t = qB_x(z_b - z_a)\,. \tag{4.26}$$

The radius of the particle orbit is

$$R = \frac{dr}{d\alpha} = \frac{v_z dt}{d\alpha} = \frac{v_z p dt}{dp_y} = \frac{v_z p dt}{F_y dt} = \frac{\sqrt{p_y^2 + p_z^2}}{qB_x} = \sqrt{p_y^2 + p_z^2} \left| \frac{z_b - z_a}{p_t} \right| . \qquad (4.27)$$

Please note that $d\alpha \approx \sin d\alpha = dp_y/p$ since the angle α is small (see Figure 4.6). Finally, from geometrical considerations, we get the following dependences:

$$x_a = x_b + \frac{p_x}{p_z}(z_a - z_b) , \qquad (4.28)$$

$$y_a = y_R - \sqrt{R^2 - (z_a - z_R)^2} , \qquad (4.29)$$

where $y_R = y_b + Rp_z/p$ and $z_R = z_b - Rp_y/p$ are coordinates of the orbit center.

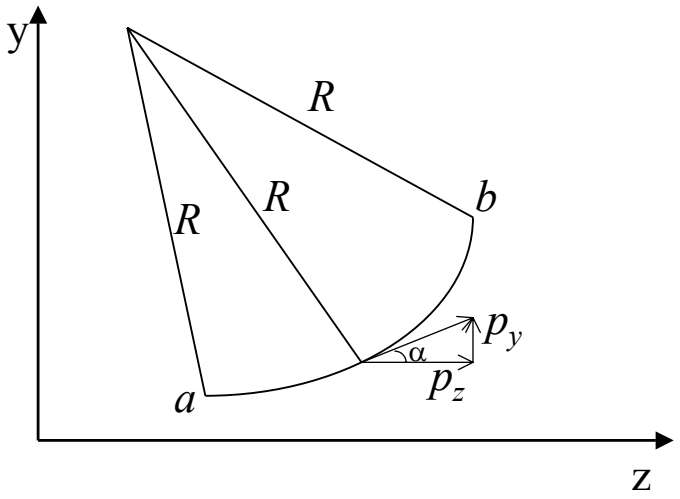

Figure 4.6. A charged particle is deflected in the constant magnetic field while moving along the z axis.

4.2.1.7 Trigger requirement for events with more than five tracks. For events with more than five tracks we choose the five tracks that give the best agreement with signal or normalizing-mode hypotheses. Then we check that the Cascade trigger was fired by the tracks of our choice. This is necessary for the proper acceptance calculations, because our MC generates only five-track decay modes and, therefore, MC-events have exactly five tracks, but data-events may have more than five tracks.

As mentioned in Section 2.1.13, the hodoscopes and calorimeter were the trigger elements for nonmuonic decay modes. The Left-Right trigger required at least one hit in the same-sign and opposite-sign hodoscopes. For each "fired" counter, we projected the downstream segment of the chosen track to the counter z position. If its intersection was within the counter's active region, then the counter was hit by this track. We required at least one counter hit by at least one track belonging to the signal or normalizing-mode decay in each of the same-sign and opposite-sign hodoscopes.

The method to define the counter active region with only the recorded data is subtle. A counter can be fired by the tracks themselves or by the products of accidental interaction of the secondary beam with spectrometer material. While we have full information about the former, there are no recorded data for the latter case. Moreover, data show that accidental interactions are responsible for roughly 10% of "fired" counters, thus, we cannot neglect them. To estimate the fraction of accidental interactions, we calculate the distance along the x axis from the center of the "fired" counter to the closest track and divide the number of events that are more than 4.5 cm from the counter center by the total number of events. For selected counters this distance is plotted in Figures 4.7 and 4.8. One can see the edges at ± 4.5 cm.Counters were relatively long and particles that traversed the Analyzing Magnets apertures were not able to pass above or below the hodoscopes. Given this we define the counter active region as rectangle inscribed in the counter. The borderline of the rectangle is 0.5 cm away from the vertical counter edges and 2 cm away from both horizontal edges towards the counter center.

In spite of the somewhat subjective active-region border selection, we are confident in the results. Our goal is to exclude events with more than five tracks that were written to tape when the trigger was fired by the background particles. To

maximize the probability of excluding such events, the area selected for the active region is, perhaps, smaller than the "true" active region. Since there are five tracks in our decay modes, the chances to satisfy our trigger requirements are high and the downside will be rejecting only a small fraction of "good" events.

The hadronic calorimeter threshold for the Cascade trigger was set at 60 GeV/c, thus we required the proton momentum to exceed this threshold. If the proton momentum was greater than or equal to the threshold, we projected its downstream segment to the calorimeter upstream face. If the intersection was within the calorimeter active region, then the event was deemed to satisfy the CAL(CAS) trigger. The entire calorimeter front face was used as the active area. The distribution of particles with $p \geq 60$ GeV/c at the position of the calorimeter front face is shown in Figure 4.9.

These active-region requirements were tested with Monte Carlo simulations and were found to be 100% efficient, which means that all signal events in the MC samples passed them. For the data, all signal- and normalizing-mode events after the corresponding selection criteria also satisfied these requirements.

4.3 Final Event Selection

As mentioned in the preceding section, event reconstruction is based on the "best mass" hypothesis. First, the track with the highest momentum is assigned as the proton. The remaining tracks' tagging is based on the track combination that gives reconstructed invariant mass closest to the PDG value. Then we calculate all other parameters needed to describe the event, e.g., vertex position, χ^2/dof for the decay geometry, particle position at the target, etc. A detailed explanation how to calculate all these quantities is given in Section 4.2.

Event selection criteria (also known as "cuts") for both signal modes and the normalizing mode are

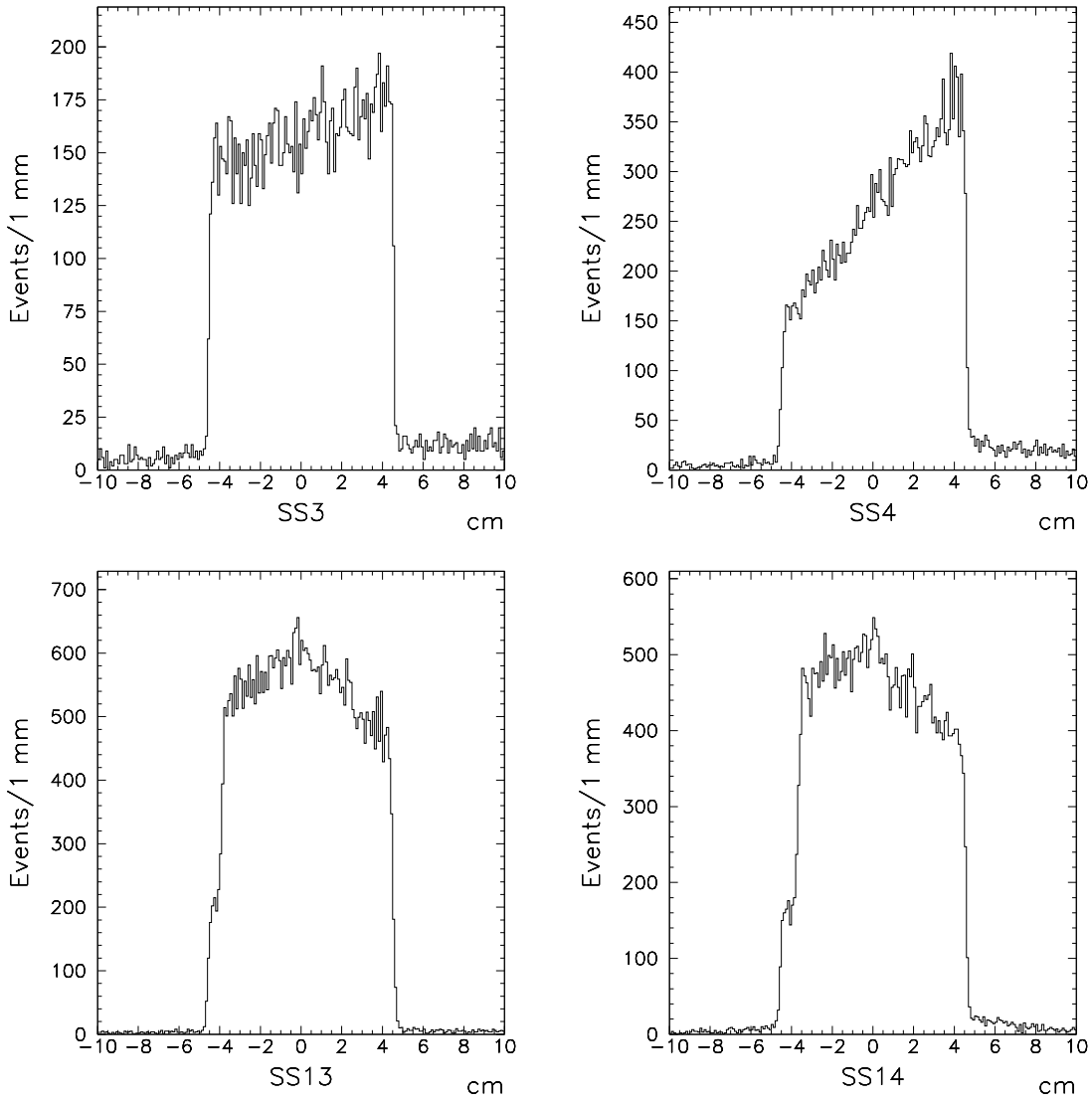

Figure 4.7. Distance along the x axis from the center of the "fired" counter to the closest track for selected SS counters.

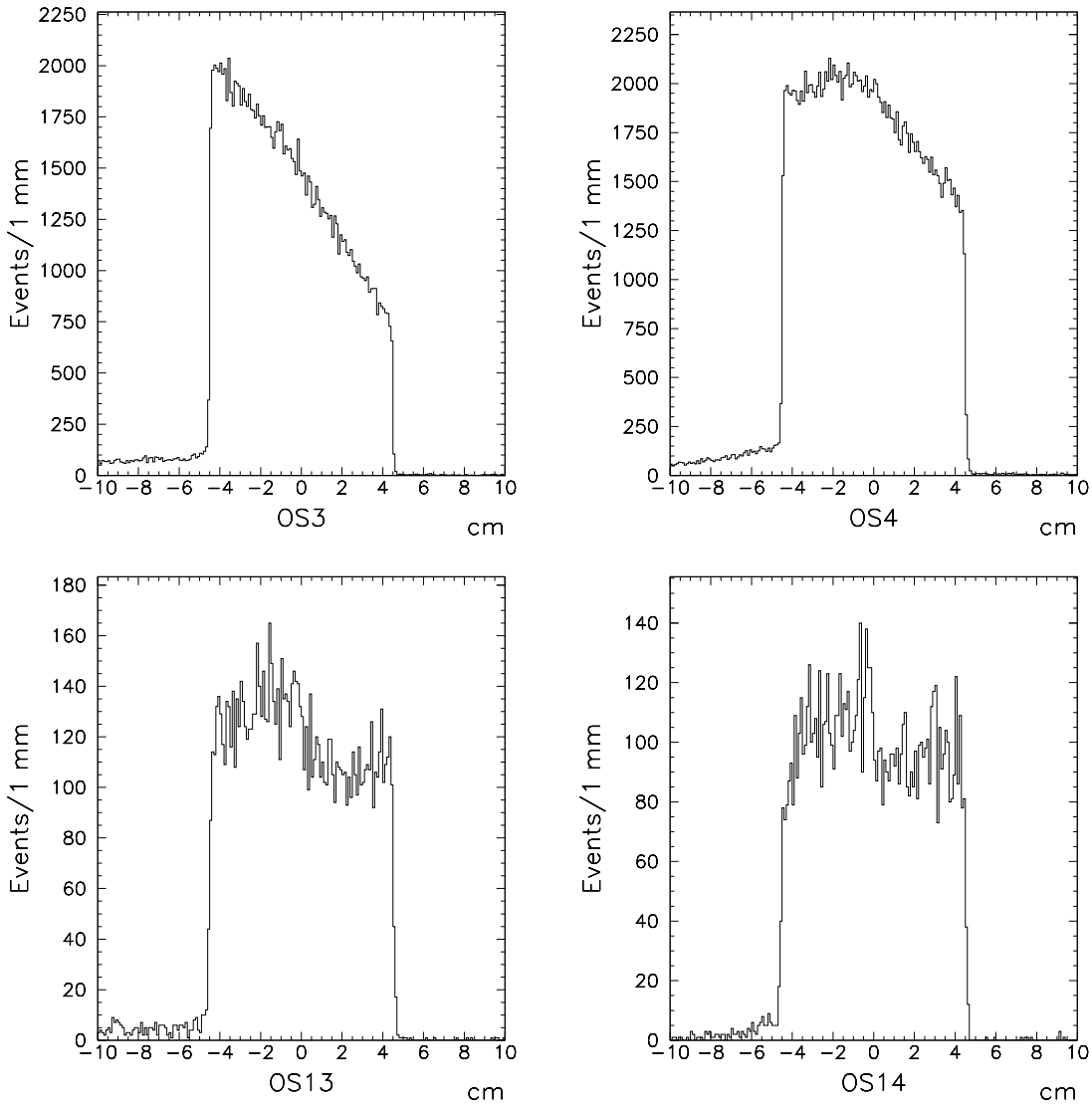

Figure 4.8. Distance along the x axis from the center of the "fired" counter to the closest track for selected OS counters.

Table 4.3. Parameters for the Gaussian-plus-polynomial fit for selected distributions (normalizing-mode Neg99 MC).

Distribution	Gaussian Mean	Standard Deviation
$m_{p\pi^-} - m_{\Lambda(PDG)}$	$(-1.67 \pm 0.35) \cdot 10^{-2}$ MeV/c^2	$0.80 \pm 0.35 \cdot 10^{-2}$ MeV/c^2
$m_{\pi^-\pi^-\pi^+} - m_{K(PDG)}$	$(-16 \pm 0.80) \cdot 10^{-2}$ MeV/c^2	$1.75 \pm 0.74 \cdot 10^{-2}$ MeV/c^2
$m_{p\pi^+\pi^-\pi^-\pi^-} - m_{\Omega(PDG)}$	$(-17.5 \pm 0.88) \cdot 10^{-2}$ MeV/c^2	$2.04 \pm 0.76 \cdot 10^{-2}$ MeV/c^2
x_{target}	$(1.52 \pm 0.40) \cdot 10^{-3}$ cm	$0.09 \pm 0.30 \cdot 10^{-3}$ cm
y_{target}	$6.48 \pm 0.45 \cdot 10^{-3}$ cm	$0.10 \pm 0.34 \cdot 10^{-3}$ cm

- reconstructed invariant masses of particles within 3σ of corresponding PDG values;
- total momentum between 135 and 220 GeV/c;
- all decay vertices inside the vacuum decay region and vertex topology consistent with the decay;
- tracks form good vertices;
- reasonable χ^2/dof from fitting decay topology to upstream track segments;
- reconstructed Ω track within the aperture of the collimator and originating from the target.

4.3.1 Normalizing Mode. We calculate standard deviations to be used in invariant mass and target position cuts by fitting the corresponding Monte Carlo distributions with Gaussian-plus-polynomial functions. Results for the normalizing-mode "Neg99" ("Pos99") MC are given in Table 4.3 (4.4) with corresponding distributions plotted in Figures 4.10 and 4.11 (Figures B.1 and B.2).

Cuts for the normalizing mode are listed in Table 4.5. Monte Carlo distributions for each selection criterion are plotted in Figures 4.12 to 4.19 for the "Neg99" subset. Monte Carlo distributions for the "Pos99" subset look similar. Not to bore

Table 4.4. Parameters for the Gaussian-plus-polynomial fit for selected distributions (normalizing-mode Pos99 MC).

Distribution	Gaussian Mean	Standard Deviation
$m_{\overline{p}\pi^+} - m_{\Lambda(PDG)}$	$(-0.62 \pm 0.35) \cdot 10^{-2}$ MeV/c^2	$0.80 \pm 0.37 \cdot 10^{-2}$ MeV/c^2
$m_{\pi^+\pi^+\pi^-} - m_{K(PDG)}$	$(-16.9 \pm 0.80) \cdot 10^{-2}$ MeV/c^2	$1.75 \pm 0.74 \cdot 10^{-2}$ MeV/c^2
$m_{\overline{p}\pi^-\pi^+\pi^+\pi^+} - m_{\Omega(PDG)}$	$(-17.3 \pm 0.89) \cdot 10^{-2}$ MeV/c^2	$2.04 \pm 0.75 \cdot 10^{-2}$ MeV/c^2
x_{target}	$(0.99 \pm 0.39) \cdot 10^{-3}$ cm	$0.09 \pm 0.30 \cdot 10^{-3}$ cm
y_{target}	$6.48 \pm 0.46 \cdot 10^{-3}$ cm	$0.10 \pm 0.35 \cdot 10^{-3}$ cm

the reader, we do not include them in this dissertation. Each cut can be characterized with isolated and final efficiencies based on MC calculations. Isolated efficiency is the number of events surviving this particular cut divided by the total number of events before any cuts. Final efficiency is the number of events after all cuts have been applied divided by the number of events surviving all cuts except this particular cut. Efficiencies for the Neg99 and Pos99 MC are given in Table 4.6. Based on these values we infer that we lose the largest fraction of good events due to poor reconstruction of the particle-vertex z coordinate.

Table 4.5. Selection cuts for the normalizing mode.

Cut Type	Selection Rule	Cut ID
$p(\overline{p})\pi^{\mp}$ invariant mass	$\lvert m_{p(\overline{p})\pi^{\mp}} - m_{\Lambda(PDG)}\rvert \leq 2.40$ MeV	N1
$\pi^{\mp}\pi^{\mp}\pi^{\pm}$ invariant mass	$\lvert m_{\pi^{\mp}\pi^{\mp}\pi^{\pm}} - m_{K(PDG)}\rvert \leq 5.25$ MeV	N2
$p(\overline{p})\pi^{\pm}\pi^{\mp}\pi^{\mp}\pi^{\mp}$ invariant mass	$\lvert m_{p(\overline{p})\pi^{\pm}\pi^{\mp}\pi^{\mp}\pi^{\mp}} - m_{\Omega(PDG)}\rvert \leq 6.12$ MeV	N3
$\Omega^{\mp}$ total momentum	$135 \leq P_{\Omega} \leq 220$ GeV	N4
Z coordinate of the particle vertex	$50 < \mathrm{Z}_{\Omega} < 1300$ cm	N5
	$\mathrm{Z}_{\Omega} < \mathrm{Z}_{\Lambda} < 1300$ cm	N6
	$\mathrm{Z}_{\Omega} < \mathrm{Z}_{K} < 1300$ cm	N7
Distance of closest approach	$\mathrm{DOCA}_{\Omega} < 0.3$ cm	N8
	$\mathrm{DOCA}_{\Lambda} < 0.3$ cm	N9
	$\mathrm{DOCA}_{K} < 0.35$ cm	N10
Decay geometry fitter	$(\chi^2/dof)_{\Lambda} < 2$	N11
	$(\chi^2/dof)_{K} < 3$	N12
$\Omega^{\mp}$ position at the target	$[(x_{target}/0.25)^2 +$	
	$((y_{target} - 6.4835)/0.285)^2] \leq 1$	N13
$\Omega^{\mp}$ at the collimator exit	-1 cm $\leq exit_x \leq 1$ cm	N14
	-0.6 cm $\leq exit_y \leq 0.55$ cm	N15

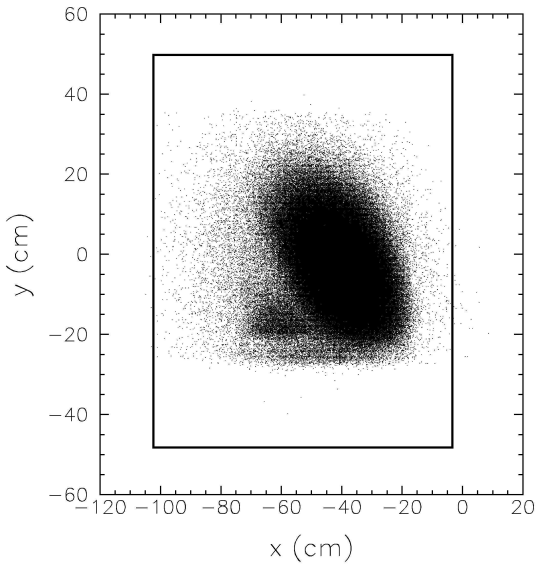

Figure 4.9. Distribution of particles with $p \geq 60$ GeV/c at the position of the calorimeter front face. The rectangle indicates the calorimeter active area.

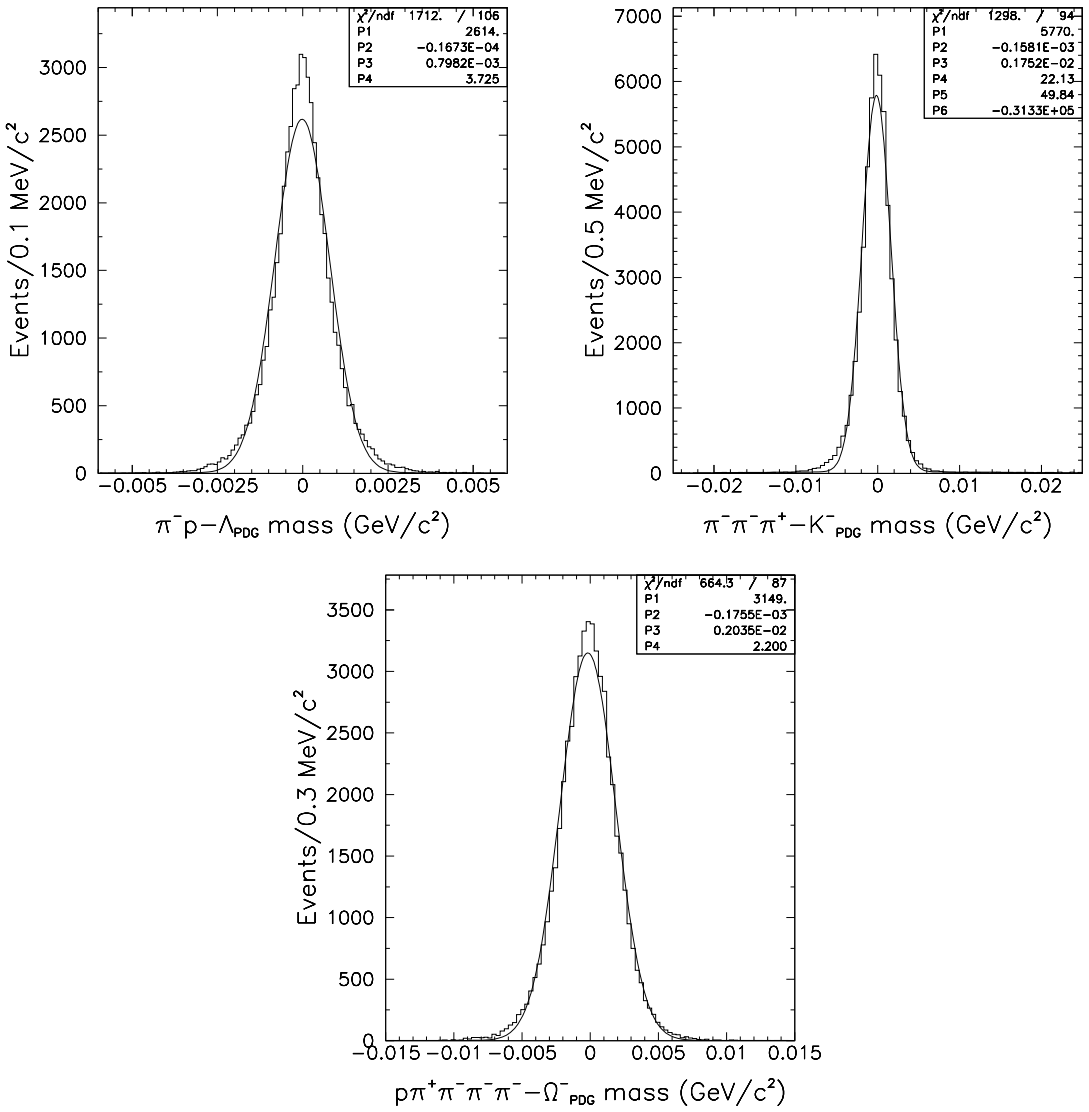

Figure 4.10. Difference between reconstructed invariant mass with no cuts and PDG values for the normalizing-mode Neg99 MC. Solid line is Gaussian-plus-polynomial fit.

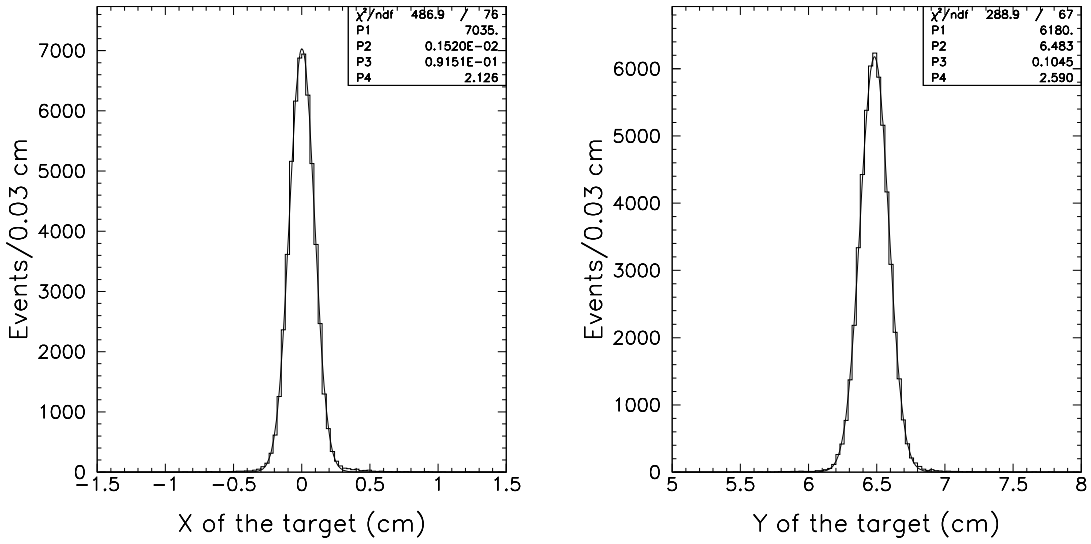

Figure 4.11. X and Y positions of the Ω^- at the target with no cuts for the normalizing-mode Neg99 MC. Solid line is Gaussian-plus-constant fit.

Table 4.6. Efficiency of selection cuts for the normalizing mode MC.

	Isolated Effic., %		Final Effic., %	
Cut ID	Neg99	Pos99	Neg99	Pos99
N1	97.9	97.8	98.4	98.4
N2	94.6	94.5	99.6	99.6
N3	98.7	98.6	99.7	99.8
N4	99.9	99.9	100	100
N5	80.2	80.4	78.5	78.9
N6	84.2	84.1	86.2	86.3
N7	74.5	74.4	79.3	79.5
N8	96.1	96.0	99.7	99.7
N9	94.8	94.7	99.2	99.0
N10	95.1	95.0	99.5	99.4
N11	92.7	92.6	97.4	97.4
N12	89.7	89.7	98.3	98.3
N13	95.8	95.8	99.0	99.1
N14	99.0	99.0	99.4	99.5
N15	99.3	99.2	99.8	99.8
All cuts	43.1	43.2		

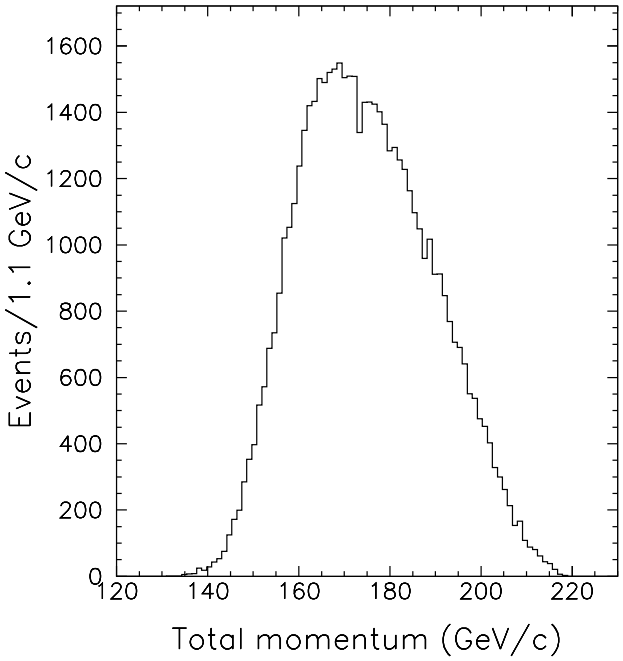

Figure 4.12. Total momentum of Ω^- with no cuts for the normalizing-mode Neg99 MC.

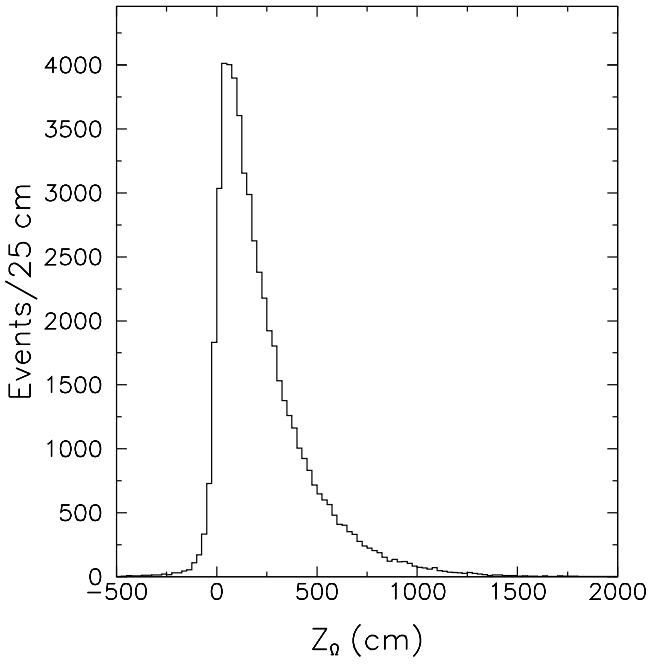

Figure 4.13. Z position of the decay vertex with no cuts for Ω^-. Normalizing mode Neg99 MC.

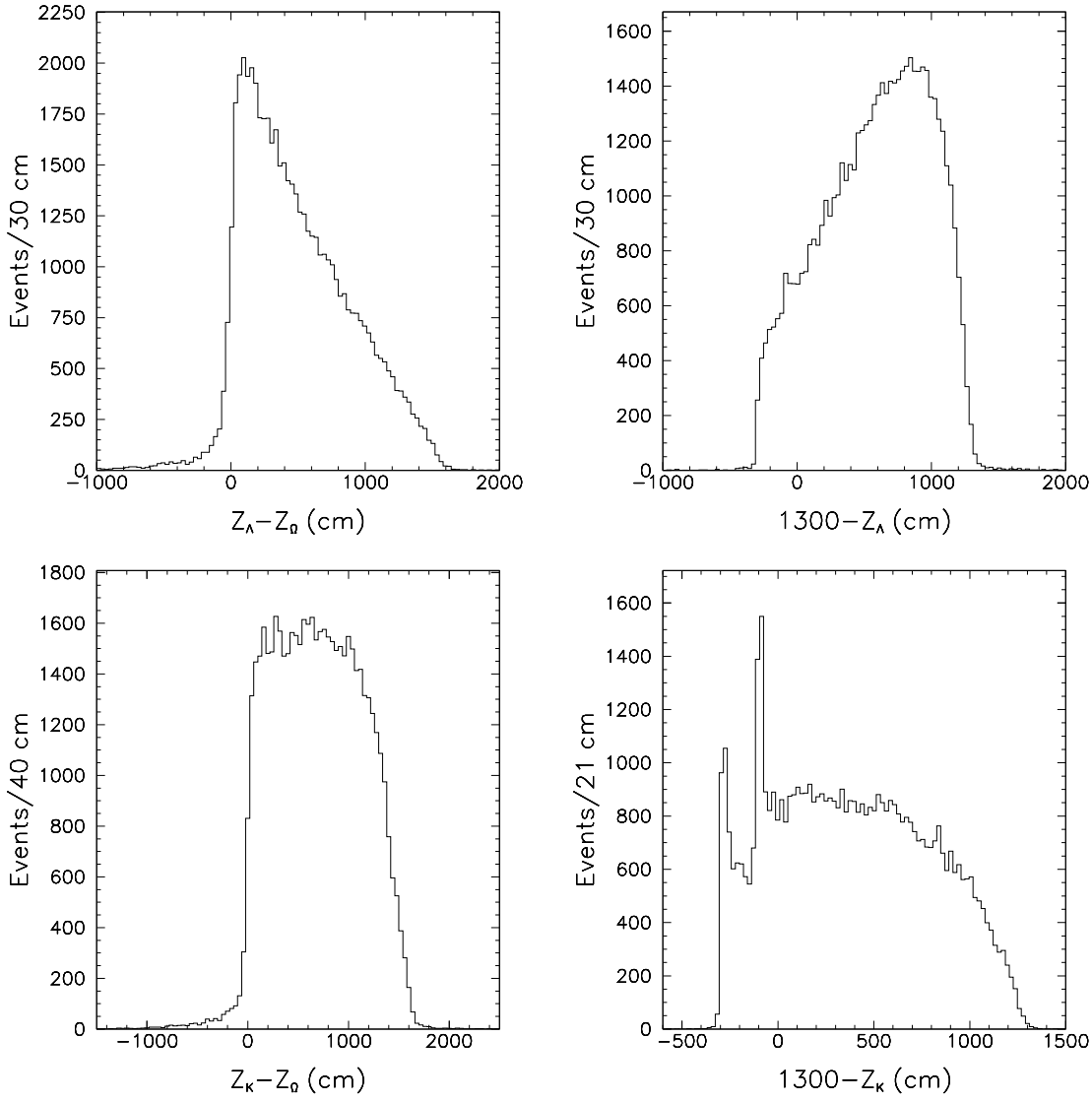

Figure 4.14. Z position of the decay vertex with no cuts. Normalizing mode Neg99 MC.

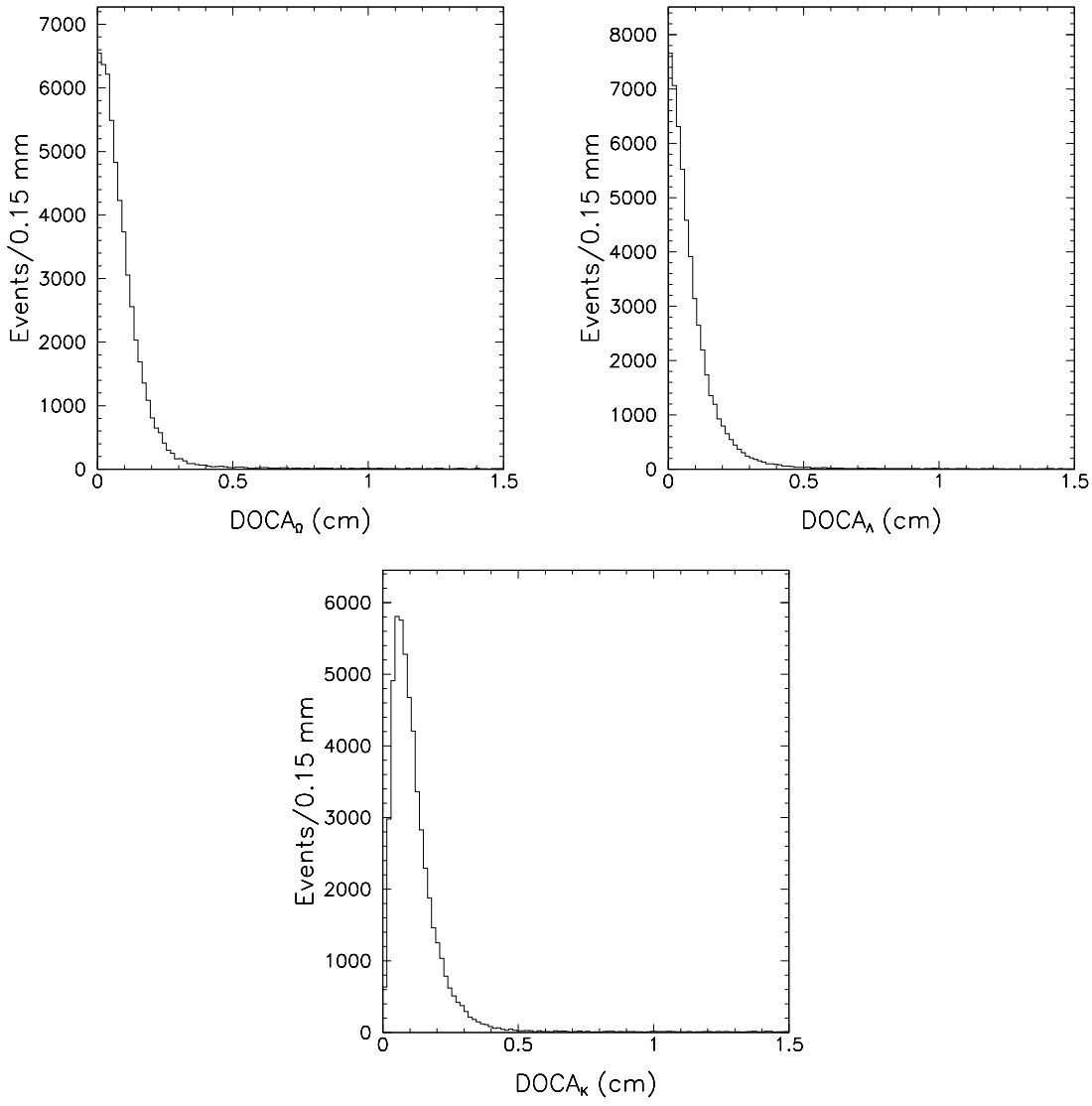

Figure 4.15. Distance of closest approach with no cuts. Normalizing mode Neg99 MC.

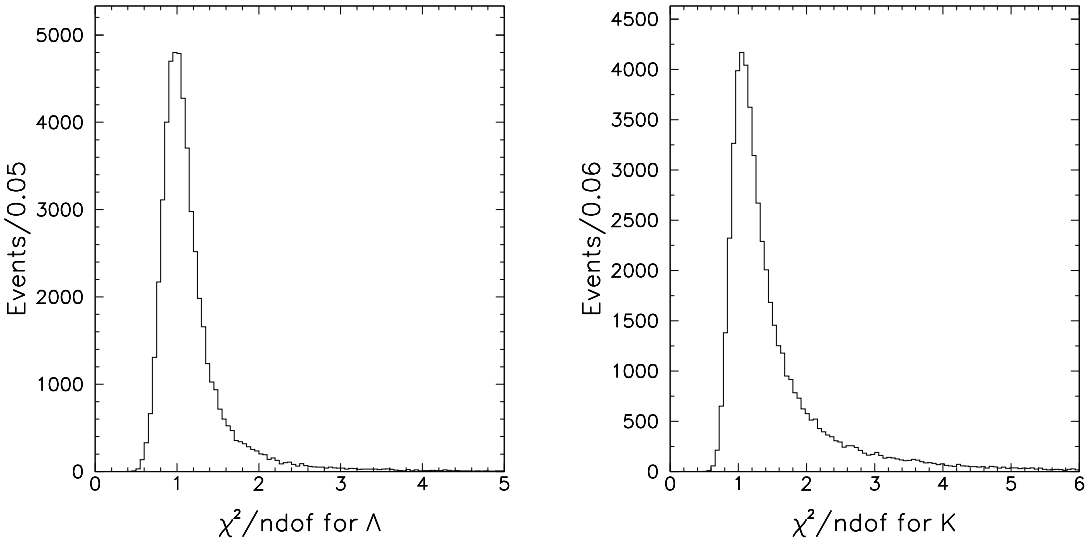

Figure 4.16. Calculated χ^2/dof with no cuts. Normalizing mode Neg99 MC.

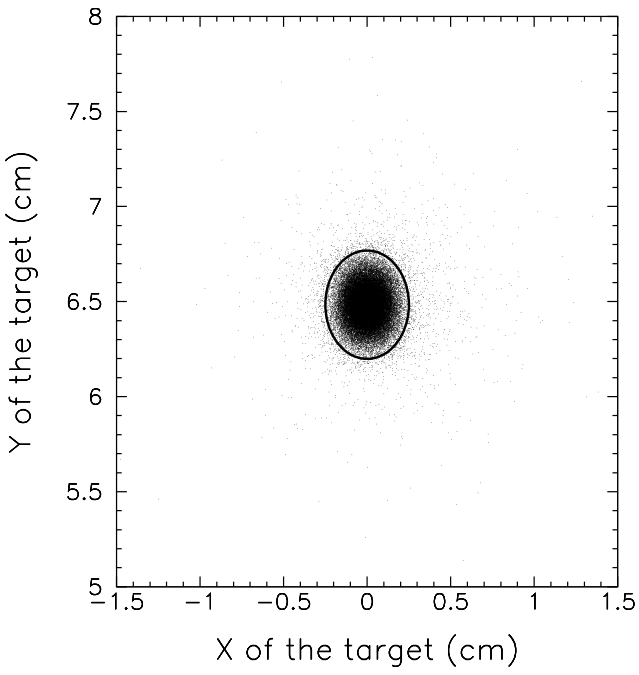

Figure 4.17. Y vs. X position of the Ω^- at the target with no cuts for the normalizing-mode Neg99 MC. Solid line — elliptical cut.

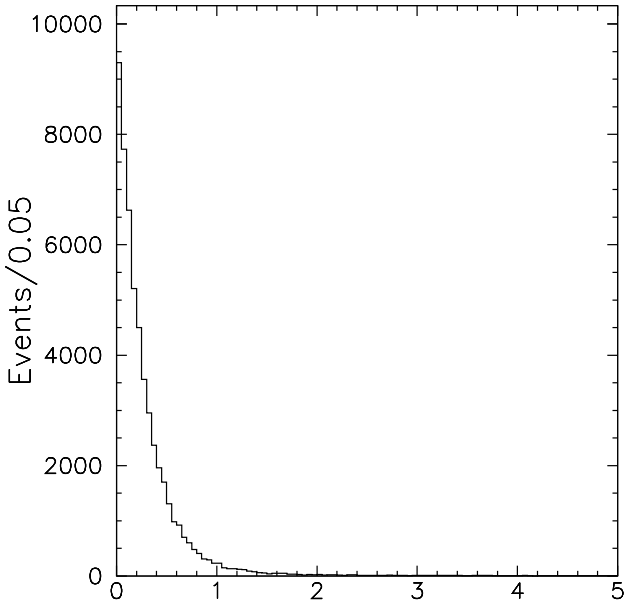

Figure 4.18. Normalized distance from the center $r = (x_{target}/0.25)^2 + ((y_{target} - 6.4835)/0.285)^2$. Normalizing mode Neg99 MC.

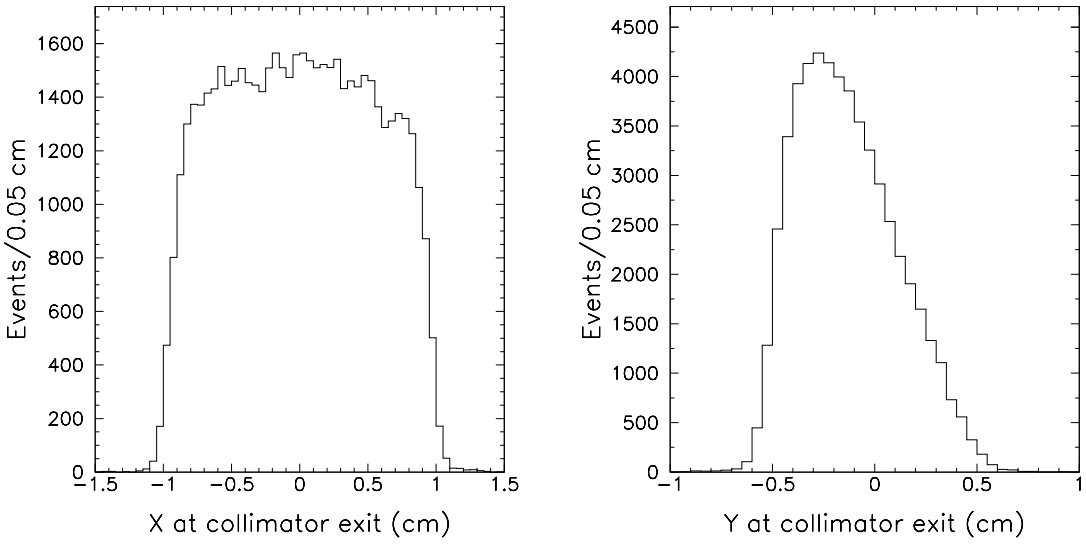

Figure 4.19. X and Y positions of the Ω^- at the collimator exit with no cuts for the normalizing-mode Neg99 MC.

Table 4.7. Parameters for the Gaussian-plus-constant fit for selected distributions (signal 3-body-mode Neg99 MC).

Distribution	Gaussian Mean	Standard Deviation
$m_{p\pi^-} - m_{\Lambda(PDG)}$	$(-1.47 \pm 0.23) \cdot 10^{-2}$ MeV/c^2	$0.85 \pm 0.23 \cdot 10^{-2}$ MeV/c^2
$m_{p\pi^-\pi^-} - m_{\Xi(PDG)}$	$(-5.95 \pm 0.41) \cdot 10^{-2}$ MeV/c^2	$1.50 \pm 0.38 \cdot 10^{-2}$ MeV/c^2
$m_{p\pi^+\pi^-\pi^-\pi^-} - m_{\Omega(PDG)}$	$(-6.64 \pm 0.55) \cdot 10^{-2}$ MeV/c^2	$2.03 \pm 0.47 \cdot 10^{-2}$ MeV/c^2
x_{target}	$(0.42 \pm 0.26) \cdot 10^{-3}$ cm	$0.10 \pm 0.14 \cdot 10^{-3}$ cm
y_{target}	$6.48 \pm 0.31 \cdot 10^{-3}$ cm	$0.11 \pm 0.24 \cdot 10^{-3}$ cm

Table 4.8. Parameters for the Gaussian-plus-constant fit for selected distributions (signal 3-body-mode Pos99 MC).

Distribution	Gaussian Mean	Standard Deviation
$m_{\overline{p}\pi^+} - m_{\Lambda(PDG)}$	$(-0.73 \pm 0.23) \cdot 10^{-2}$ MeV/c^2	$0.85 \pm 0.24 \cdot 10^{-2}$ MeV/c^2
$m_{\overline{p}\pi^+\pi^+} - m_{\Xi(PDG)}$	$(-5.58 \pm 0.41) \cdot 10^{-2}$ MeV/c^2	$1.50 \pm 0.38 \cdot 10^{-2}$ MeV/c^2
$m_{\overline{p}\pi^-\pi^+\pi^+\pi^+} - m_{\Omega(PDG)}$	$(-6.36 \pm 0.55) \cdot 10^{-2}$ MeV/c^2	$2.03 \pm 0.47 \cdot 10^{-2}$ MeV/c^2
x_{target}	$(-0.08 \pm 0.26) \cdot 10^{-3}$ cm	$0.10 \pm 0.2 \cdot 10^{-3}$ cm
y_{target}	$6.48 \pm 0.31 \cdot 10^{-3}$ cm	$0.11 \pm 0.24 \cdot 10^{-3}$ cm

4.3.2 Signal Modes. Invariant mass and target position Monte Carlo distributions for both, 3-body and resonance, signal modes were fit with Gaussian-plus-constant functions. Parameters after the fit are given in Tables 4.7 through 4.10. Corresponding distributions for the "Neg99" ("Pos99") data subset are shown in Figures 4.20 through 4.22 (Figures B.3 through B.6).

Cuts for the signal mode are given in Table 4.11. Figures 4.24 through 4.39 show 3-body- and resonance-mode "Neg99" MC distributions for each selection criterion. As well as for the normalizing mode, corresponding distributions for the "Pos99" subset look similar and we omit them. Cut efficiencies for the 3-body (resonance) mode are listed in Table 4.12 (4.13).

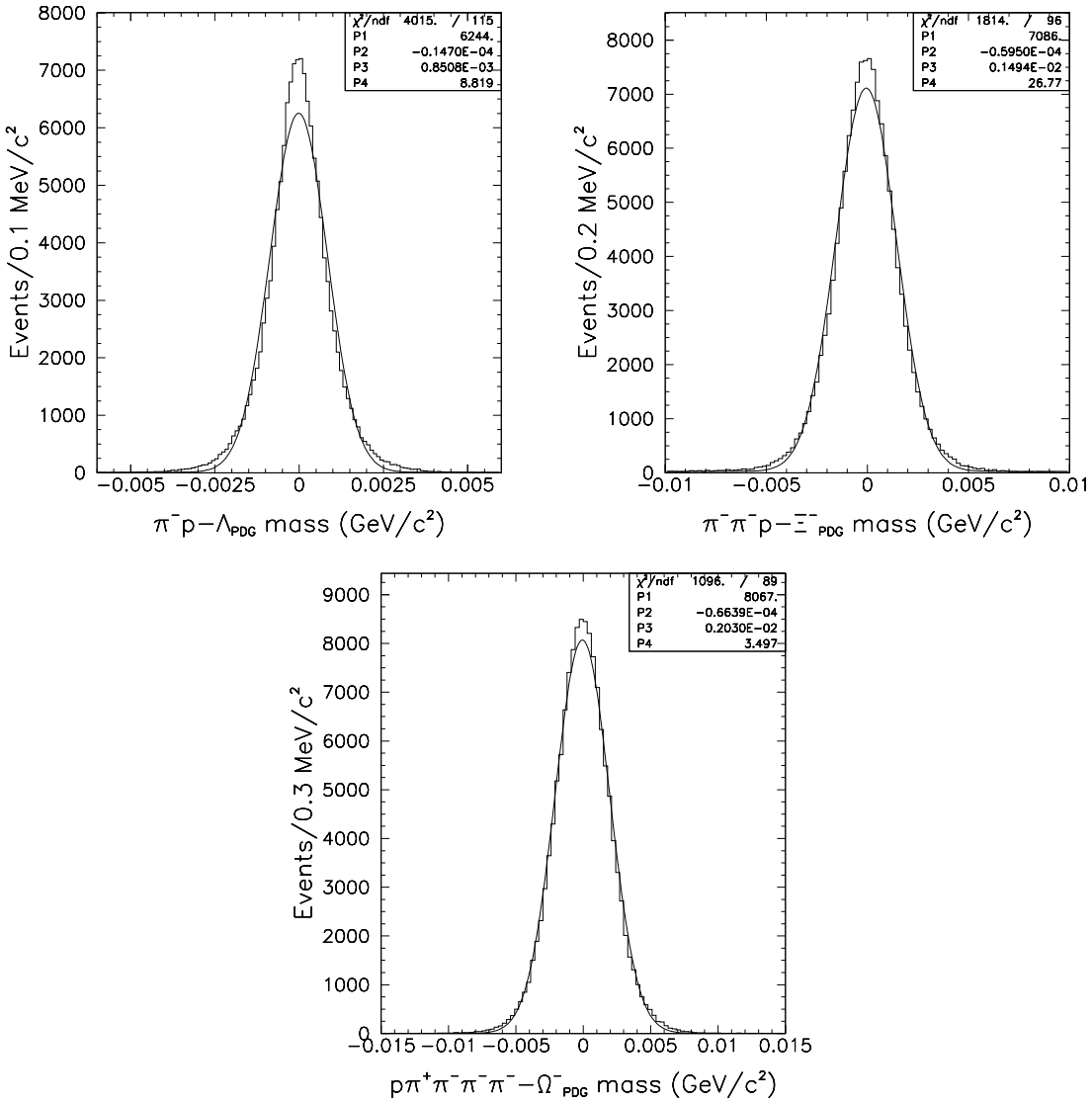

Figure 4.20. Difference between reconstructed invariant mass with no cuts and PDG values for the signal 3-body-mode Neg99 MC. Solid line is Gaussian-plus-constant fit.

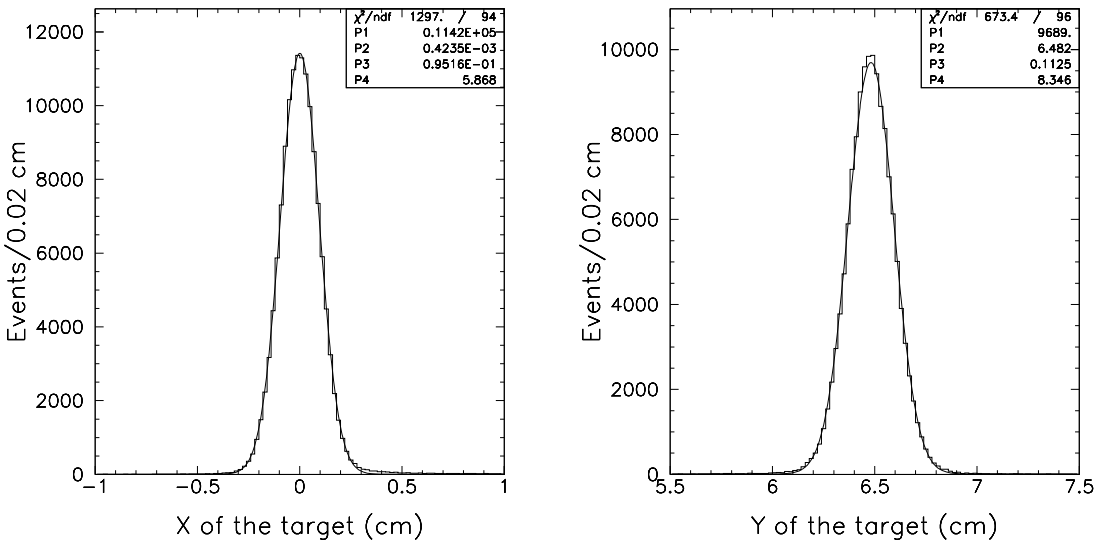

Figure 4.21. X and Y positions of the Ω^- at the target with no cuts for the signal 3-body-mode Neg99 MC. Solid line is Gaussian-plus-constant fit.

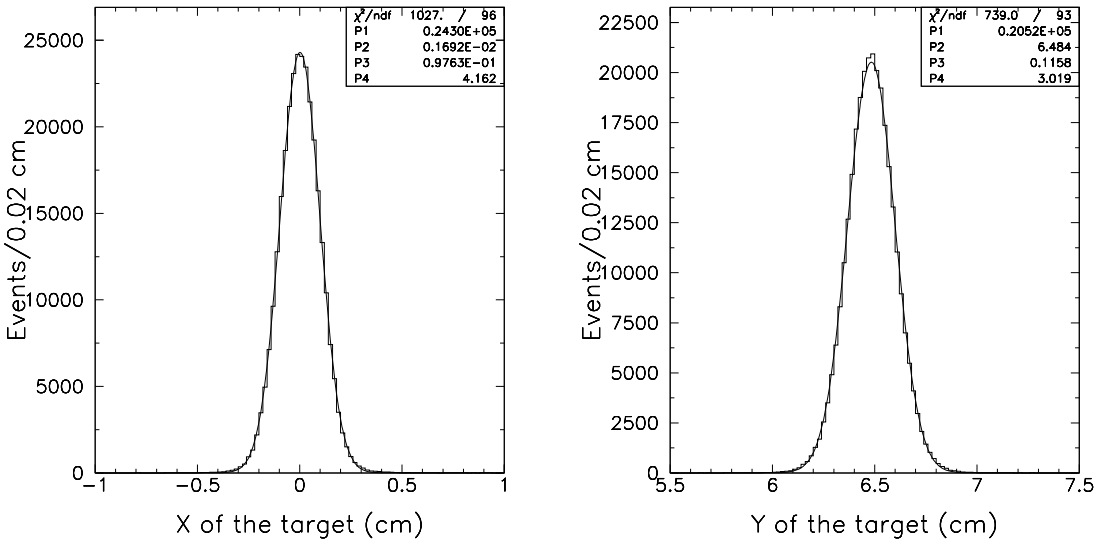

Figure 4.22. X and Y positions of the Ω^- at the target with no cuts for the signal resonance-mode Neg99 MC. Solid line is Gaussian-plus-constant fit.

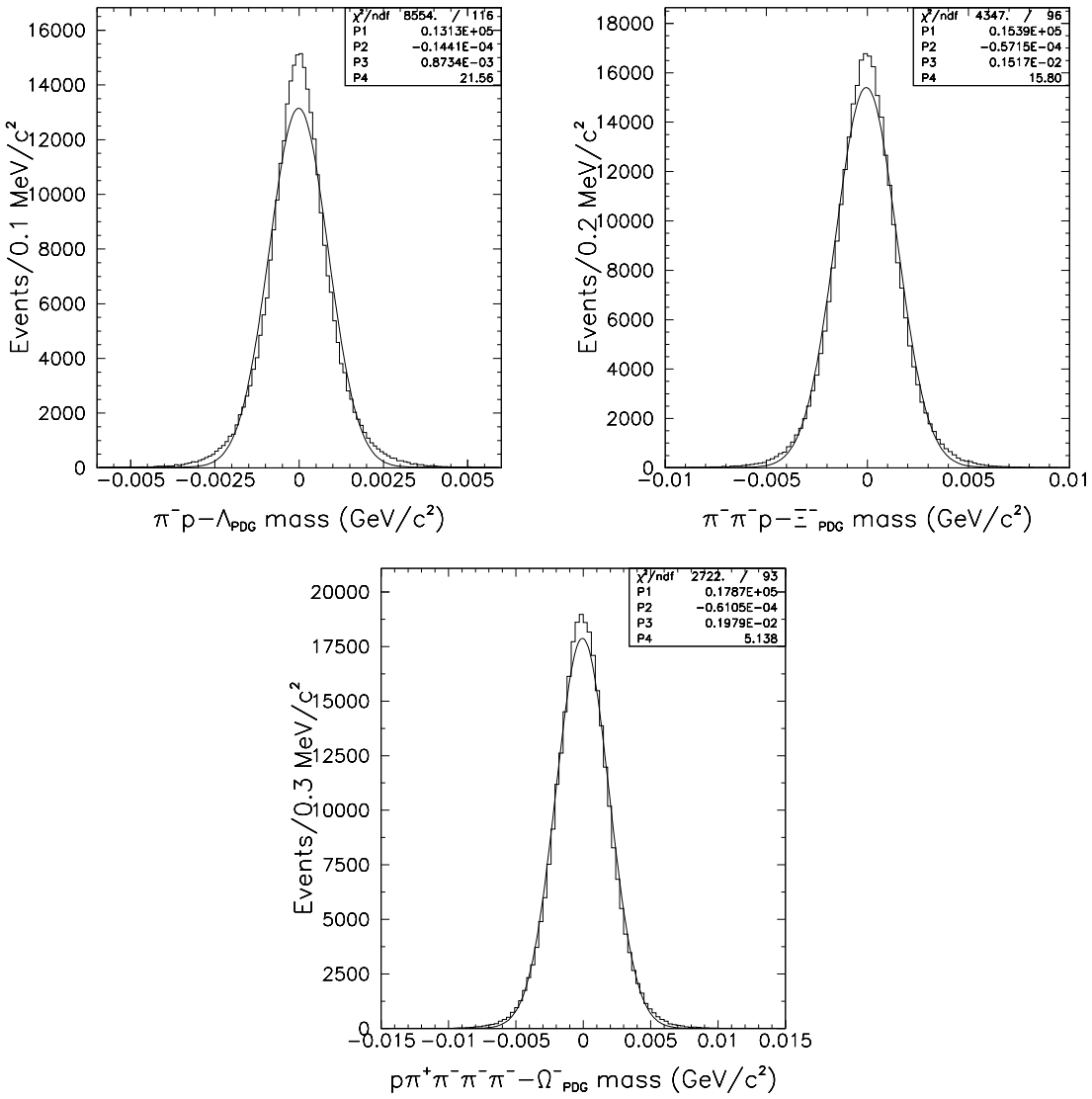

Figure 4.23. Difference between reconstructed invariant mass with no cuts and PDG values for the signal resonance-mode Neg99 MC. Solid line is Gaussian-plus-constant fit.

Table 4.9. Parameters for the Gaussian-plus-constant fit for selected distributions (signal resonance-mode Neg99 MC).

Distribution	Gaussian Mean	Standard Deviation
$m_{p\pi^-} - m_{\Lambda(PDG)}$	$(-1.44 \pm 0.16) \cdot 10^{-2}$ MeV/c^2	$0.87 \pm 0.17 \cdot 10^{-2}$ MeV/c^2
$m_{p\pi^-\pi^-} - m_{\Xi(PDG)}$	$(-5.71 \pm 0.28) \cdot 10^{-2}$ MeV/c^2	$1.52 \pm 0.26 \cdot 10^{-2}$ MeV/c^2
$m_{p\pi^+\pi^-\pi^-\pi^-} - m_{\Omega(PDG)}$	$(-6.11 \pm 0.36) \cdot 10^{-2}$ MeV/c^2	$1.98 \pm 0.31 \cdot 10^{-2}$ MeV/c^2
x_{target}	$(1.69 \pm 0.18) \cdot 10^{-3}$ cm	$0.10 \pm 0.14 \cdot 10^{-3}$ cm
y_{target}	$6.48 \pm 0.21 \cdot 10^{-3}$ cm	$0.11 \pm 0.17 \cdot 10^{-3}$ cm

Table 4.10. Parameters for the Gaussian-plus-constant fit for selected distributions (signal resonance-mode Pos99 MC).

Distribution	Gaussian Mean	Standard Deviation
$m_{\overline{p}\pi^+} - m_{\Lambda(PDG)}$	$(-1.37 \pm 0.16) \cdot 10^{-2}$ MeV/c^2	$0.87 \pm 0.17 \cdot 10^{-2}$ MeV/c^2
$m_{\overline{p}\pi^+\pi^+} - m_{\Xi(PDG)}$	$(-5.46 \pm 0.28) \cdot 10^{-2}$ MeV/c^2	$1.51 \pm 0.25 \cdot 10^{-2}$ MeV/c^2
$m_{\overline{p}\pi^-\pi^+\pi^+\pi^+} - m_{\Omega(PDG)}$	$(-5.71 \pm 0.36) \cdot 10^{-2}$ MeV/c^2	$1.97 \pm 0.31 \cdot 10^{-2}$ MeV/c^2
x_{target}	$(2.37 \pm 0.18) \cdot 10^{-3}$ cm	$0.10 \pm 0.14 \cdot 10^{-3}$ cm
y_{target}	$6.48 \pm 0.21 \cdot 10^{-3}$ cm	$0.11 \pm 0.16 \cdot 10^{-3}$ cm

Table 4.11. Selection cuts for the signal modes.

Cut Type	Selection Rule	Cut ID
$p(\overline{p})\pi^{\mp}$ invariant mass	$\lvert m_{p(\overline{p})\pi^{\mp}} - m_{\Lambda(PDG)}\rvert \leq 2.55$ MeV	S1
$p(\overline{p})\pi^{\mp}\pi^{\mp}$ invariant mass	$\lvert m_{p(\overline{p})\pi^{\mp}\pi^{\mp}} - m_{\Xi(PDG)}\rvert \leq 4.50$ MeV	S2
$p(\overline{p})\pi^{\pm}\pi^{\mp}\pi^{\mp}\pi^{\mp}$ invariant mass	$\lvert m_{p(\overline{p})\pi^{\pm}\pi^{\mp}\pi^{\mp}\pi^{\mp}} - m_{\Omega(PDG)}\rvert \leq 6.09$ MeV	S3
$\Omega^{\mp}$ total momentum	$135 \leq P_{\Omega} \leq 220$ GeV	S4
Z coordinate of the particle vertex	$50 < \mathrm{Z}_{\Omega} < 1300$ cm	S5
	$\mathrm{Z}_{\Omega} < \mathrm{Z}_{\Xi} < \mathrm{Z}_{\Lambda}$ cm	S6
	$\mathrm{Z}_{\Lambda} < 1300$ cm	S7
Distance of closest approach	$\mathrm{DOCA}_{\Omega} < 0.45$ cm	S8
	$\mathrm{DOCA}_{\Lambda} < 0.3$ cm	S9
	$\mathrm{DOCA}_{\Xi} < 0.35$ cm	S10
Decay geometry fitter	$(\chi^2/dof)_{\Lambda} < 2$	S11
	$(\chi^2/dof)_{decay} < 2.2$	S12
$\Omega^{\mp}$ position at the target	$[(x_{target}/0.27)^2 +$	
	$((y_{target} - 6.4822)/0.3)^2] \leq 1$	S13
$\Omega^{\mp}$ at the collimator exit	-1 cm $\leq exit_x \leq 1$ cm	S14
	-0.65 cm $\leq exit_y \leq 0.55$ cm	S15

Table 4.12. Efficiency of selection cuts for the signal 3-body-mode MC.

	Isolated Effic., %		Final Effic., %	
Cut ID	Neg99	Pos99	Neg99	Pos99
S1	97.9	97.8	98.8	98.8
S2	97.2	97.2	99.6	99.6
S3	99.0	99.0	99.8	99.8
S4	100	100	100	100
S5	82.8	82.6	81.4	81.2
S6	91.7	91.9	93.0	93.1
S7	77.1	77.2	76.3	76.4
S8	96.7	96.8	99.7	99.7
S9	97.7	97.7	99.7	99.6
S10	97.9	98.0	99.2	99.2
S11	93.8	93.8	97.9	98.0
S12	94.4	94.5	98.8	98.8
S13	95.6	95.7	98.4	98.5
S14	98.5	98.5	99.1	99.1
S15	99.1	99.1	99.8	99.7
All cuts	49.9	50.0		

Table 4.13. Efficiency of selection cuts for the signal resonance-mode MC.

	Isolated Effic., %		Final Effic., %	
Cut ID	Neg99	Pos99	Neg99	Pos99
S1	97.6	97.5	98.7	98.6
S2	98.4	98.4	99.6	99.6
S3	99.1	99.0	99.8	99.8
S4	100	100	100	100
S5	82.5	82.6	81.2	81.2
S6	93.5	93.4	92.8	92.6
S7	77.0	76.9	77.1	76.9
S8	98.1	98.1	99.5	99.6
S9	98.9	98.9	99.7	99.7
S10	98.7	98.7	99.2	99.1
S11	94.3	94.2	97.8	97.8
S12	95.1	95.1	98.2	98.2
S13	96.2	96.2	98.0	98.1
S14	98.9	98.9	99.1	99.1
S15	99.4	99.4	99.7	99.7
All cuts	50.0	49.9		

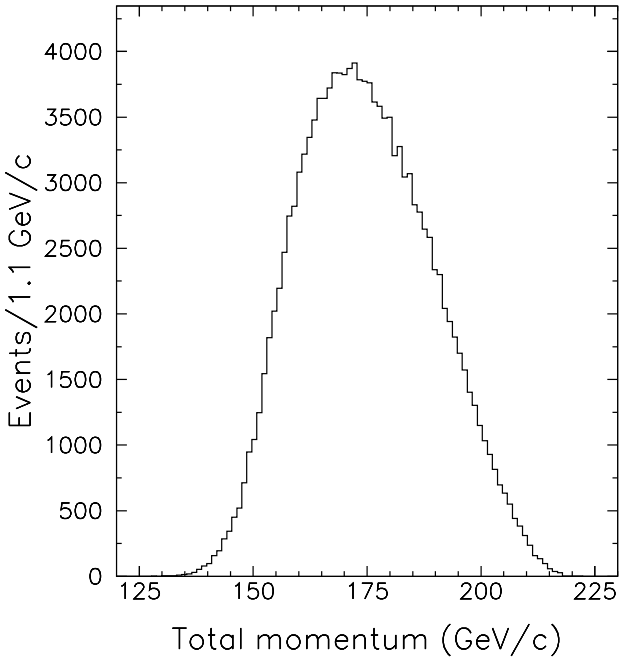

Figure 4.24. Total momentum of Ω^- with no cuts for the signal 3-body mode Neg99 MC.

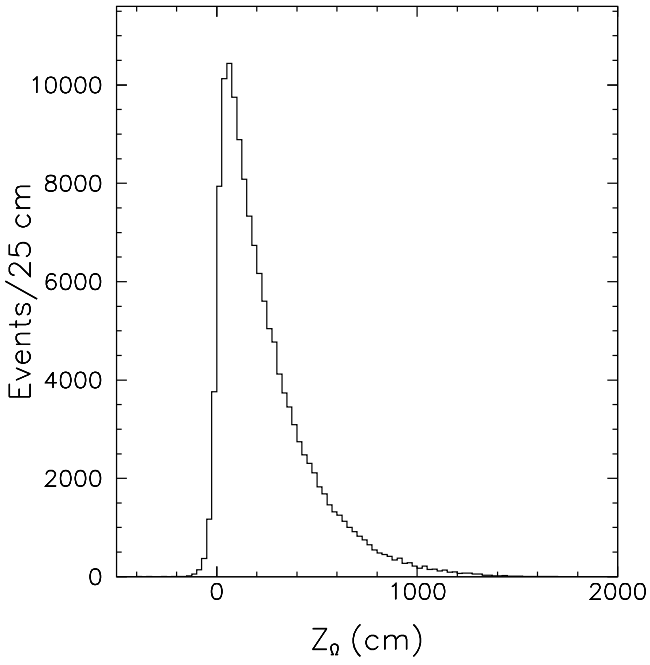

Figure 4.25. Z position of the decay vertex with no cuts for Ω^-. Signal 3-body mode Neg99 MC.

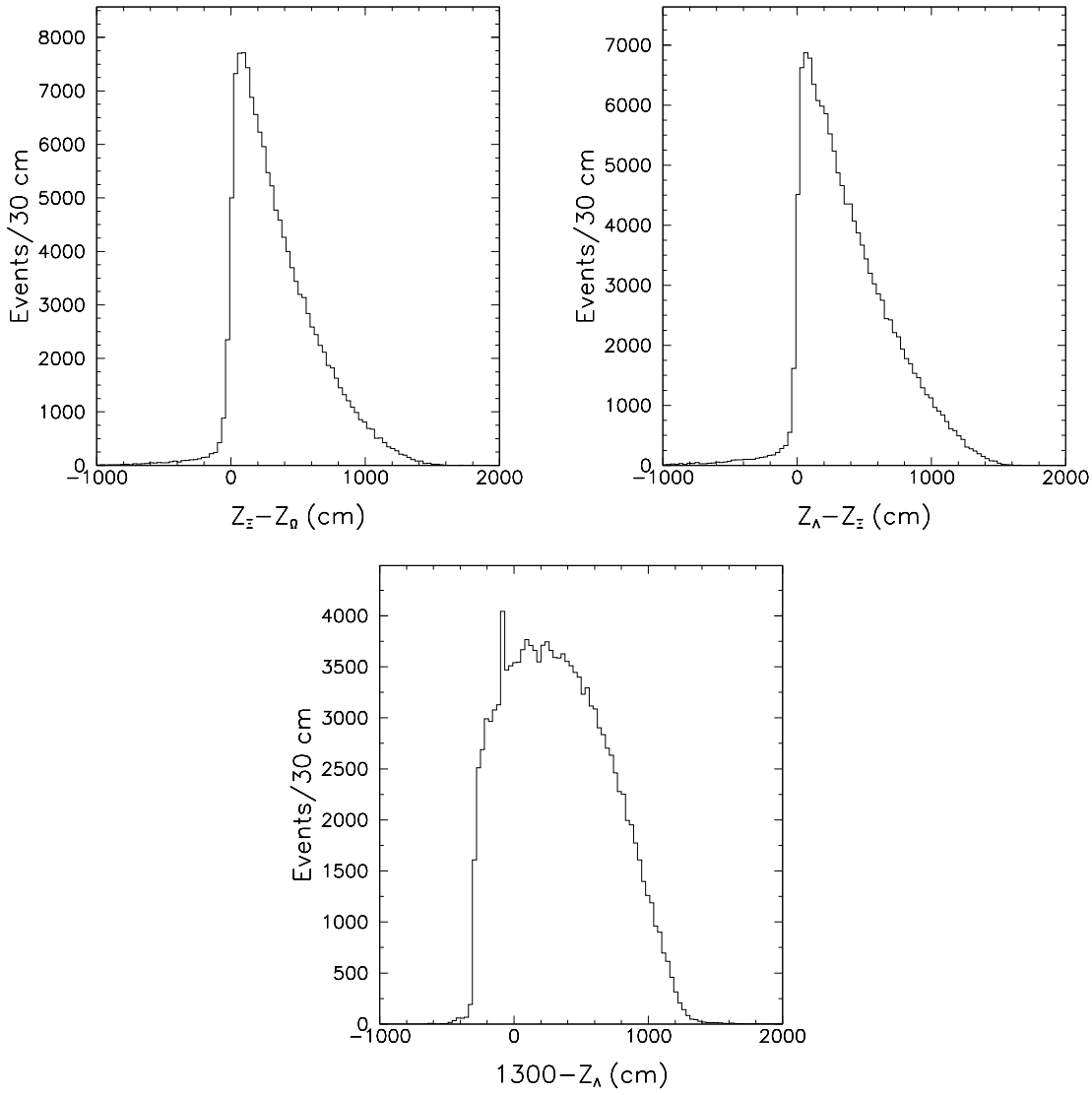

Figure 4.26. Z position of the decay vertex with no cuts. Signal 3-body mode Neg99 MC.

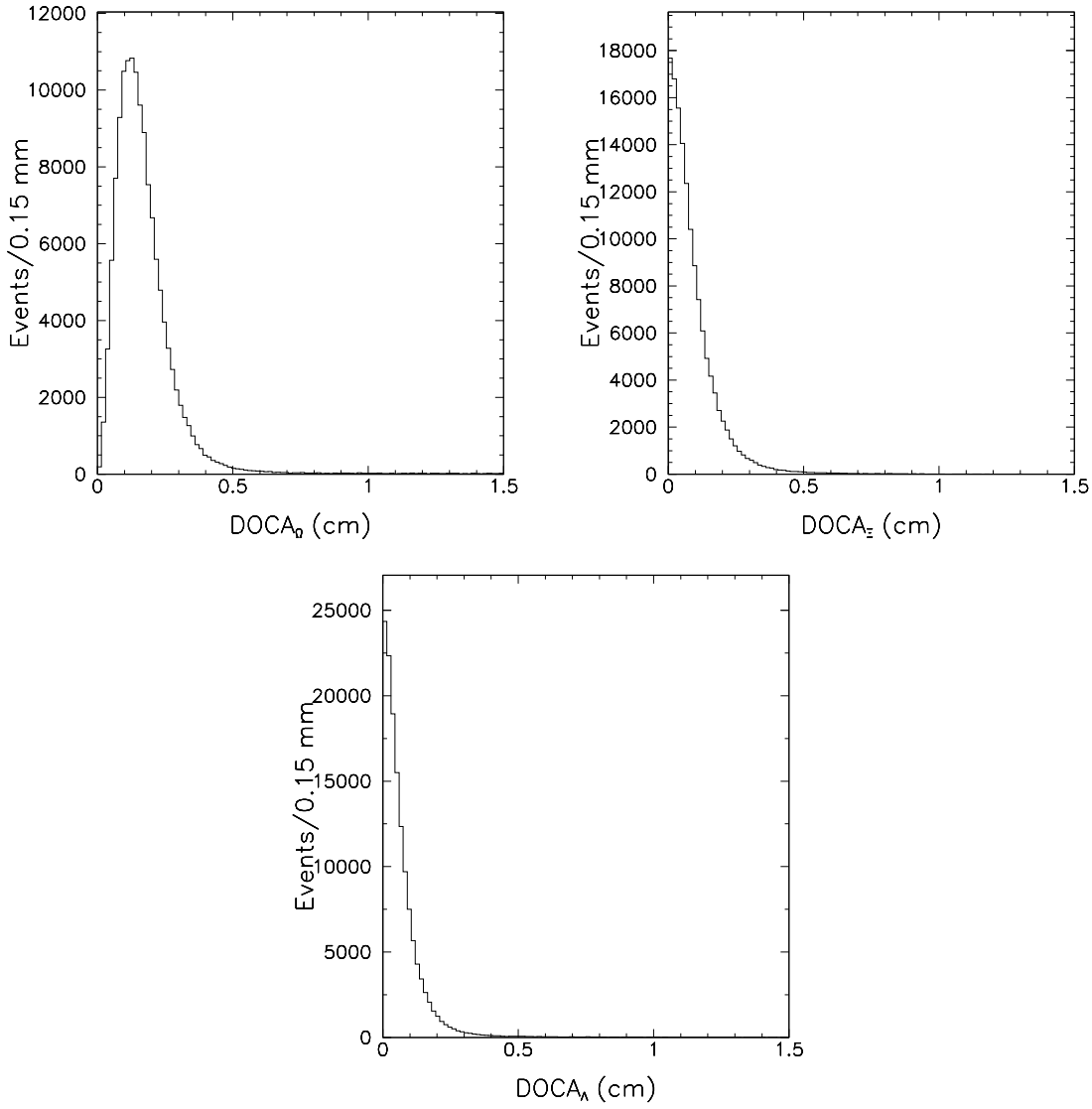

Figure 4.27. Distance of closest approach with no cuts. Signal 3-body mode Neg99 MC.

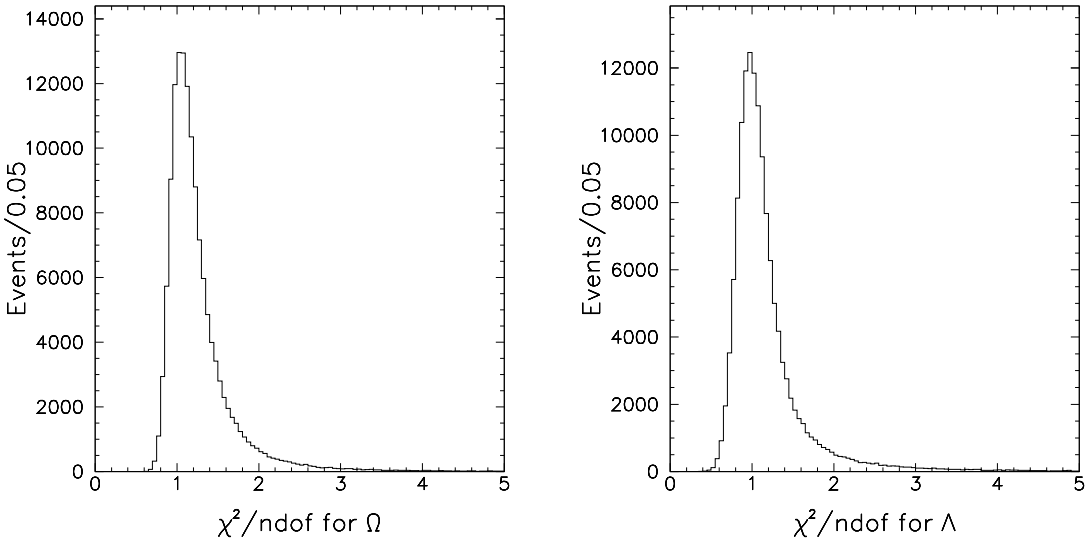

Figure 4.28. Calculated χ^2/dof with no cuts. Signal 3-body mode Neg99 MC.

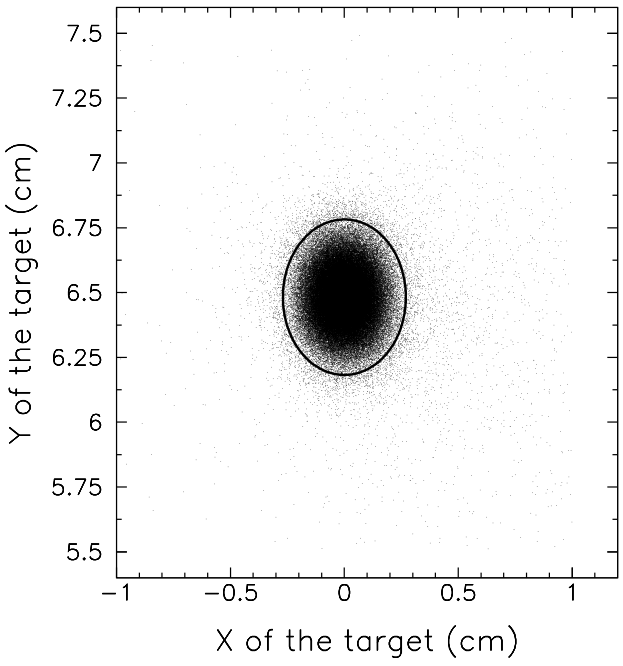

Figure 4.29. Y vs. X position of the Ω^- at the target with no cuts for the signal 3-body mode Neg99 MC. Solid line is elliptical cut.

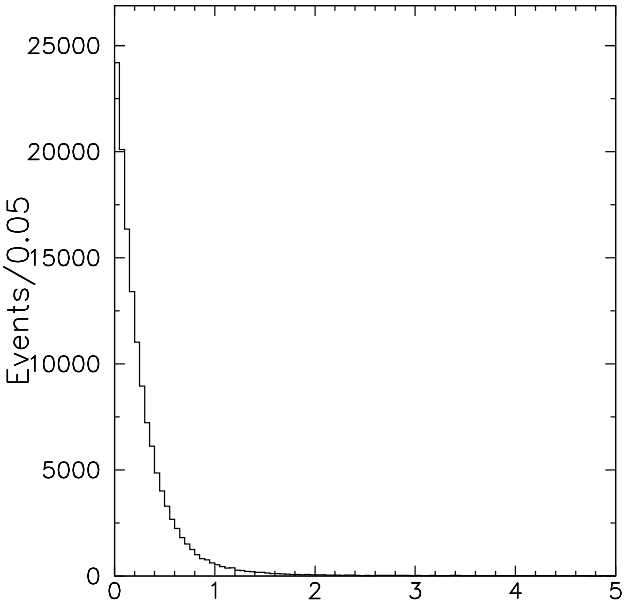

Figure 4.30. Normalized distance from the center $r = (x_{target}/0.27)^2 + ((y_{target} - 6.4822)/0.3)^2$. Signal 3-body mode Neg99 MC.

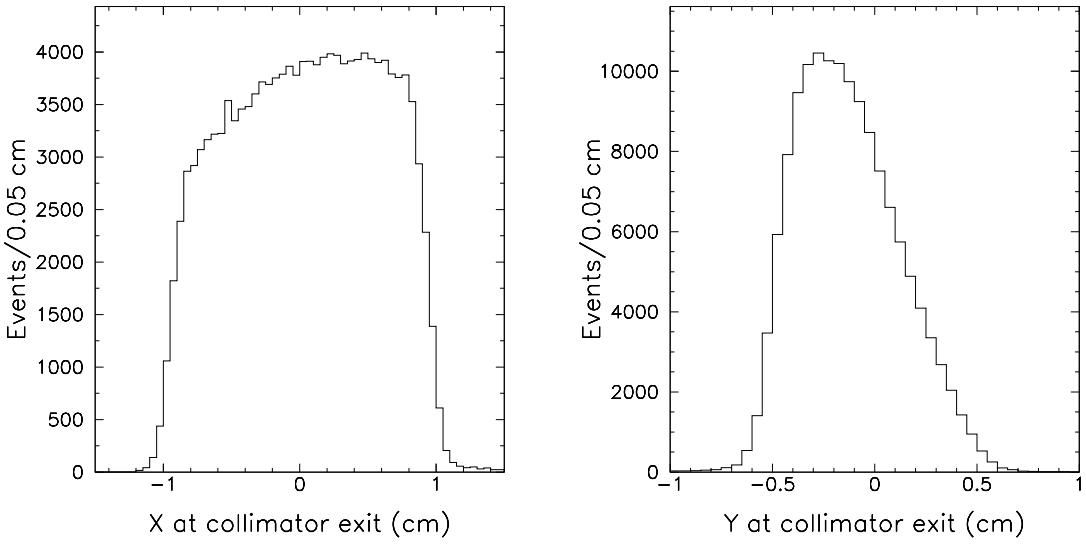

Figure 4.31. X and Y positions of the Ω^- at the collimator exit with no cuts for the signal 3-body mode Neg99 MC.

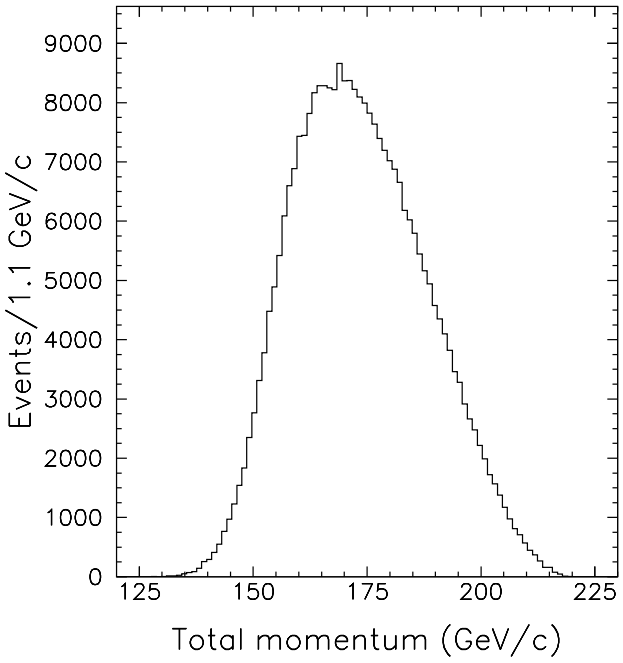

Figure 4.32. Total momentum of Ω^- with no cuts for the signal resonance mode Neg99 MC.

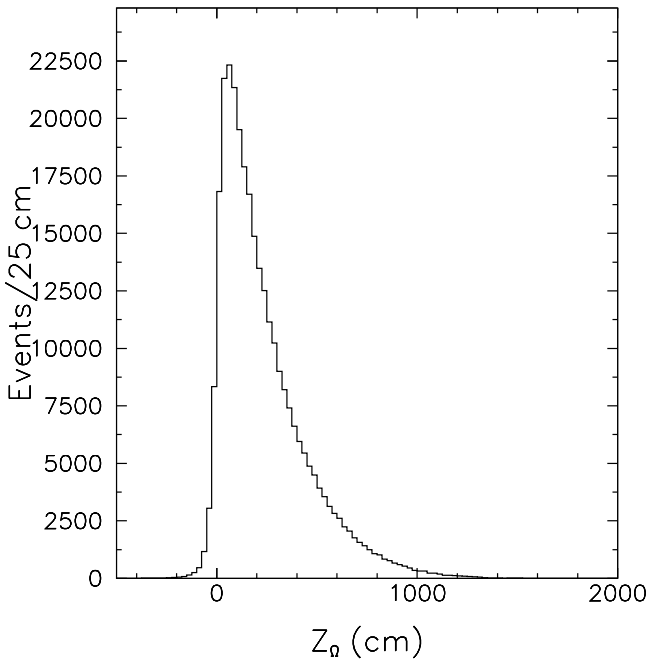

Figure 4.33. Z position of the decay vertex with no cuts for Ω^-. Signal resonance mode Neg99 MC.

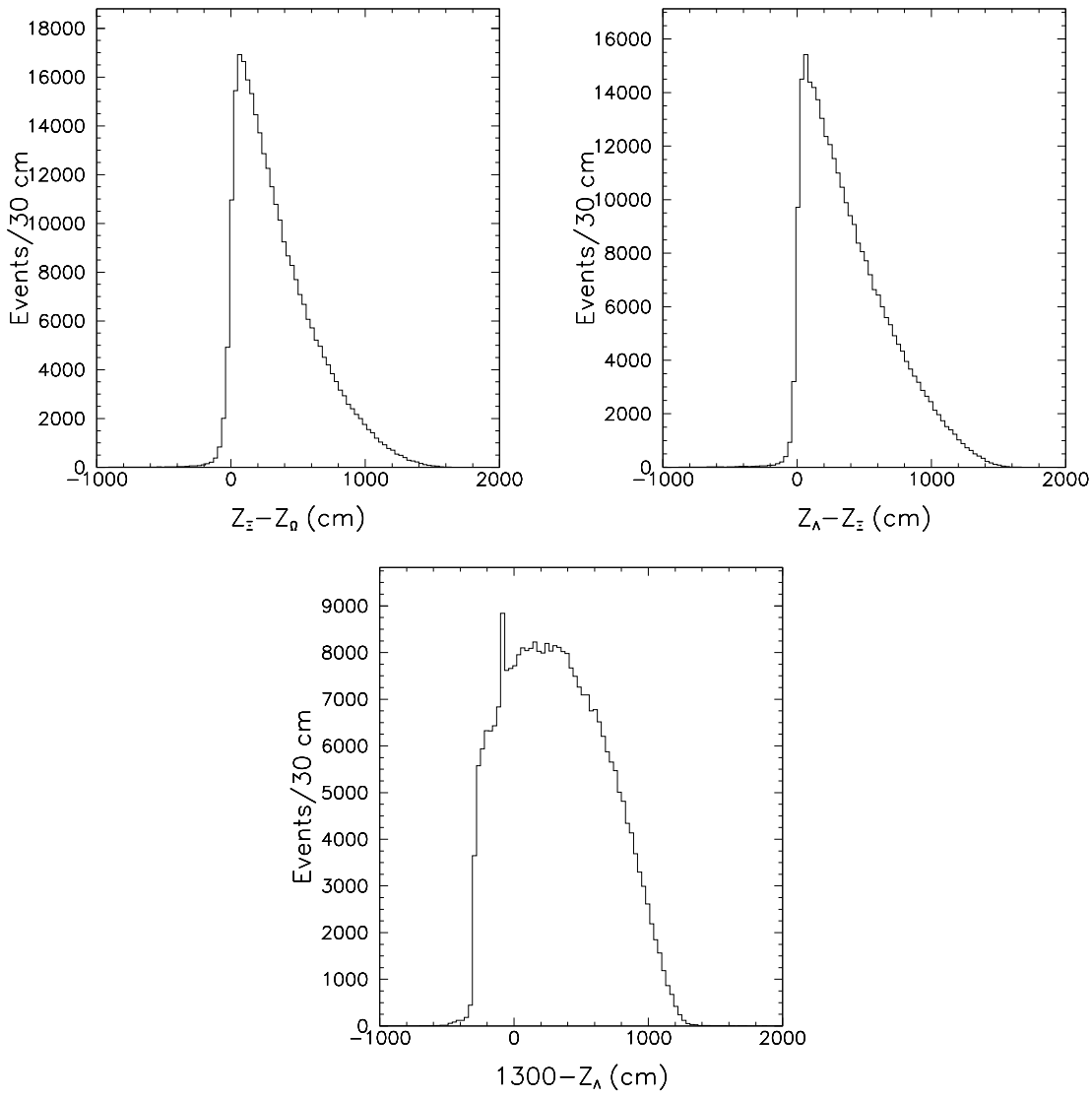

Figure 4.34. Z position of the decay vertex with no cuts. Signal resonance mode Neg99 MC.

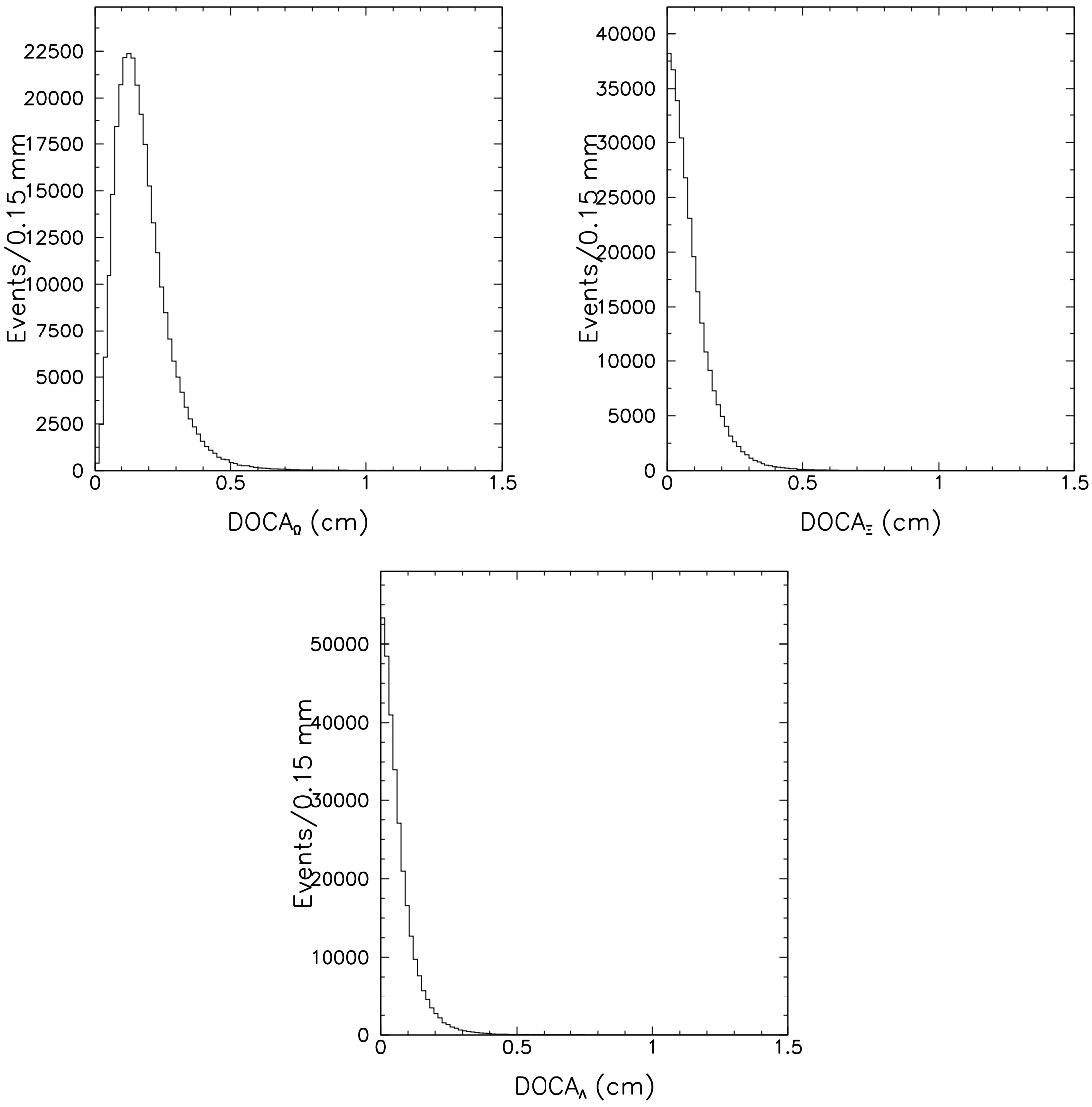

Figure 4.35. Distance of closest approach with no cuts. Signal resonance mode Neg99 MC.

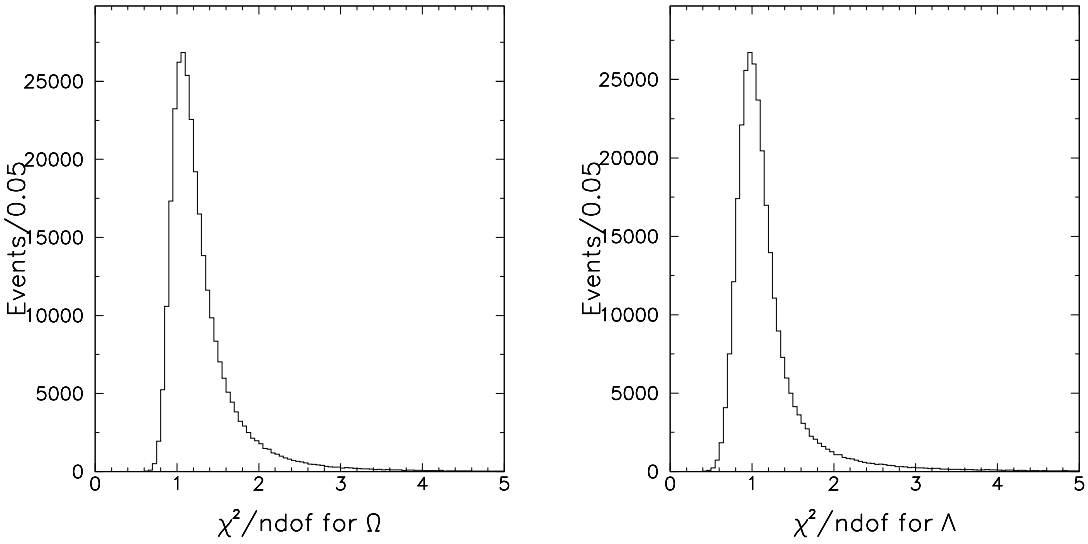

Figure 4.36. Calculated χ^2/dof with no cuts. Signal resonance mode Neg99 MC.

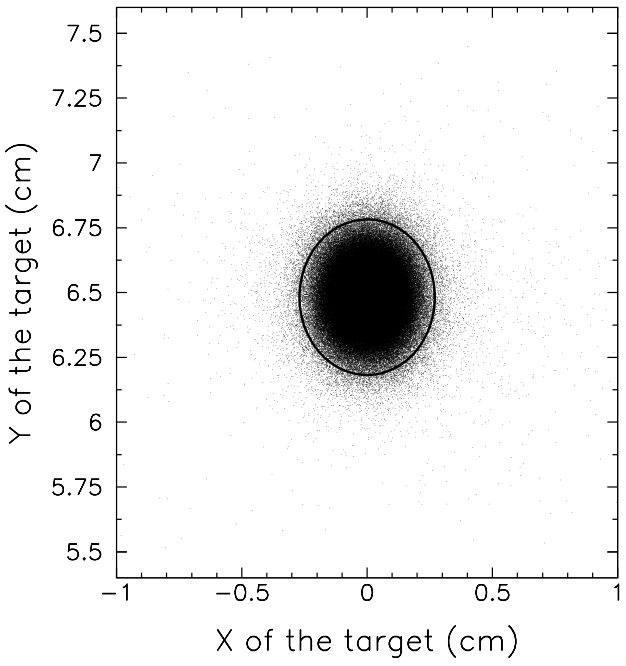

Figure 4.37. Y vs. X position of the Ω^- at the target with no cuts for the signal resonance mode Neg99 MC. Solid line is elliptical cut.

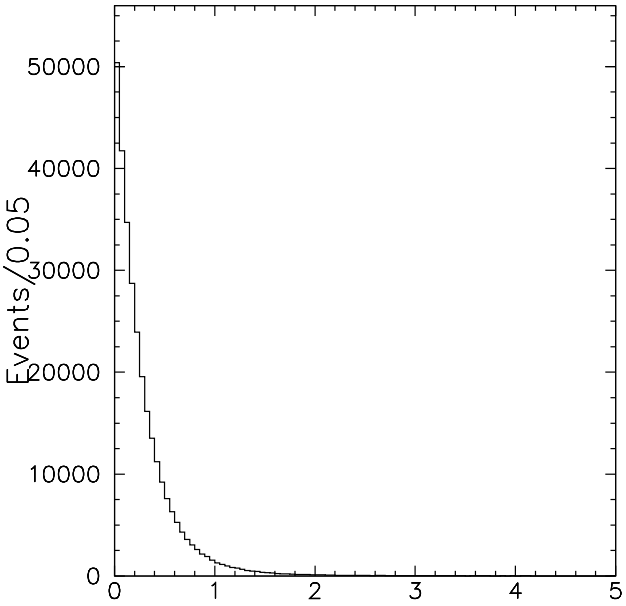

Figure 4.38. Normalized distance from the center $r = (x_{target}/0.27)^2 + ((y_{target} - 6.4822)/0.3)^2$. Signal resonance mode Neg99 MC.

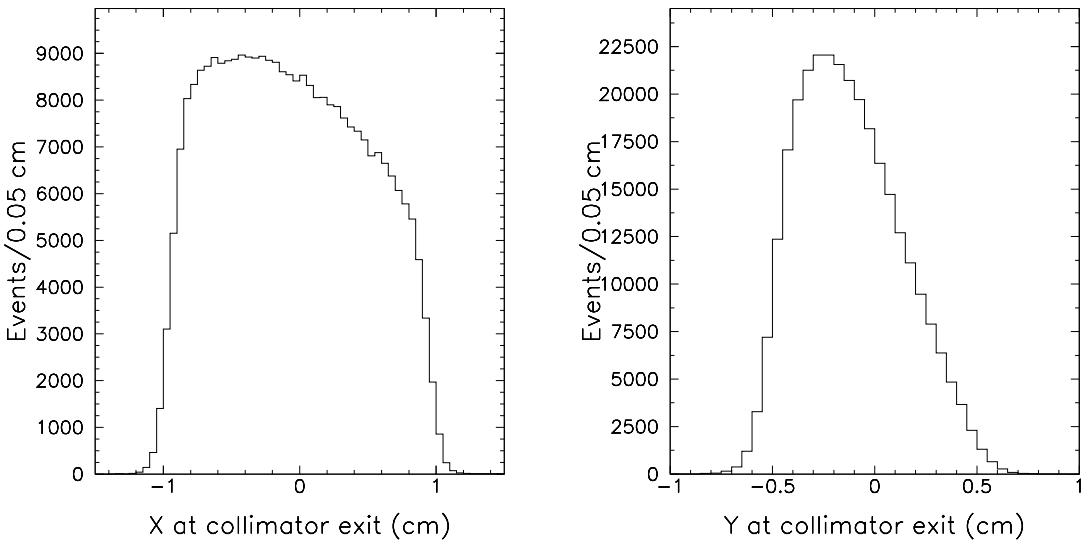

Figure 4.39. X and Y positions of the Ω^- at the collimator exit with no cuts for the signal resonance mode Neg99 MC.

4.4 Monte Carlo Tuning and Comparison with Data

The Monte Carlo was tuned to get a reasonable match with the data. We used the normalizing mode for the tuning for two reasons: first, it has more events than the signal mode and second, because tuning using the signal mode might bias our final result. In the MC we varied the parameters for generation of Ω at the target. The probability density function for the Ω momentum in p_x, p_y, p_z was varied arbitrarily. The position of the beam and the center of the target in x and y were varied by 0.1 mm until reasonable agreement between data and MC was reached.

We employed the Kolmogorov test to compare data with MC. All cuts from Table 4.5 (4.11) were applied to the data and the normalizing (signal) mode MC. Kolmogorov test probabilities for selected variables after tuning are given in Table 4.14 (4.15) for the Neg99 (Pos99) subset. Corresponding Neg99 (Pos99) data subset distributions together with other variables are plotted in Figures 4.40 to 4.44 (C.1 to C.5) for the normalizing mode and in Figures 4.45 to 4.49 (C.6 to C.10) for the signal modes. One can see that indeed there is a reasonable, although not perfect, match between data and MC. For completeness, numbers of events for each mode and each data subset are listed in Table 4.16.

Table 4.14. Kolmogorov test probabilities (in percent) from data and MC comparison for selected variables for the Neg99 subset.

Variable	Normalizing mode	Signal mode
p_x for Ω^-	86.7	13.8
p_y for Ω^-	30.6	38.9
p_z for Ω^-	2.8	10.3
x_{target} for Ω^-	2.4	7.7
y_{target} for Ω^-	48.4	60.9
x_{exit} for Ω^-	95.9	20.8
y_{exit} for Ω^-	9.2	99.5

Table 4.15. Kolmogorov test probabilities (in percent) from data and MC comparison for selected variables for the Pos99 subset.

Variable	Normalizing mode	Signal mode
p_x for Ω^+	91.0	91.6
p_y for Ω^+	5.2	100
p_z for Ω^+	8.3	97.8
x_{target} for Ω^+	16.0	55.9
y_{target} for Ω^+	23.3	71.1
x_{exit} for Ω^+	93.5	84.8
y_{exit} for Ω^+	50.0	24.4

Table 4.16. Number of events in each of the data samples after all cuts.

Mode	Negative99	Positive99
Normalizing	375	156
Signal	78	24

4.4.1 Remarks on histogram comparisons. There are more than one goodness-of-fit test that can be used to compare a measured distribution (histogram) to a MC prediction. In this section we explain why the Kolmogorov test has been chosen for this analysis.

Undoubtedly, the most popular and widespreaded goodness-of-fit test is the χ^2 (chi-squared) test. However, it has one large disadvantage. Its results strongly depend on the number of bins and number of events within a bin. To test this we have created three MC and three data histograms with differing binning. Tests have been performed with the same data events. Results are summarized in Table 4.17. Corresponding histograms are plotted in Figure 4.50. One can see that the χ^2 test strongly depends on the binning and the resulting probabilities of compatibility between data and MC histograms can differ by orders of magnitude. In contrast, the Kolmogorov test returns a unique probability value.

Furthermore, we have to satisfy other requirements to perform a reliable χ^2 test. For example, the number of events within a bin should be large enough so that the actual Poisson distribution of errors approximates a Gaussian. Various authors suggest various rules for an optimal data binning. We have tried to satisfy the criteria not to have bins with fewer than five events and not to have more than several bins with $\leq$10 events. In the case of small data-sample size, which is exactly what we have, the task of choosing optimal binning becomes even harder (more detailed discussion may be found in references [33] and [22]).

Table 4.17. Probabilities for χ^2 test with differing binning and the Kolmogorov test. The same data events were used in all tests.

Test	Probability, %	Figure
χ^2, 8 bins	6.8	4.50a
χ^2, 10 bins	0.09	4.50b
χ^2, 12 bins	14.78	4.50c
Kolmogorov	1.213	

Contrary to the χ^2 test, the Kolmogorov test does not require binning. It is restricted to univariate distributions. Since we deal with one-dimensional low statistics histograms, the Kolmogorov test is perfectly suitable for us. In the Physics Analysis Workstation (PAW) software package the Kolmogorov test is implemented through the command `/HIST/OPER/DIFF` [7]. To employ it we must store our data in a histogram which is a confusing requirement for the Kolmogorov test. However, if our bin width is small compared with experimental resolution or the number of bins is very large compared with the number of events, then we can confidently use it. To be on the safe side all our histograms for the Kolmogorov test have been created with 3×10^5 bins. We also request that overflow and underflow bins be taken into account while performing histogram comparison.

To check the Kolmogorov test implementation within PAW we have generated

an exponential distribution, uniform distribution, and their mixture with 95% from the exponential and 5% from the uniform distributions. These was compared with purely exponential and flat distributions. Probabilities of compatibility between the histograms are given in Table 4.18. We can infer that the Kolmogorov test is a powerful test and 6% probability of compatibility can be considered an excellent match. Normalized to the same number of entries, these distributions are plotted in Figure 4.51.

Table 4.18. The probability of compatibility between the histograms.

Histogram 1	Histogram 2	Probability, %
exp, $5 \cdot 10^4$ entries	exp, 10^3 entries	94.02
exp, $5 \cdot 10^4$ entries	flat, 10^3 entries	0
exp, $5 \cdot 10^4$ entries	95% exp + 5% flat, 10^3 entries	6.72
exp, 10^3 entries	95% exp + 5% flat, 10^3 entries	94.68
flat, 10^3 entries	95% exp + 5% flat, 10^3 entries	0

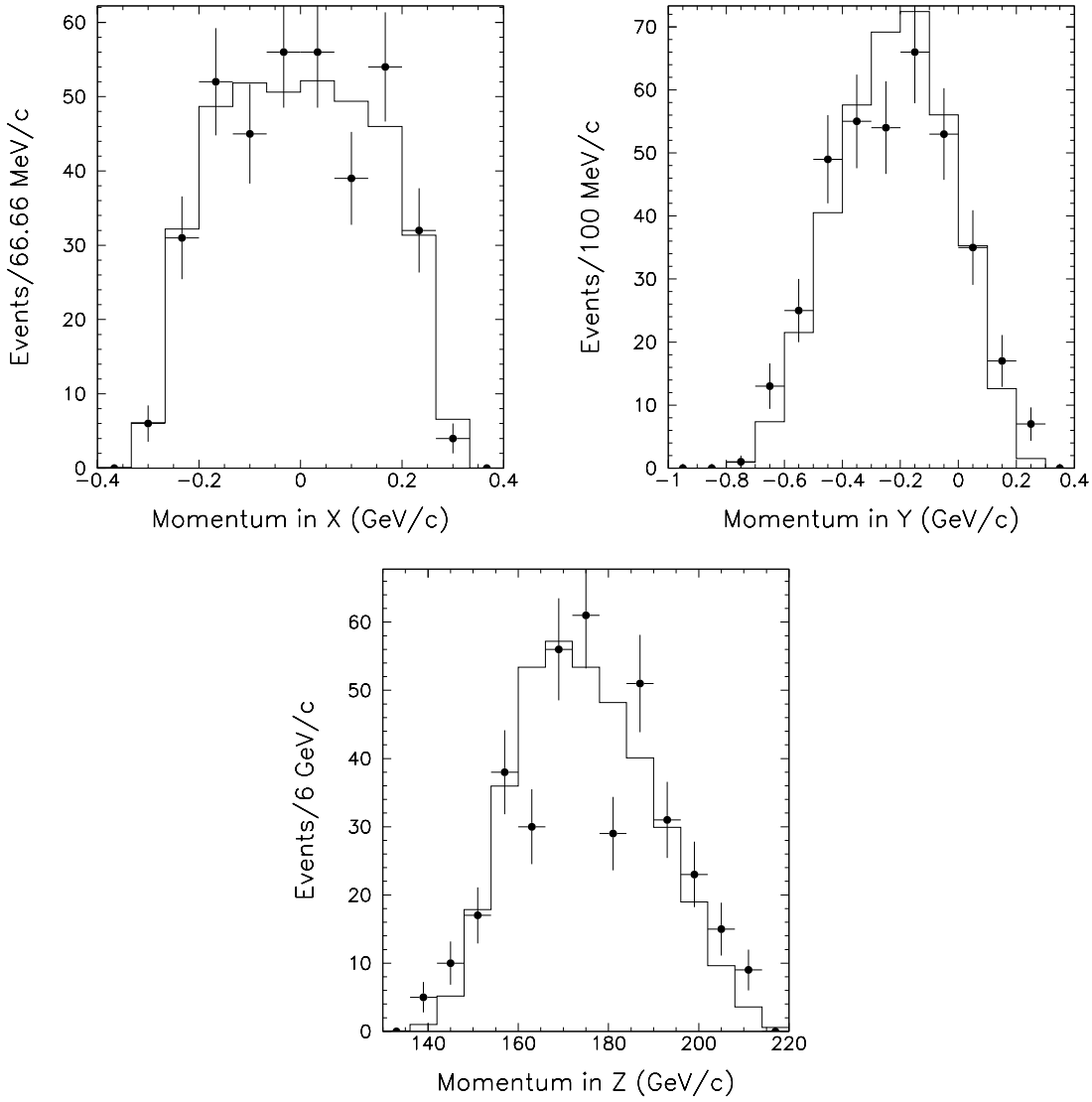

Figure 4.40. Data (Neg99) and MC comparison for x, y, and z projections of the Ω^- momentum after the cuts. Normalizing mode.

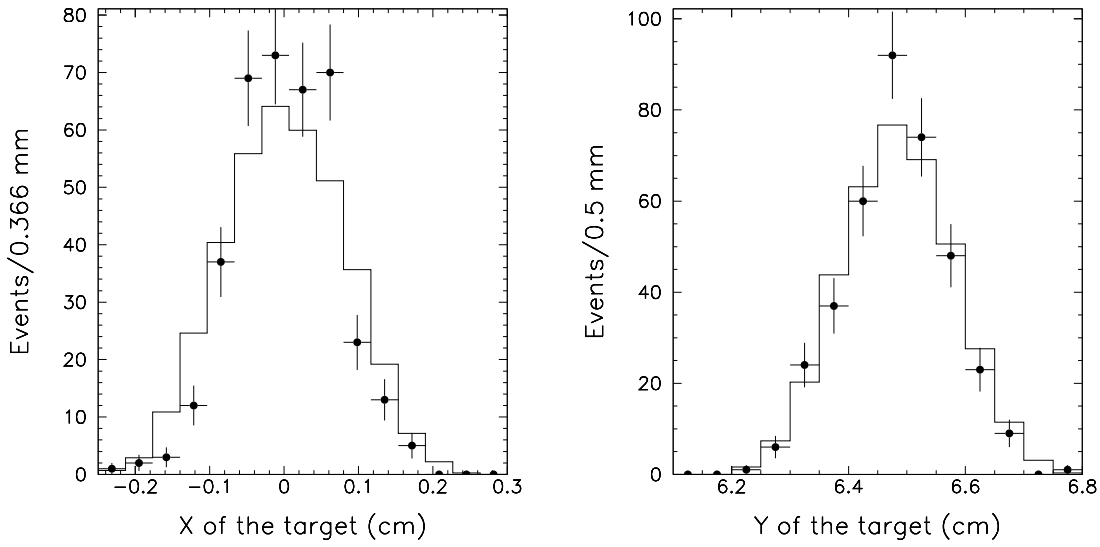

Figure 4.41. Data (Neg99) and MC comparison for x and y positions of the Ω^- at the target after the cuts. Normalizing mode.

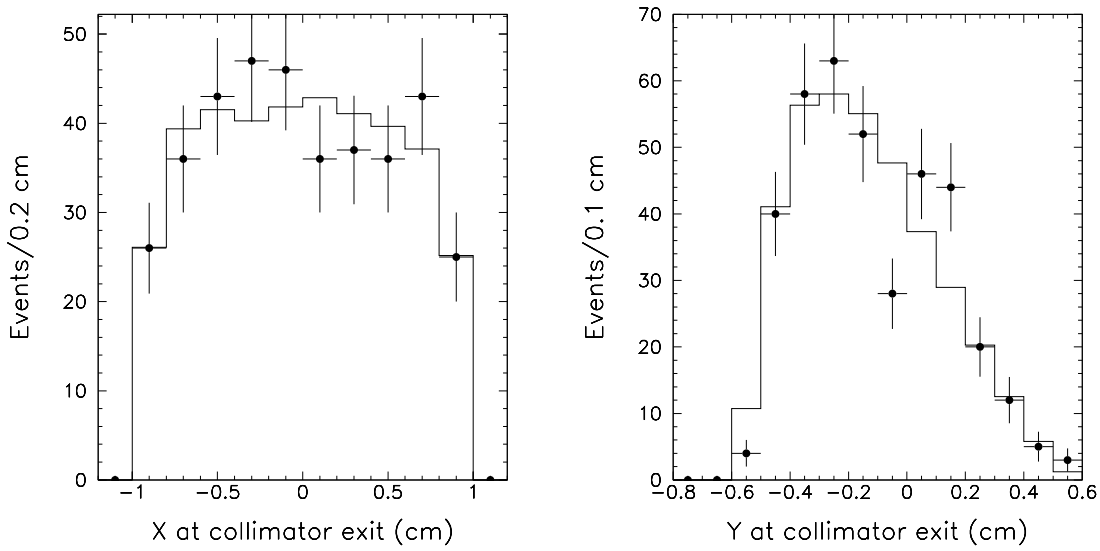

Figure 4.42. Data (Neg99) and MC comparison for x and y positions of the Ω^- at the collimator exit after the cuts. Normalizing mode.

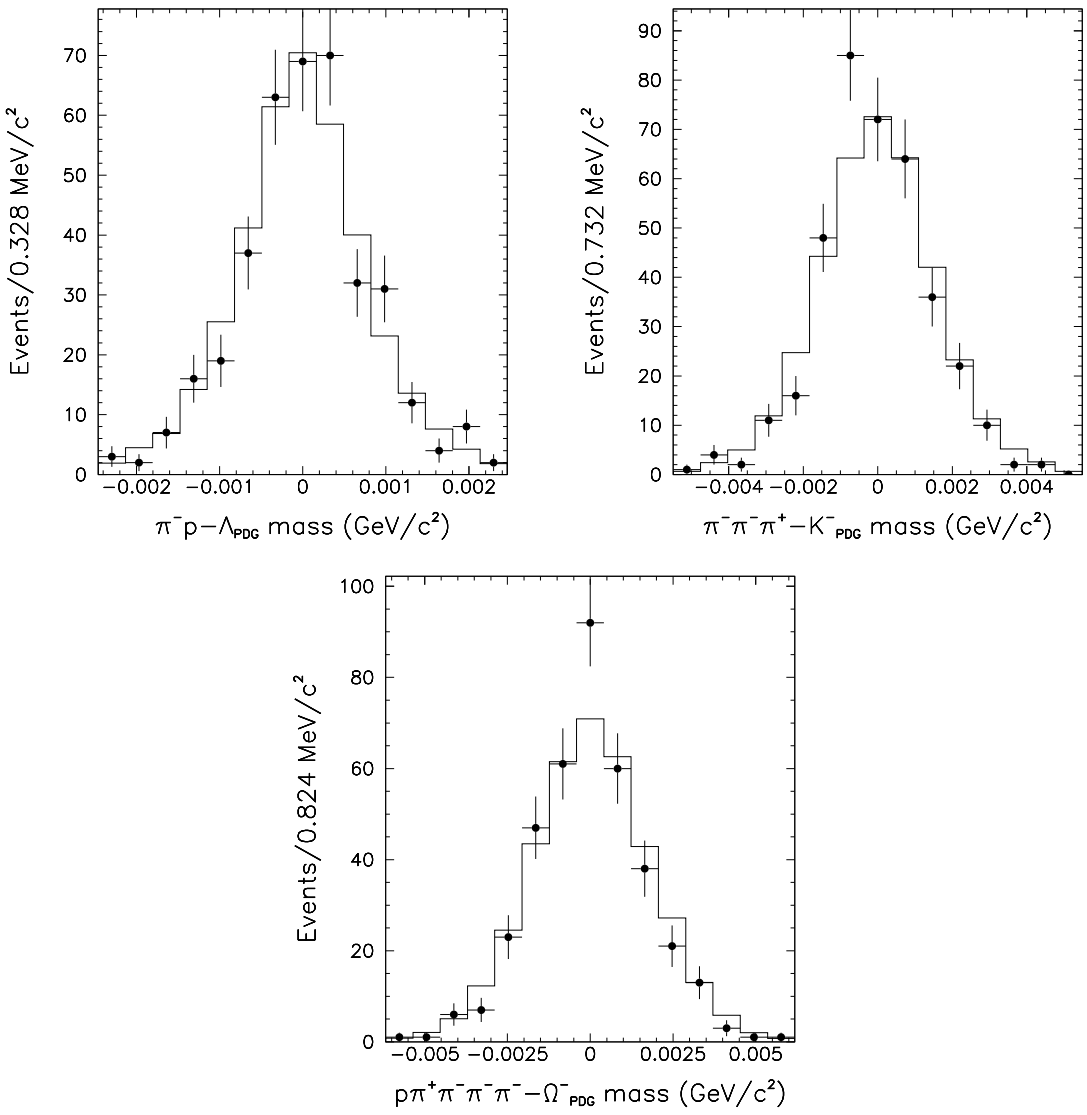

Figure 4.43. Data (Neg99) and MC comparison for the difference between reconstructed invariant mass after the cuts and PDG values. Normalizing mode.

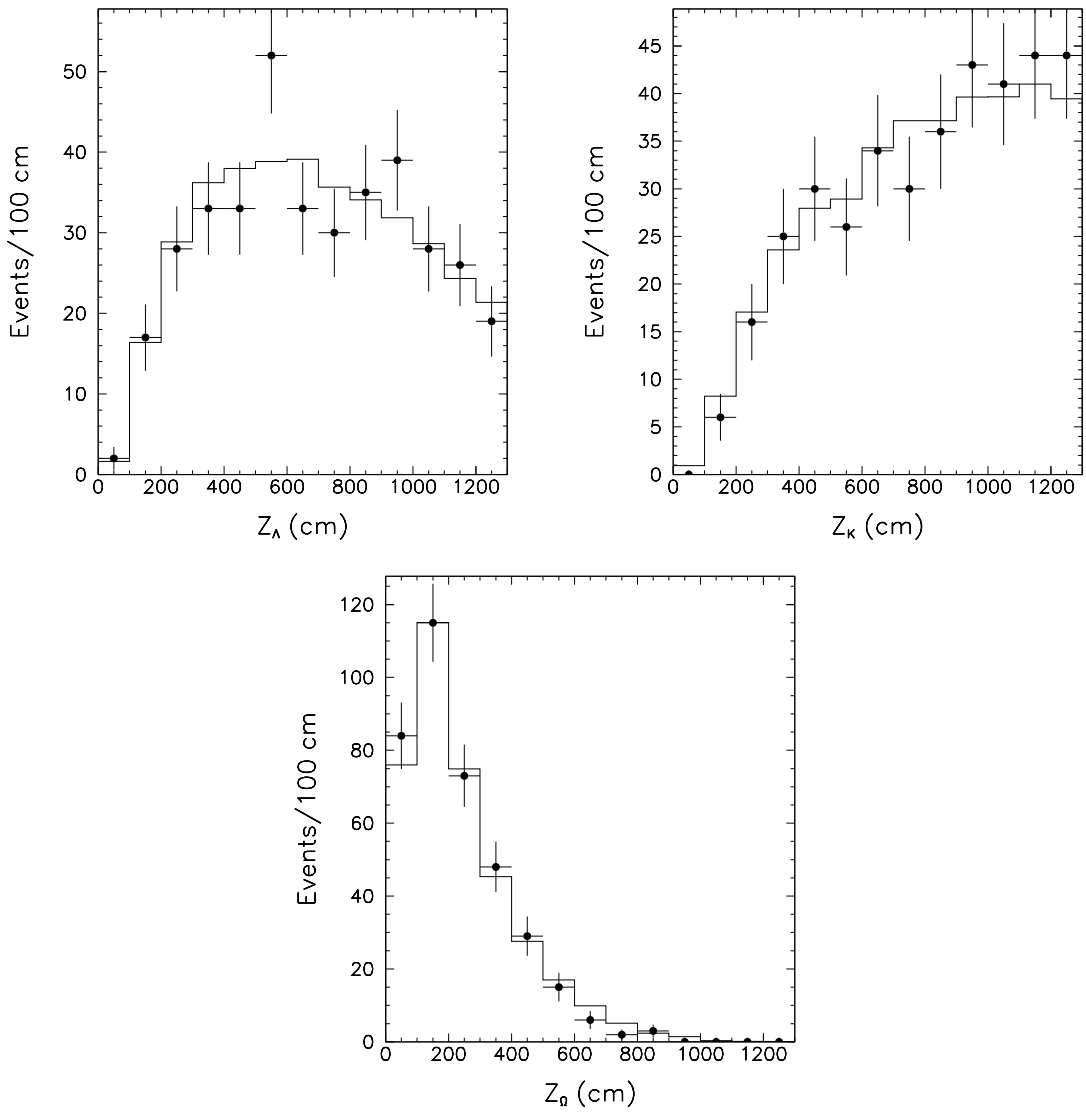

Figure 4.44. Data (Neg99) and MC comparison for the z position of the decay vertex after the cuts. Normalizing mode.

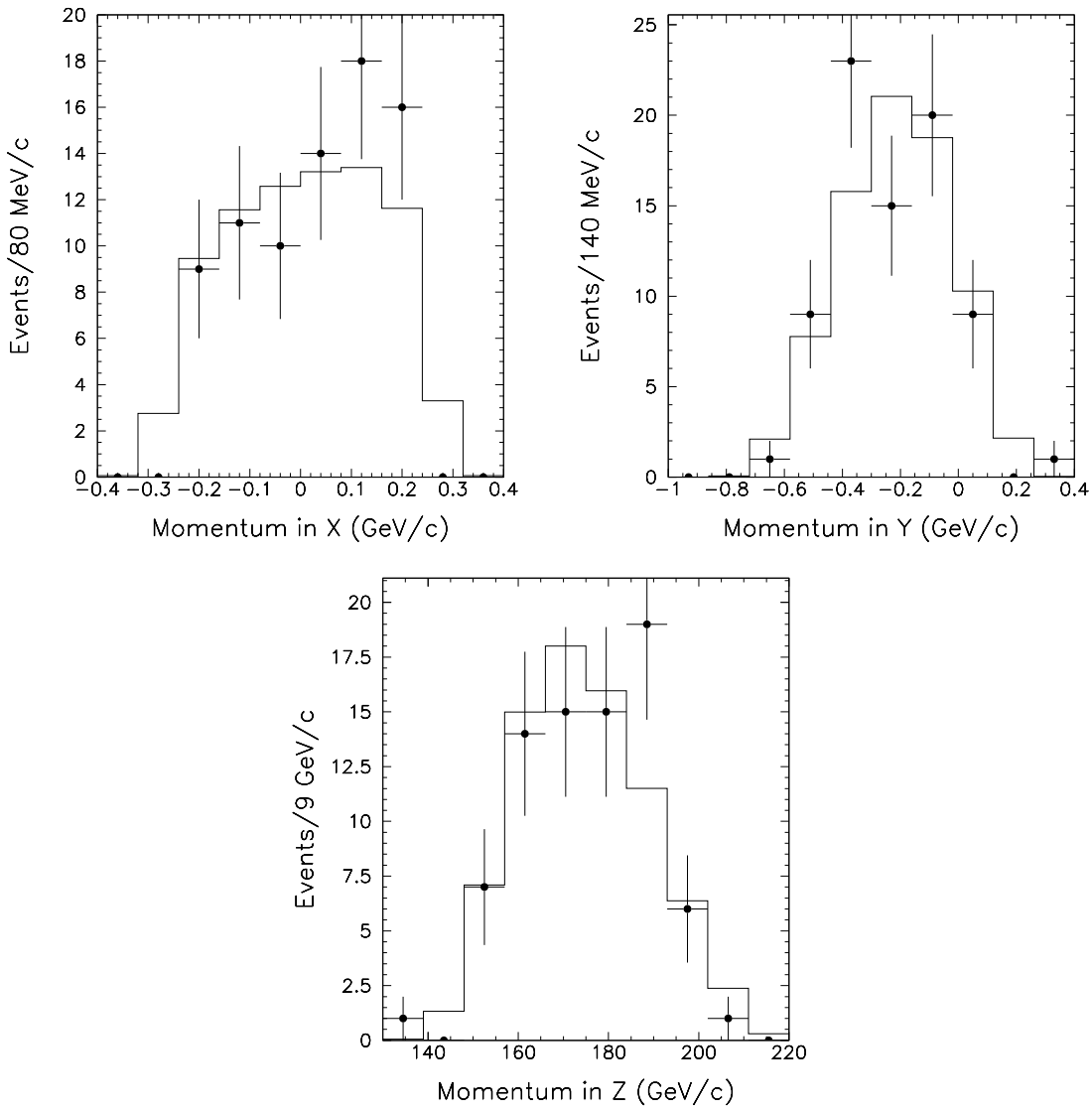

Figure 4.45. Data (Neg99) and MC comparison for x, y, and z projections of the Ω^- momentum after the cuts. Signal mode.

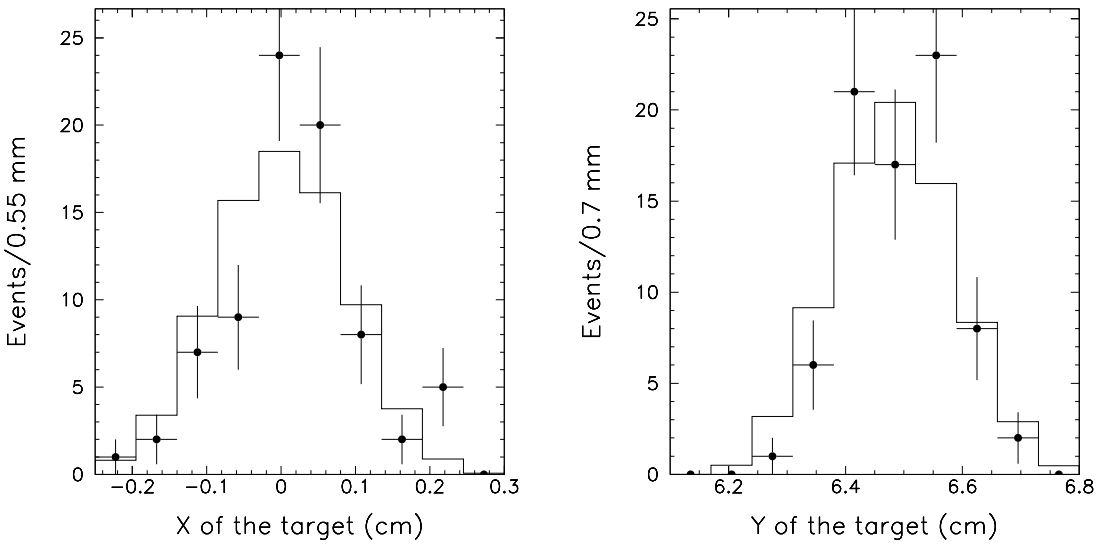

Figure 4.46. Data (Neg99) and MC comparison for x and y positions of the Ω^- at the target after the cuts. Signal mode.

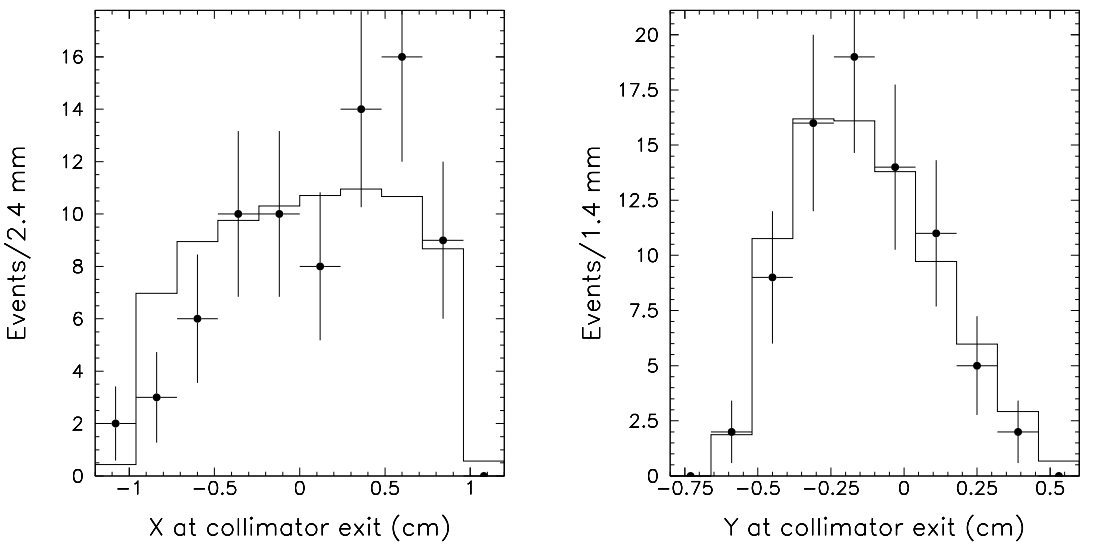

Figure 4.47. Data (Neg99) and MC comparison for x and y positions of the Ω^- at the collimator exit after the cuts. Signal mode.

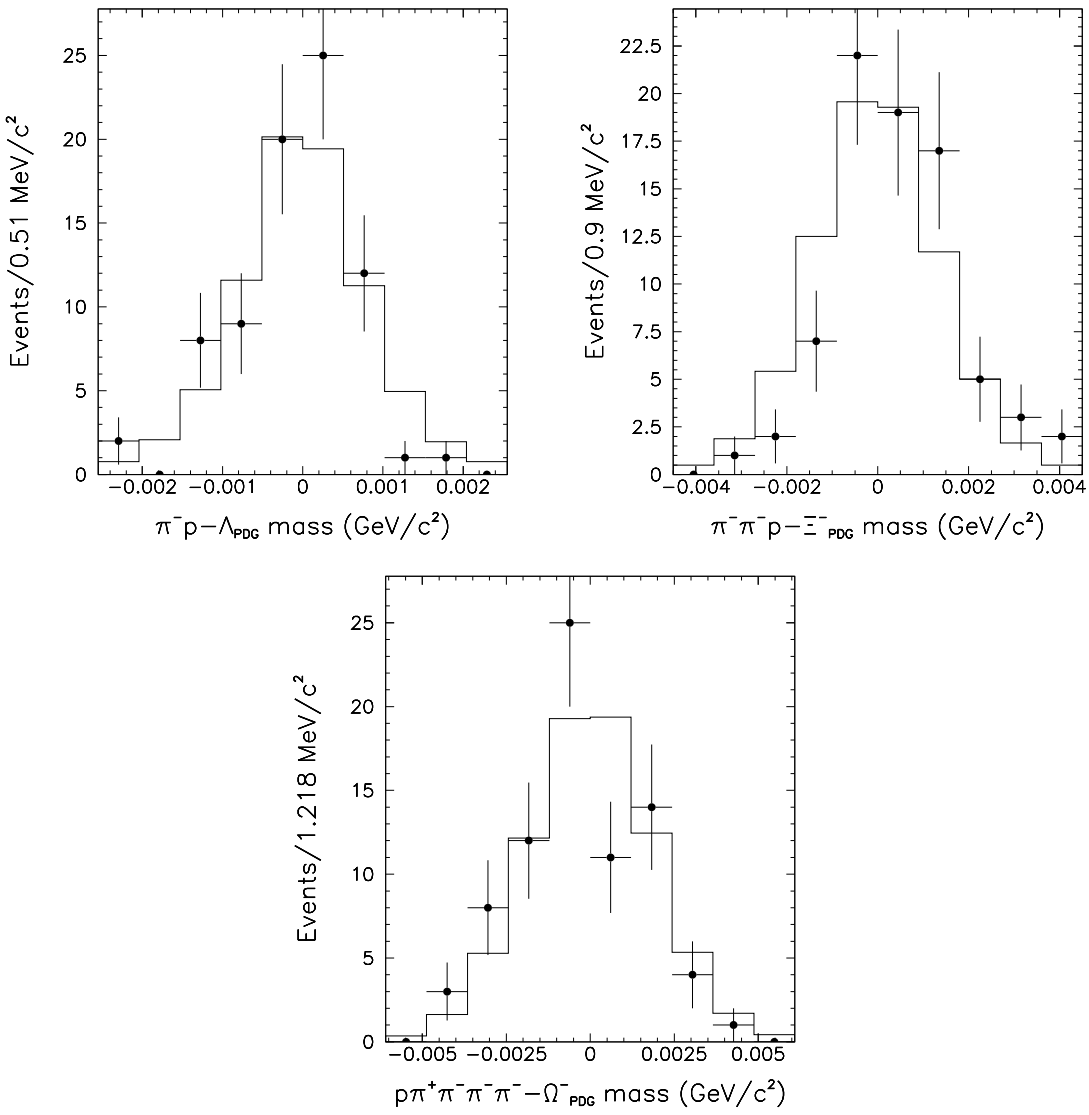

Figure 4.48. Data (Neg99) and MC comparison for the difference between reconstructed invariant mass after the cuts and PDG values. Signal mode.

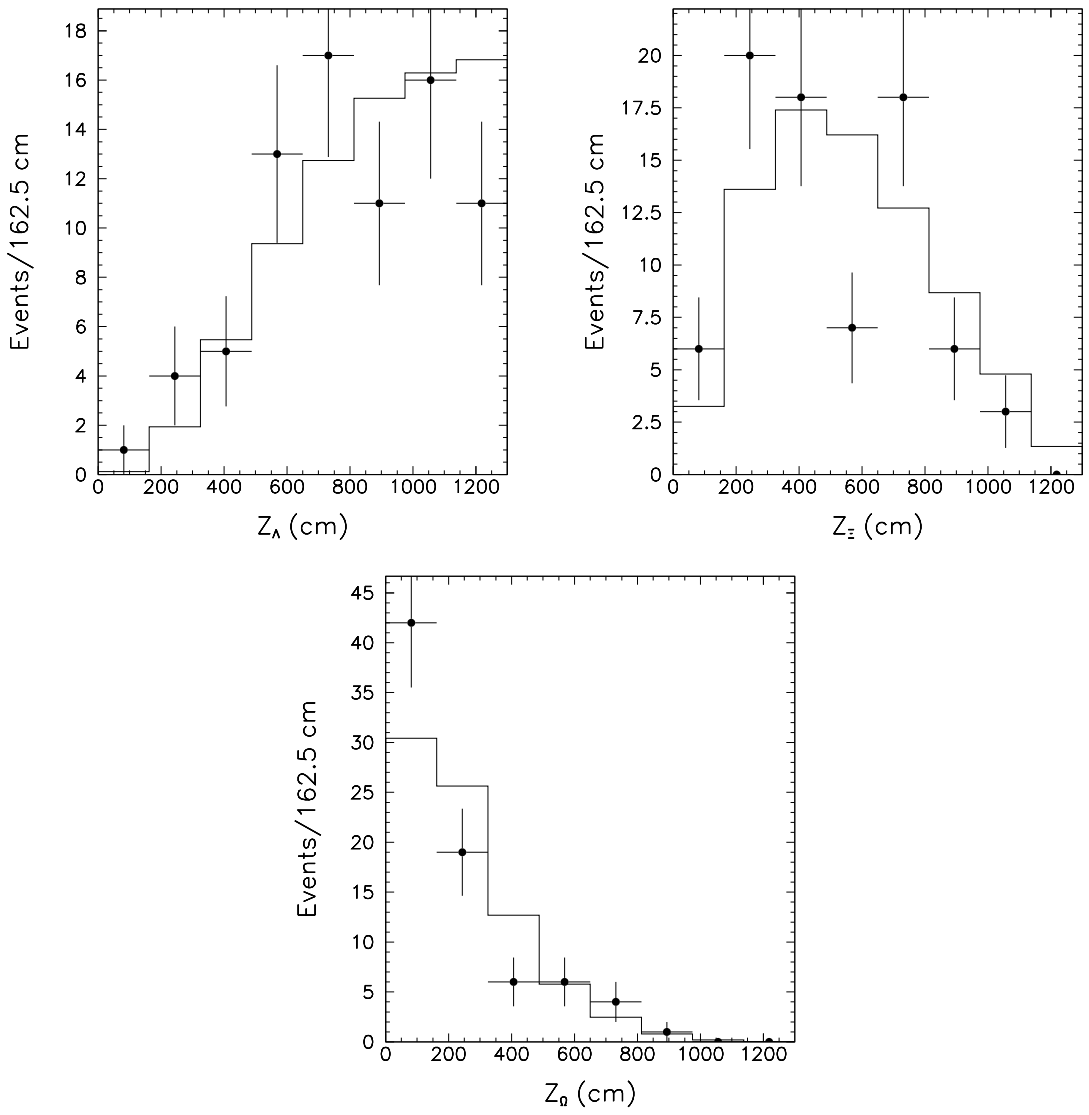

Figure 4.49. Data (Neg99) and MC comparison for the z position of the decay vertex after the cuts. Signal mode.

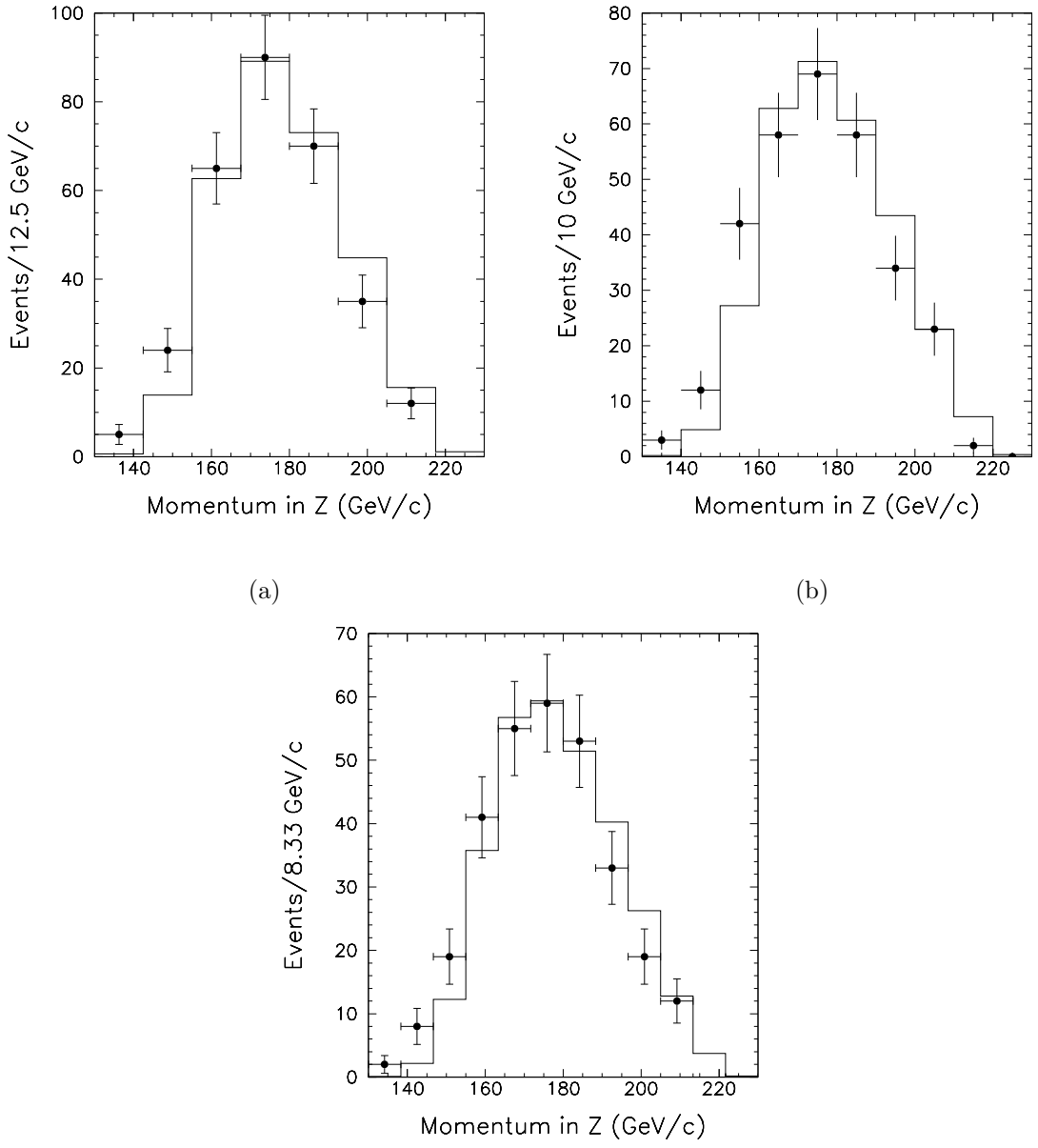

(a)

(b)

(c)

Figure 4.50. Data and MC comparison for the z projection of the Ω^- momentum. The same data are histogrammed with differing binning.

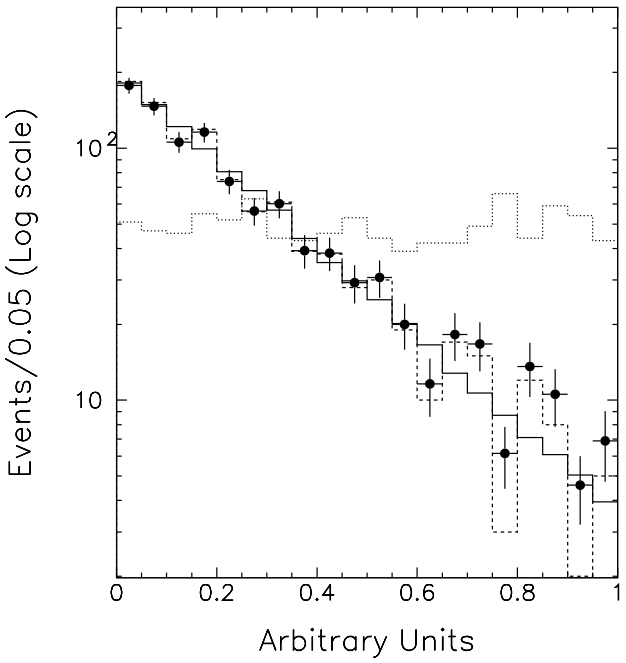

Figure 4.51. Distributions that were used to check the Kolmogorov test. Solid line is the exponential distribution with $5 \cdot 10^4$ entries; dashed line is the exponential distribution with 10^3 entries; dotted line is the uniform distribution with 10^3 entries; dots with error bars is the mixture of 95% exponential and 5% uniform with 10^3 entries. All histograms are normalized to the same number of entries.

CHAPTER 5

RESULTS

To calculate the branching ratios of interest we need to provide values for the variables on the right-hand side of equations (3.2) and (3.3). In particular we must calculate the number of events and acceptance for each decay mode. While the latter can be estimated with Monte Carlo simulations, to calculate the former is not a trivial task. In the first two sections of this chapter we explain how the number of events for each decay mode was calculated. We calculate both branching ratios in the third section.

5.1 Unbinned Generalized Log-Likelihood Fit Method

We would like to perform precise measurements, including parameter determination from fitting, but we have low statistics in both the normalizing and signal modes (see Table 5.1). Moreover, we want to do two-dimensional Dalitz-plot analysis with only 78 signal events! How should one proceed? First of all we must avoid data binning. In fitting a binned sample, we lose information. Moreover, binned fitting introduces biases due to empty bins and bin size. Second, we should use the likelihood fitting method since it is more reliable than the χ^2 method when there are doubts about the applicability of Gaussian statistics, particularly for low-statistics data sets. Finally, to make use of all available information, we would like to add the number of observed events as an additional constraint on the likelihood function. This also helps to avoid troubles with probability density function (pdf) renormalization. Thus, the unbinned generalized log-likelihood fit method is our choice.

Detailed description of the generalized likelihood method may be found elsewhere [11]. Here we describe it briefly. Suppose that we would like to fit some data with the fit function $f(x;\vec{p})$, where $\vec{p}$ is a vector of fit parameters. The fit function

must be properly normalized or else the likelihood method will not work. The integral over the fit range is

$$N(\vec{p}) = \int_{x_1}^{x_2} f(x;\vec{p})\, dx\,.$$

The likelihood is defined as

$$L(\vec{p}) = \prod_{i=1}^{n} \frac{f(x_i;\vec{p})}{N(\vec{p})}\,, \tag{5.1}$$

where n is the total number of observed events. The task of fitting is to find values for $\vec{p}$ that maximize L. Now we add the probability for observing n events, when the number of observed events is Poissonian with mean $N(\vec{p})$. Consequently, the equation for the generalized likelihood is

$$L(\vec{p}) = \frac{N^n(\vec{p})e^{N(\vec{p})}}{n!} \prod_{i=1}^{n} \frac{f(x_i;\vec{p})}{N(\vec{p})}\,. \tag{5.2}$$

The negative logarithm of the likelihood function is a computationally preferred quantity and is usually used. The likelihood L is maximal for the same values of $\vec{p}$ as when $-\ln L$ is at the minimum. Constant additive terms in $-\ln L$ do not affect the location of the minimum and can be safely removed. Thus, we need to minimize

$$-\ln L(\vec{p}) = N(\vec{p}) - \sum_{i=1}^{n} \ln f(x_i;\vec{p})\,. \tag{5.3}$$

Minimization of the quantity $-\ln L(\vec{p})$ can be done in a variety of ways. We chose to use the CERN function minimization program Minuit [15]. Several technical details about our use of Minuit are worth mentioning. We set the strategy for calculating first and second derivatives to the most precise (second) level and defined parameter errors as the change in parameter value required to change the $-\ln L$ function value by 0.5 since we used the likelihood fit method. We accepted fit results only when Minuit reported "status=converged" and "error matrix accurate."

5.1.1 Number of Ω decays calculation. To extract the numbers of normalizing- and signal-mode Ω decays, we fit the distribution of the reconstructed invariant mass

of the Ω with the Gaussian-plus-constant fit function. The unbinned generalized log-likelihood fit method was employed. The fit function is

$$f(m; n, \mu, \sigma, b) = \frac{n}{\sigma\sqrt{2\pi}} e^{-\frac{1}{2}\left(\frac{m-\mu}{\sigma}\right)^2} + \frac{b}{x_2 - x_1}\,, \tag{5.4}$$

where n is the number of Ω decays, b is the number of background events and the fit range is between x_1 and x_2. The function to minimize is thus

$$-\ln L(n, \mu, \sigma, b) = n + b - \sum_{i=1}^{n} f(m_i; n, \mu, \sigma, b)\,. \tag{5.5}$$

The reconstructed invariant Ω mass after all cuts except the Ω mass cut is plotted in Figures 5.1 through 5.4. Histograms are plotted for visualization purposes only: we do not fit them, we fit the unbinned data. The numbers of Ω decays and background events after the fit are listed in Table 5.1.

Figure 5.3 shows a large number of background events. Signal-mode candidate events for the Neg99 data subset have the largest ratio of background to Ω decays as can be inferred from Table 5.1. That there are many more background events on the right, higher-mass sideband than on the left suggests that the background is due to identifying some lower-mass particles as pions. The β-decay $\Omega^- \to \Xi^-\pi^+ l\bar{\nu}_l$ is a possible explanation.[3]

Independent of the origin of the background events in Figure 5.3, it is possible to reduce the background. The scatter plot of reconstructed[4] $\Xi^-\pi^+$ mass vs. Ω^- mass for the Neg99 data subset is shown in Figure 5.5. Events distributed along the diagonal show a correlation between the two masses. Furthermore, after all signal-mode cuts, the reconstructed invariant $\Xi^-\pi^+$ mass is less than 1.54 GeV/c^2. Thus, it is possible to remove some background events from Figure 5.3 by requiring that $m_{\Xi^-\pi^+} < 1.54$ GeV/c^2.

[3]Nick Solomey, HyperCP internal note.

[4]For brevity, we refer to the reconstructed $p(\overline{p})\pi^\pm\pi^\mp\pi^\mp$ mass as "$\Xi^\mp\pi^\pm$ mass."

We applied the Gaussian-plus-polynomial fit to the distribution (shown in Figure 5.6) of the reconstructed invariant Ω^- mass after the requirement that $m_{\Xi^-\pi^+} < 1.54$ GeV/c^2 and signal-mode cuts. We found 75.3 ± 8.9 decays of Ω^- (consistent with the corresponding value of 74.0 ± 8.9 from Table 5.1) and 21.7 ± 5.0 background events.

Table 5.1. Number of events in each of the data samples after the Gaussian-plus-polynomial fit.

	Normalizing Mode		Signal Mode	
Events	Neg99	Pos99	Neg99	Pos99
Ω decays	373.9 ± 19.4	155.4 ± 12.5	74.0 ± 8.9	22.7 ± 4.8
Background	7.1 ± 3.1	4.6 ± 2.3	32.0 ± 6.0	4.3 ± 2.1

5.2 Extraction of the Proportionality Coefficients

In Section 4.3 we plotted event variable distributions for both 3-body and resonance signal modes from the Monte Carlo simulations. The MC distributions for both signal modes have a large overlap region. As can be seen from Tables 4.12 and 4.13, the selection criteria efficiencies are also nearly the same for the 3-body and resonance modes. Thus, it is impossible to separate one signal mode from another just by applying a set of cuts to the data. More sophisticated methods must be used.

The numbers of resonance- and 3-body-mode decays are proportional to the total numbers of observed signal decays

$$N_{\Omega^-\to\Xi^{*0}_{1530}\pi^-} = p_{res} \cdot N_{signal}\,, \tag{5.6}$$

$$N_{\Omega^-\to\Xi^-\pi^+\pi^-} = p_{3b} \cdot N_{signal}\,, \tag{5.7}$$

and similarly for antiparticle modes. The proportionality coefficients (p_{res} and p_{3b}) can be found by fitting data to the combination of resonance and 3-body MCs. We can fit the distribution of $\Xi^\mp\pi^\pm$ invariant mass, which is the best variable for distinguishing between the resonance and 3-body modes. We can also perform the two-dimensional

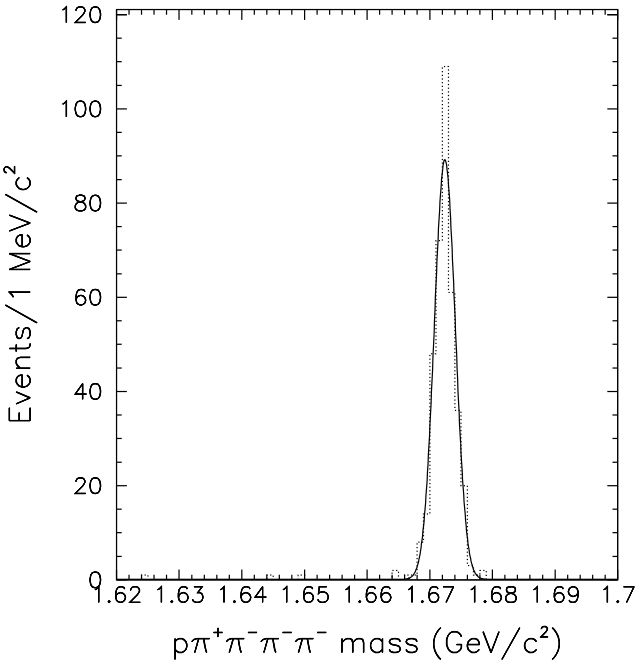

Figure 5.1. Reconstructed invariant Ω^- mass after all normalizing-mode cuts, except Ω^- mass cut.

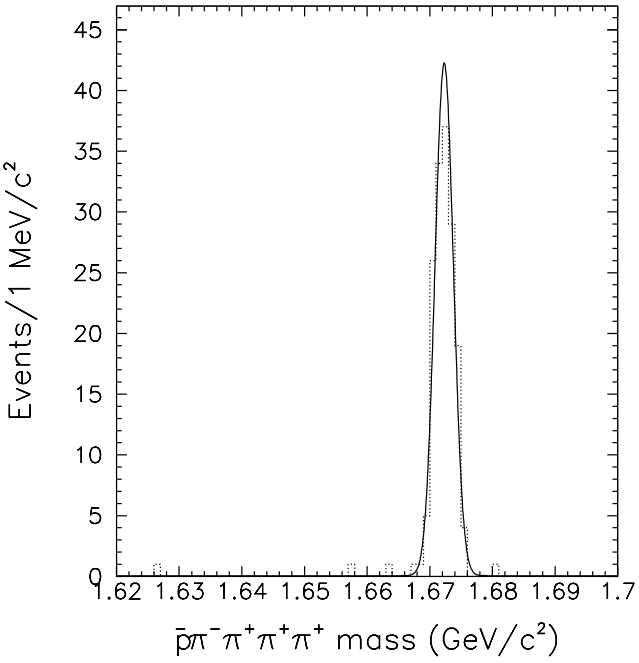

Figure 5.2. Reconstructed invariant Ω^+ mass after all normalizing-mode cuts, except Ω^+ mass cut.

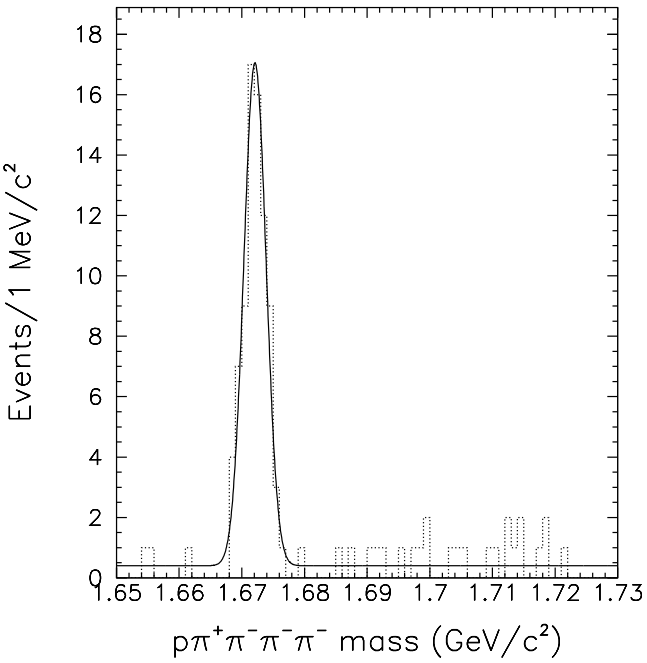

Figure 5.3. Reconstructed invariant Ω^- mass after all signal-mode cuts, except Ω^- mass cut.

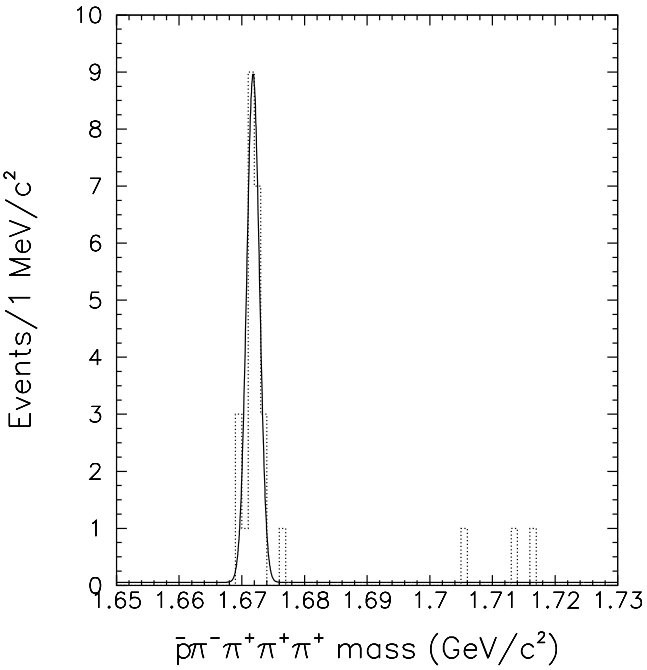

Figure 5.4. Reconstructed invariant Ω^+ mass after all signal-mode cuts, except Ω^+ mass cut.

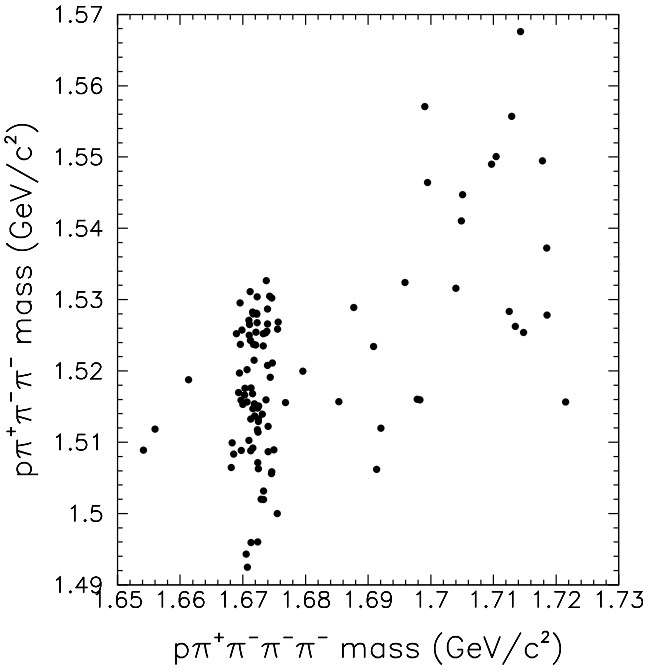

Figure 5.5. Reconstructed $\Xi^-\pi^+$ mass vs. Ω^- mass after all signal-mode cuts, except Ω^- mass cut.

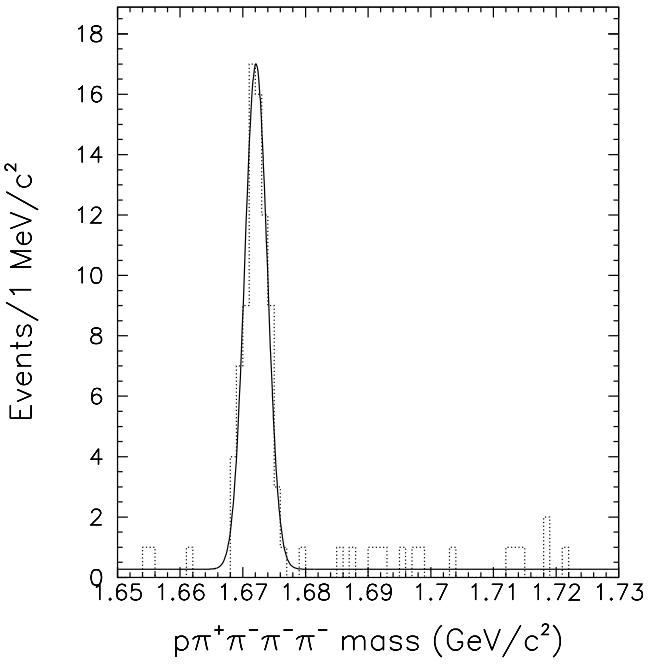

Figure 5.6. Reconstructed invariant Ω^- mass after the requirement that $m_{\Xi^-\pi^+} < 1.54$ GeV/c^2 and all signal-mode cuts, except Ω^- mass cut.

Dalitz-plot fit. Another sensitive variable is the angle between the opposite-sign pion momentum in the dipion rest frame and the dipion momentum in the parent Ω rest frame. We employ all three methods and show that they give consistent results.

5.2.1 $\Xi^{\mp}\pi^{\pm}$ invariant mass distribution fit. We apply the unbinned generalized log-likelihood fit method described in the preceding section. The fit function is

$$f(m_{\Xi^{\mp}\pi^{\pm}}; p_{res}, p_{3b}) = N_{signal}\left(p_{res}\frac{f_{res}(m_{\Xi^{\mp}\pi^{\pm}})}{N_{MC(res)}} + p_{3b}\frac{f_{3b}(m_{\Xi^{\mp}\pi^{\pm}})}{N_{MC(3b)}}\right), \tag{5.8}$$

where N_{signal} is the number of reconstructed signal Ω decays, $f_{res}(m_{\Xi^{\mp}\pi^{\pm}})$ and $f_{3b}(m_{\Xi^{\mp}\pi^{\pm}})$ are functional forms of the corresponding MCs, and $N_{MC(res)}$ and $N_{MC(3b)}$ are the total numbers of events in the MCs. The function to minimize is thus

$$-\ln L(p_{res}, p_{3b}) = N_{signal}(p_{res} + p_{3b}) - \sum_{i=1}^{N_{signal}} f(m_i; p_{res}, p_{3b})\,. \tag{5.9}$$

The functions f_{res} and f_{3b} can be found by smoothing the histograms of $\Xi^{\mp}\pi^{\pm}$ invariant mass for the resonance- and 3-body-mode MCs correspondingly. They are shown in Figures 5.7 and 5.8.

The quantity $-\ln L(p_{res}, p_{3b})$ was minimized in Minuit. The proportionality coefficients after the fit for the Neg99 (Pos99) data subset are given in Table 5.2 (5.3). The fit function (5.8) after the Minuit fit is plotted in Figure 5.9 (5.10) for the particle (antiparticle) mode. The resonance-mode and 3-body-mode MC histograms together with the data are also shown (please note that histograms are plotted for visualization purposes only and are not used in the fit procedure).

To make sure that Minuit returned meaningful result, we examined the log-likelihood function in Minuit. We conclude by examining the $-\ln L$ contour that there is a well-defined minimum and that the fit parameters are negatively correlated with each other. We plotted $-\ln L$ as a function of p_{res} with p_{3b} fixed at the value corresponding to the $-\ln L$ minimum. Our conclusion is that Minuit has found a

well-defined local minimum which is stable against small perturbations. The Minuit output is given in Appendix E (F) for the Neg99 (Pos99) data subset.

Table 5.2. Two-parameter unbinned log-likelihood fit results using Negative99 data.

Parameter	Ξ^{*0}_{1530} mass fit	Dalitz plot fit	$\cos\psi$ fit
p_{3b}	0.851 ± 0.128	0.828 ± 0.125	0.898 ± 0.145
p_{res}	0.149 ± 0.086	0.172 ± 0.085	0.102 ± 0.104

Table 5.3. Two-parameter unbinned log-likelihood fit results using Positive99 data.

Parameter	$\overline{\Xi^{*0}_{1530}}$ mass fit	Dalitz plot fit	$\cos\psi$ fit
p_{3b}	0.973 ± 0.245	0.927 ± 0.238	0.737 ± 0.261
p_{res}	0.027 ± 0.144	0.073 ± 0.146	0.263 ± 0.220

5.2.2 Dalitz plot fit. The Dalitz plot of reconstructed $\Xi^{\mp}\pi^{\pm}$ mass vs. $\pi^{\pm}\pi^{\mp}$ mass for the Neg99 (Pos99) data subset is shown as the large dots in Figures 5.11 (5.13) and 5.12 (5.14). They can be compared with the distribution of resonance-channel MC events in Figure 5.11 (5.13) and that of uniform-phase-space 3-body MC events in Figure 5.12 (5.14). Qualitatively our data are more consistent with the 3-body decay than with the resonance mode.

The fit function $f(m_{\Xi^{\mp}\pi^{\pm}}, m_{\pi^{\pm}\pi^{\mp}}; p_{res}, p_{3b})$ is an extension of equation (5.8) to the two-dimensional case. The functions f_{res} and f_{3b} were found by smoothing the two-dimensional Monte Carlo Dalitz plot histograms. As an example, the histogram and the corresponding analytical function for the resonance-mode MC are shown in Figure 5.15. The proportionality coefficients after the fit for the Neg99 (Pos99) data subset are given in Table 5.2 (5.3). They are consistent with the results of the preceding method.

We examined the log-likelihood function behavior in Minuit and did not see any indications of problems. Again, we concluded that Minuit found a well-defined

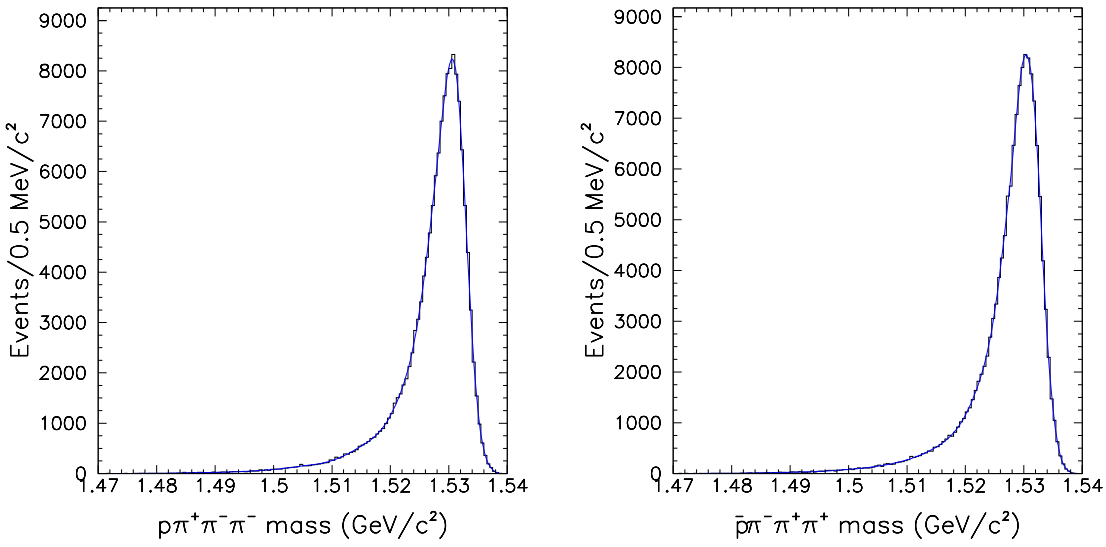

Figure 5.7. Reconstructed invariant mass of $\Xi^{\mp}\pi^{\pm}$ after all cuts for the resonance-mode MC. Solid line is the analytical function (f_{res}) found by smoothing.

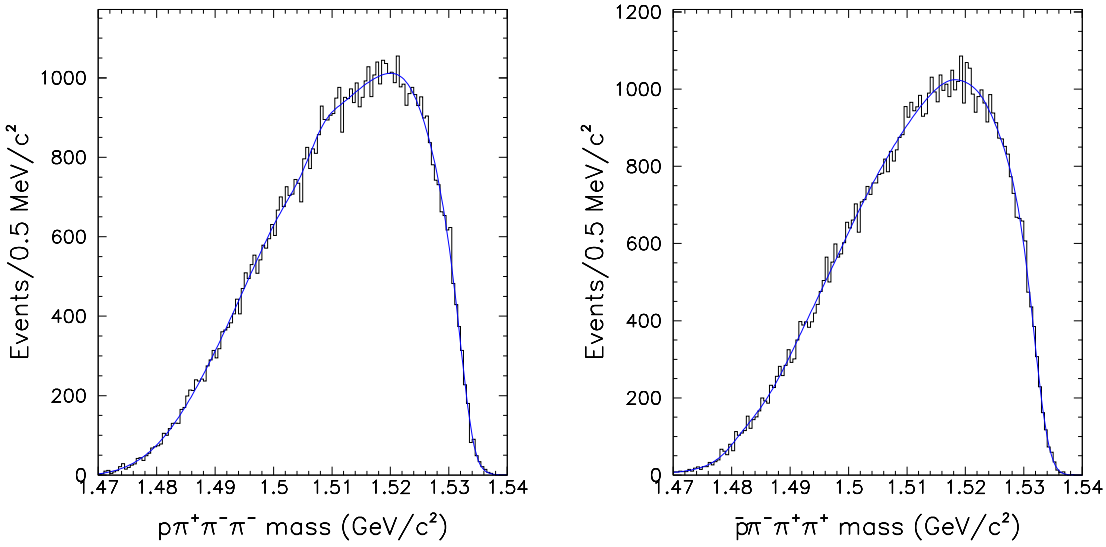

Figure 5.8. Reconstructed invariant mass of $\Xi^{\mp}\pi^{\pm}$ after all cuts for the 3-body-mode MC. Solid line is the analytical function (f_{3b}) found by smoothing.

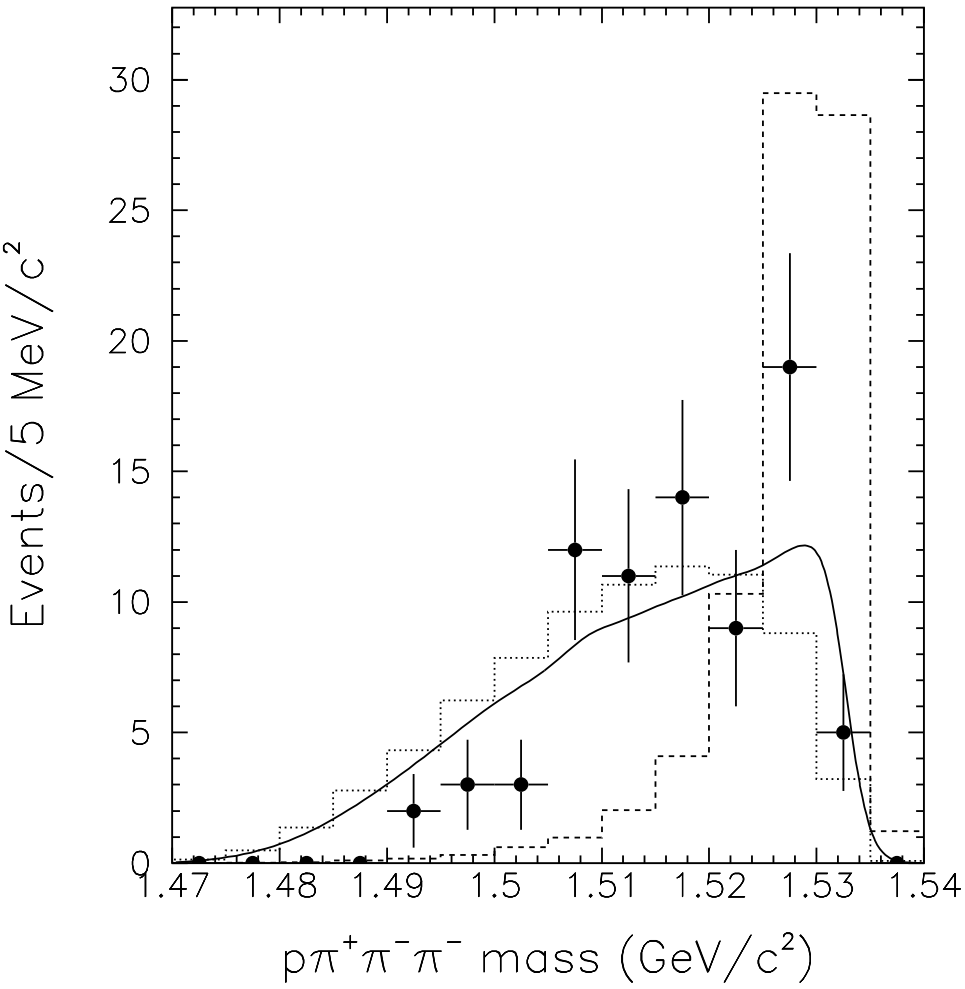

Figure 5.9. Reconstructed invariant $\Xi^-\pi^+$ mass for the Neg99 data subset (dots with error bars) together with the resonance (dashed line) and 3-body (dotted line) mode MCs. Solid line is the fit function with the proportionality coefficients after Minuit minimization.

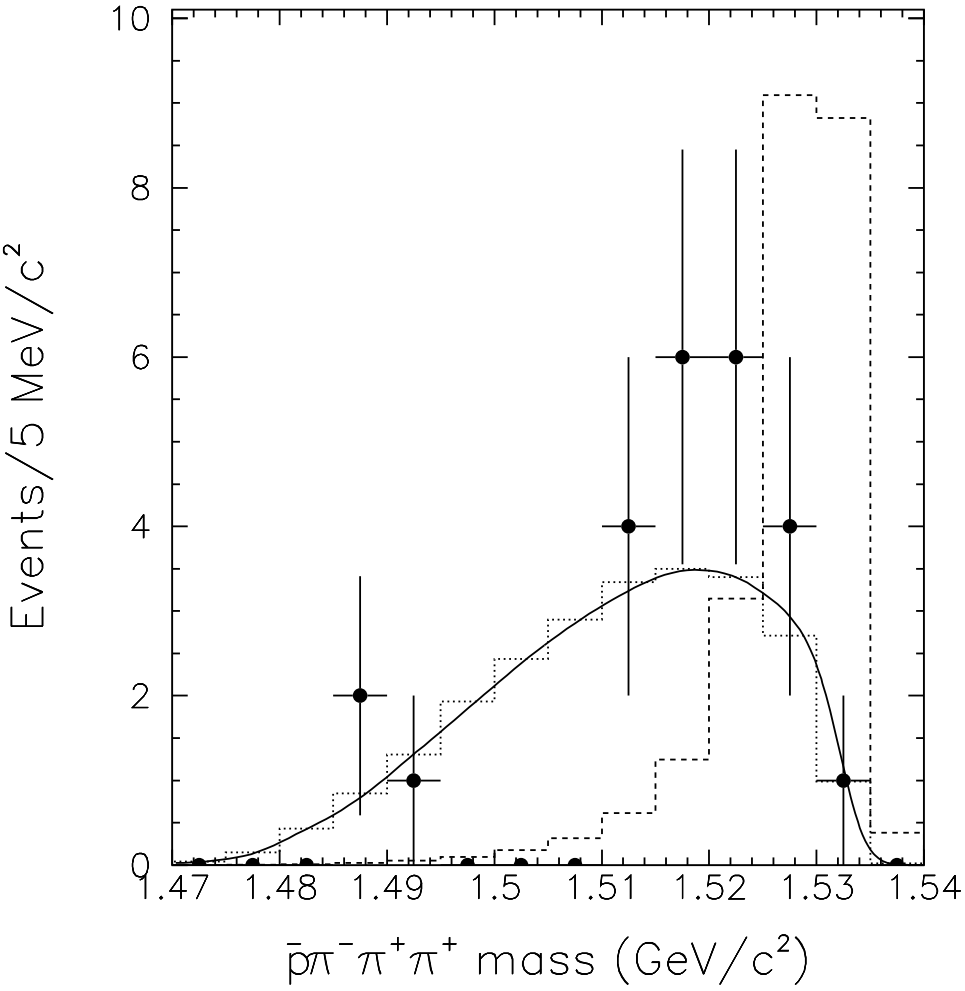

Figure 5.10. Reconstructed invariant $\Xi^+\pi^-$ mass for the Pos99 data subset (dots with error bars) together with the resonance (dashed line) and 3-body (dotted line) mode MCs. Solid line is the fit function with the proportionality coefficients after Minuit minimization.

local minimum. The Minuit output is given in Appendix E (F) for the Neg99 (Pos99) data subset.

5.2.3 $\cos\psi$ **distribution fit.** The same procedure as was used to fit the reconstructed $\Xi^{\mp}\pi^{\pm}$ mass can be applied to the $\cos\psi$ distribution. We only change $m_{\Xi^{\mp}\pi^{\pm}}$ to $\cos\psi$ in the fit function (5.8). The analytical functions after smoothing are plotted in Figures 5.16 and 5.17.

The proportionality coefficients after the fit for the Neg99 (Pos99) data subset are given in Table 5.2 (5.3). They are consistent with both preceding results. The fit function after the Minuit fit is plotted in Figure 5.18 (5.19) for the particle (antiparticle) mode. The resonance-mode and 3-body-mode MC histograms together with the data are also shown (again, please note that histograms are plotted for visualization purposes only and are not used in the fit procedure). The fit function behavior in Minuit indicates that a well-defined local minimum was found. The Minuit output is given in Appendix E (F) for the Neg99 (Pos99) data subset.

5.2.4 Compatibility between data and MC. We employed χ^2 and Kolmogorov tests to estimate the compatibility between data and MC distributions for the variables that distinguish the resonance mode from the 3-body mode. Due to the small numbers of reconstructed signal events, only univariate distributions were used. Data were compared with the pure 3-body mode MC (f_{3b}), the pure resonance mode MC (f_{res}), and with their combination with the found proportionality coefficients ($p_{3b}f_{3b} + p_{res}f_{res}$). Probabilities of compatibility for Neg99 (Pos99) data are given in Table 5.4 (5.5). As discussed in Section 4.4.1, the χ^2 test is unreliable for the small data subsets and the Kolmogorov test gives the more accurate result. Calculated Kolmogorov test probabilities confirm that the proportionality coefficients, found after the unbinned generalized log-likelihood fit, give a reasonable match between data and MC.

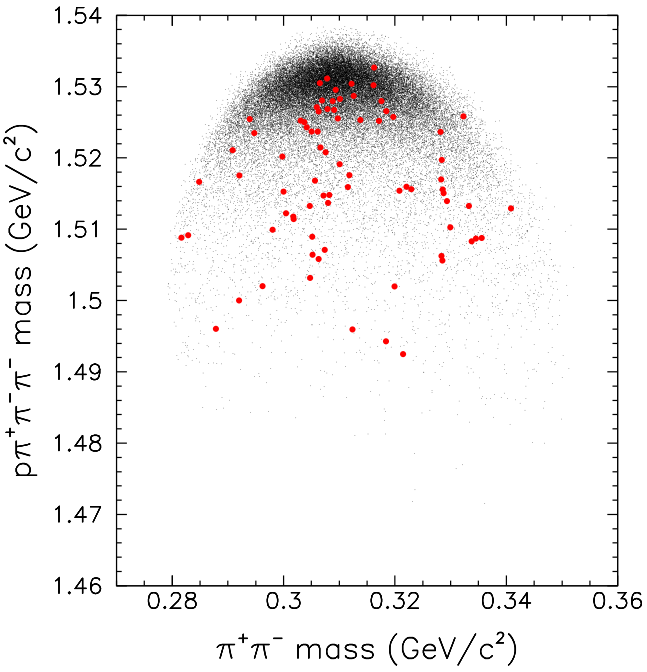

Figure 5.11. Reconstructed $\Xi^-\pi^+$ mass vs. $\pi^+\pi^-$ mass for the resonance-channel MC. The large dots represent the data.

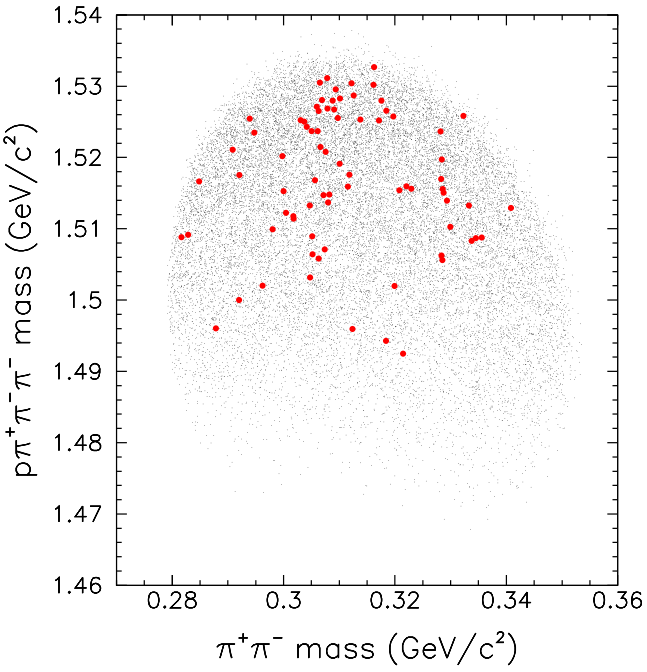

Figure 5.12. Reconstructed $\Xi^-\pi^+$ mass vs. $\pi^+\pi^-$ mass for the 3-body MC. The large dots represent the data.

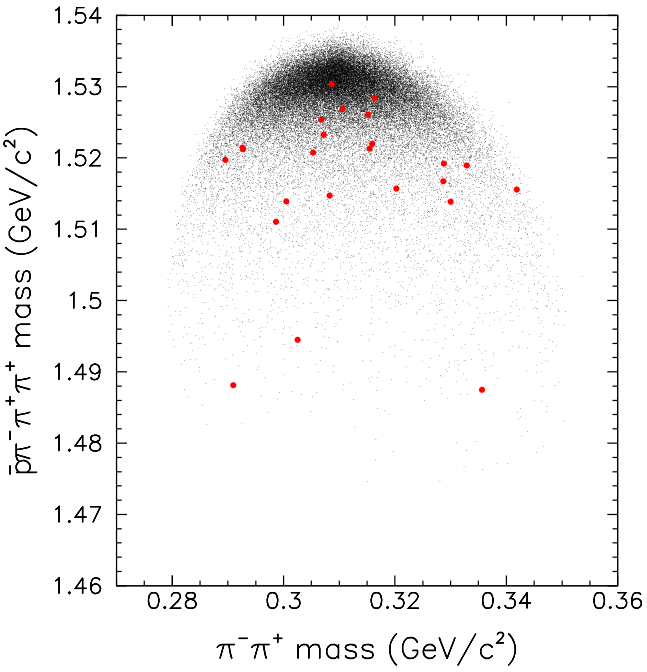

Figure 5.13. Reconstructed $\Xi^+\pi^-$ mass vs. $\pi^-\pi^+$ mass for the resonance-channel MC. The large dots represent the data.

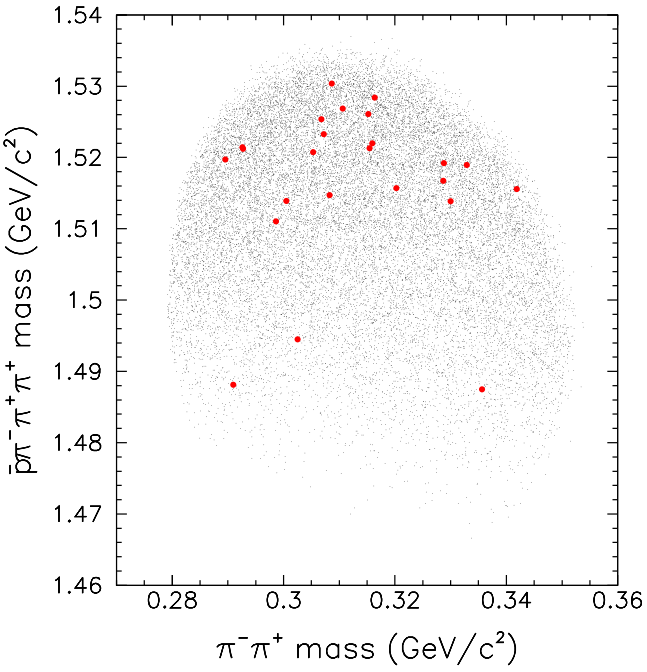

Figure 5.14. Reconstructed $\Xi^+\pi^-$ mass vs. $\pi^-\pi^+$ mass for the 3-body MC. The large dots represent the data.

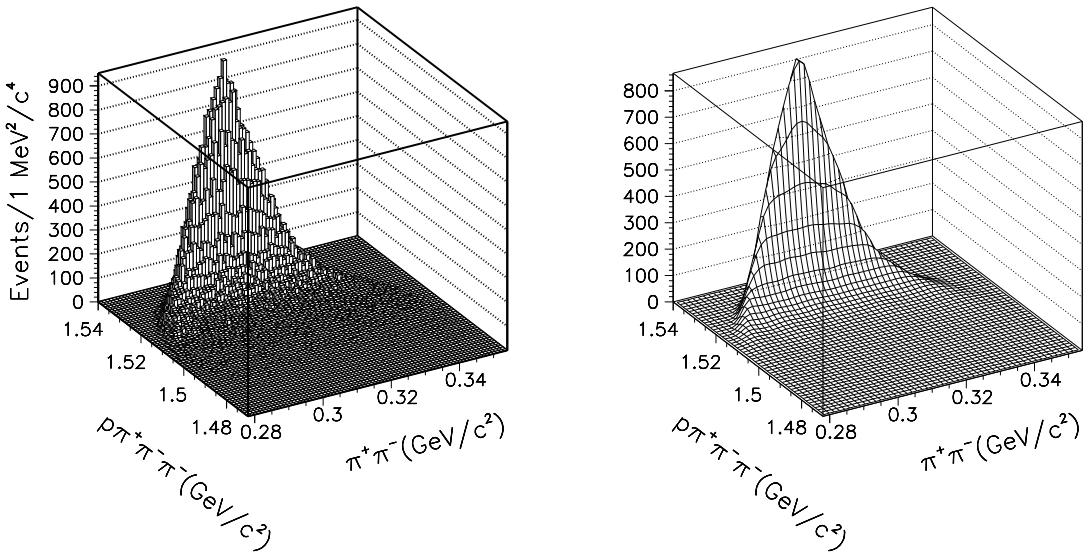

Figure 5.15. Reconstructed $\Xi^-\pi^+$ mass vs. $\pi^+\pi^-$ mass for the resonance-channel MC. Histogrammed MC (left plot) can be compared with the analytical function (f_{res}) (right plot) found by smoothing.

5.3 Calculation of the Branching Ratios

Now we have all necessary ingredients for the branching ratio calculation. Acceptances for each mode are given in Table 5.6. Other decay mode branching ratios that we need for the calculation are taken from the PDG review [32] as follows:

$$B(\Omega^{\mp} \to \Lambda(\overline{\Lambda})K^{\mp}) = 6.78 \times 10^{-1},$$

$$B(K^{\mp} \to \pi^{\mp}\pi^{\pm}\pi^{\mp}) = 5.59 \times 10^{-2},$$

Table 5.4. Compatibility between Negative99 data and MC.

			Probability, %	
MC function	Fit variable	χ^2/dof	χ^2 test	Kolmogorov test
f_{3b}	Ξ^{*0}_{1530} mass	18.49/8	1.78	0.21
f_{res}	Ξ^{*0}_{1530} mass	51.73/8	0.00	0.00
$p_{3b}f_{3b} + p_{res}f_{res}$	Ξ^{*0}_{1530} mass	13.78/8	8.77	15.66
f_{3b}	$\cos\psi$	14.49/6	2.46	2.01
f_{res}	$\cos\psi$	45.11/6	0.00	0.00
$p_{3b}f_{3b} + p_{res}f_{res}$	$\cos\psi$	12.13/6	5.91	23.69

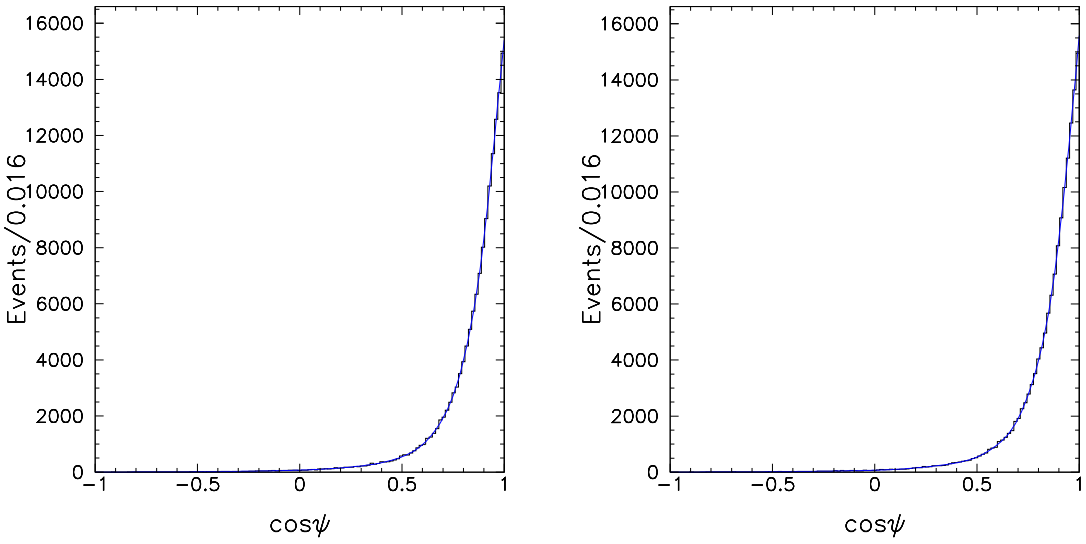

Figure 5.16. Distribution of $\cos\psi$ for particles (left plot) and antiparticles (right plot) after all cuts for the resonance-mode MC. Solid line is the analytical function found by smoothing.

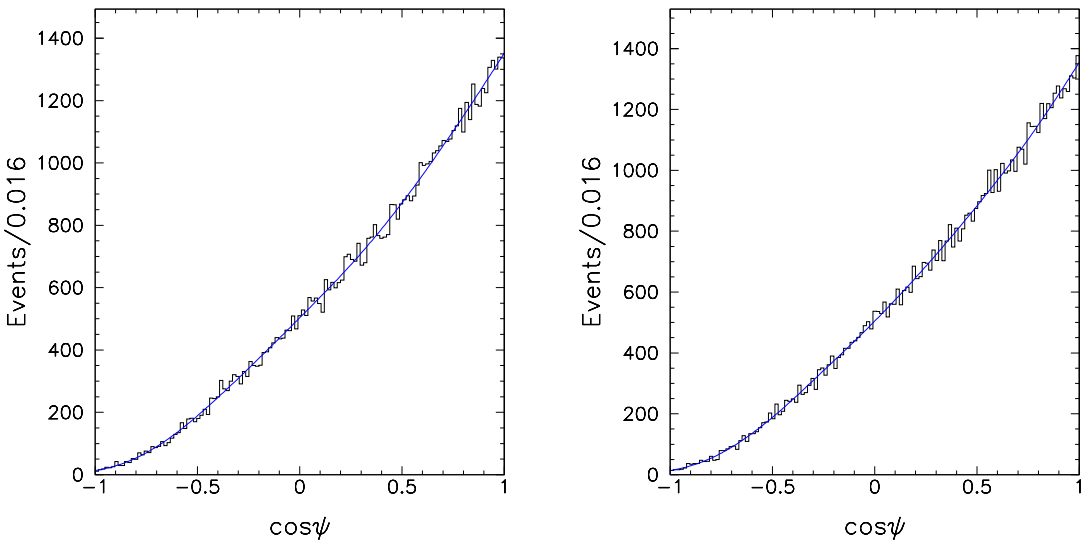

Figure 5.17. Distribution of $\cos\psi$ for particles (left plot) and antiparticles (right plot) after all cuts for the 3-body-mode MC. Solid line is the analytical function found by smoothing.

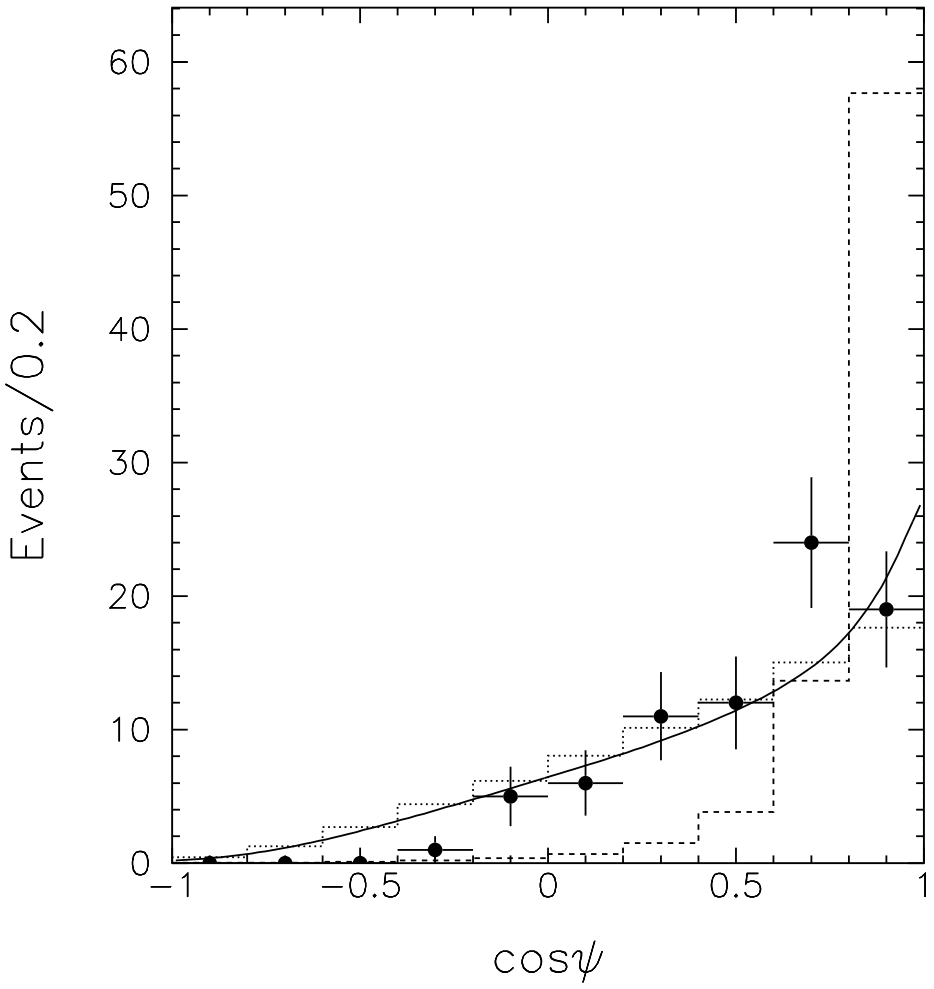

Figure 5.18. Distribution of $\cos\psi$ for the Neg99 data subset (dots with error bars) together with the resonance- (dashed line) and 3-body- (dotted line) mode MCs. Solid line is the fit function with the proportionality coefficients after Minuit minimization.

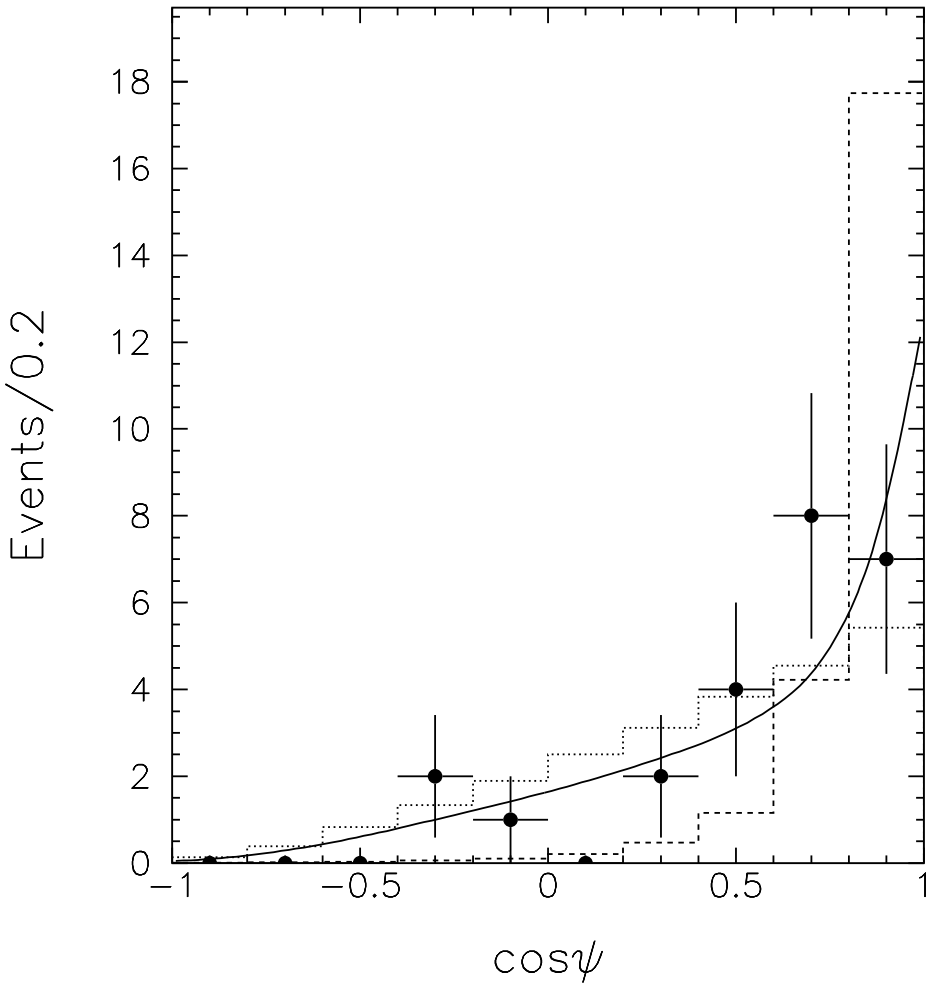

Figure 5.19. Distribution of $\cos\psi$ for the Pos99 data subset (dots with error bars) together with the resonance- (dashed line) and 3-body- (dotted line) mode MCs. Solid line is the fit function with the proportionality coefficients after Minuit minimization.

Table 5.5. Compatibility between Positive99 data and MC.

			Probability, %	
MC function	Fit variable	χ^2/dof	χ^2 test	Kolmogorov test
f_{3b}	$\overline{\Xi^{*0}_{1530}}$ mass	1.74/6	94.21	0.43
f_{res}	$\overline{\Xi^{*0}_{1530}}$ mass	18.73/6	0.46	0.00
$p_{3b}f_{3b} + p_{res}f_{res}$	$\overline{\Xi^{*0}_{1530}}$ mass	2.43/6	87.59	1.04
f_{3b}	$\cos\psi$	3.49/5	62.55	2.33
f_{res}	$\cos\psi$	12.16/5	3.27	0.00
$p_{3b}f_{3b} + p_{res}f_{res}$	$\cos\psi$	4.58/5	46.96	18.22

$$B(\Xi^{*0}_{1530}(\overline{\Xi^{*0}_{1530}}) \to \Xi^{\mp}\pi^{\pm}) = 2/3$$

$$B(\Xi^{\mp} \to \Lambda(\overline{\Lambda})\pi^{\mp}) = 9.99 \times 10^{-1}\,.$$

Using these values together with the proportionality-coefficient values from Tables 5.2 and 5.3 and the numbers of events from Table 5.1 in equations (3.2), (3.3), (5.6), and (5.7), we obtain the particle (antiparticle) mode branching ratios summarized in Table 5.7 (5.8). As expected, all these methods give consistent results. The errors in both tables are statistical only. They arise from the number of events and fitting-parameter uncertainties.

The branching ratio for the particle 3-body-decay mode is in agreement with the previous experimental result [3] listed in the PDG review. We have performed the first measurement for the antiparticle 3-body-decay mode and have found that its branching ratio is in agreement with that for the particle mode.

The resonance-mode branching ratios disagree with the current PDG value, being ≈ 14 times smaller. The particle and antiparticle results are consistent with each other. Since the branching ratio central value is less than 2σ from zero, we also calculate branching ratio upper limits at 90% confidence level following the method described in [22] on page 79. The results are given in Table 5.9.

Table 5.6. Mode acceptances.

Decay	Neg99 subset	Pos99 subset
$\Omega \to \Xi^{*0}_{1530}\pi$	1.20×10^{-2}	1.20×10^{-2}
$\Omega \to \Xi\pi\pi$	4.88×10^{-3}	4.92×10^{-3}
$\Omega \to \Lambda K$	2.81×10^{-4}	2.78×10^{-4}

Table 5.7. Calculated branching ratios in units of 10^{-5} for the particle-mode decays (errors are statistical only.)

Decay	Ξ^{*0}_{1530} mass fit	Dalitz plot fit	$\cos\psi$ fit
$\Omega^- \to \Xi^{*0}_{1530}\pi^-$	3.94 ± 2.33	4.55 ± 2.33	2.68 ± 2.77
$\Omega^- \to \Xi^-\pi^+\pi^-$	36.75 ± 7.32	35.76 ± 7.14	38.81 ± 8.06

Table 5.8. Calculated branching ratios in units of 10^{-5} for the antiparticle-mode decays (errors are statistical only.)

Decay	Ξ^{*0}_{1530} mass fit	Dalitz plot fit	$\cos\psi$ fit
$\Omega^+ \to \overline{\Xi^{*0}_{1530}}\pi^+$	0.53 ± 2.80	1.40 ± 2.83	5.09 ± 4.41
$\Omega^+ \to \Xi^+\pi^-\pi^+$	30.49 ± 10.33	29.07 ± 9.95	23.08 ± 9.70

Table 5.9. Calculated resonance-mode branching ratio upper limit in in units of 10^{-5} at 90% confidence level taking only statistical errors into account.

Decay	Ξ^{*0}_{1530} mass fit	Dalitz plot fit	$\cos\psi$ fit
$\Omega^- \to \Xi^{*0}_{1530}\pi^-$	6.99	7.57	6.51
$\Omega^+ \to \overline{\Xi^{*0}_{1530}}\pi^+$	4.93	5.61	11.05

CHAPTER 6

SYSTEMATIC ERRORS

Parameters can be measured only with some finite precision. Parameter uncertainties impact our branching ratio calculations and must be taken into account. Moreover, running conditions varied during the data taking period and our results must be corrected for this. Such errors, incorporated into the final branching ratios, are called systematics.

Systematic errors for the parameters that are used explicitly in the branching ratio equations (3.2) and (3.3) can be calculated straightforwardly. These include, for example, the subsequent decay branching ratio $B(\Xi^{\mp} \rightarrow \Lambda(\overline{\Lambda})\pi^{\mp})$. Due to the complexity of the experimental setup, for another large fraction of parameters it is impossible to know exactly how their variations affect the final result. To estimate the associated systematic errors we employ Monte Carlo simulation.

For any parameter contributing to the final answer, we first determine the variation range, which for some variables is equal to one standard deviation (σ) away from the central value. Then we change the parameter value by σ and, when necessary, run MC simulations for the normalizing and signal modes. Finally, a new branching ratio (B_{var}) is calculated and the associated systematic error is estimated as

$$\frac{\delta B}{B} = \frac{B_{var} - B_{centr}}{B_{centr}}\,, \tag{6.1}$$

where B_{centr} is the branching ratio central value calculated in the preceding chapter. We add individual errors in quadrature to get the total systematic error.

To estimate the variation in the target center position, we fit the Ω distribution at the target with a Gaussian for the normalizing mode data and found the standard deviation. Then we changed the location of the target center by σ and ran MC simulations for the resonance, 3-body, and normalizing modes.

We arbitrarily varied the Ω momentum spectrum at the target. To generate the momentum component along the z axis, a uniform distribution was used instead of the probability density function plotted in Figure 4.2. As a separate systematic error, momentum components in the x and y directions were generated within an extended range, from -5 to 5 GeV/c.

The magnetic field in the Hyperon Magnet was varied by $\pm 0.1\%$ from the MC default value to estimate the systematic error. We reconstructed the new MC files with the default ("old") magnetic field. The same procedure was applied for the Analyzing Magnet magnetic fields.

We varied the Ω, Ξ, and Λ asymmetry parameters within ranges stated in the PDG book and ran MC simulations to study the associated systematic errors. We did not vary the kaon decay form factors primarily because of the limited time available. However, the linear term form factor is known with $\approx 1\%$ precision and the systematic error from the kaon form factor uncertainties is expected to be small.

Lifetimes for Ω, Ξ, Λ, and K were varied according to the PDG book uncertainties. MC simulation was employed to calculate each systematic error.

MC statistics is another source of systematic error, which was estimated as $\sqrt{N}/N$, where N is the number of MC events.

Systematic errors are listed in Table 6.1 (6.2) for particle (antiparticle) decay modes. The largest contribution is from the Ω momentum spectrum variation. The second largest error is from the target position uncertainties.

To calculate branching ratio upper limits one needs to combine statistical and systematic errors. Here we assumed that both errors are normally distributed and added them in quadrature. As can be seen from Tables 6.1 and 6.2, the total systematic errors are assymetric. For branching ratio calculations we assume them to

be symmetric and use the error with the largest absolute value. Since the statistical uncertainty dominates over systematics, the branching ratio upper limit depends weakly on the systematic error value.

There is an alternative approach for an upper limit calculation taking into account statistical and systematic errors. It is based on a Monte Carlo simulation that generates proportionality coefficient values according to the actual probability density functions from the Minuit fit. Other quantities are treated as Gaussian-distributed. The upper limit can then be calculated from the distribution of the calculated branching ratio. This method was used, for example, in [26, 25].

Table 6.1. Systematic errors for particle signal modes.

Source	Variation	$\frac{\delta B_{3b}}{B_{3b}}$ (%)	$\frac{\delta B_{res}}{B_{res}}$ (%)
Target x center	+0.69 mm	0.38	−1.87
	−0.69 mm	−0.70	1.50
Target y center	+0.93 mm	−0.99	−3.00
	−0.93 mm	−3.31	−1.22
Momentum Spectrum, p_z	uniform	3.49	6.53
Momentum Spectrum, p_x, p_y	broader	1.45	1.87
Hyperon Magnet, B-field	+0.1 %	−0.82	−1.13
	−0.1 %	−0.56	−0.10
Analyzing Magnets, B-field	+0.1 %	1.48	1.45
	−0.1 %	−0.83	−0.49
α_Ω for $\Omega \to \Lambda K$	+0.0024	0.41	0.41
	−0.0024	−0.97	−0.97
α_Ξ for $\Xi \to \Lambda\pi$	+0.014	0.89	0.88
	−0.014	0.58	0.29
α_Λ for $\Lambda \to p\pi$	+0.013	0.22	0.19
	−0.013	1.43	1.62
Ω lifetime	+0.33 mm	1.08	0.82
	−0.33 mm	3.00	2.53
Λ lifetime	+0.6 mm	1.32	0.98
	−0.6 mm	2.04	1.28
K lifetime	+7.2 mm	0.87	0.87
	−7.2 mm	1.58	1.58
Ξ lifetime	+0.45 mm	0.14	0.27
	−0.45 mm	−0.63	−0.62
$B(\Omega^- \to \Lambda K^-)$	$\pm 0.7 \cdot 10^{-2}$	±1.03	±1.03
$B(\Xi^- \to \Lambda\pi^-)$	$\pm 3.5 \cdot 10^{-4}$	∓0.04	∓0.04
$B(K^- \to \pi^+\pi^-\pi^-)$	$\pm 3.1 \cdot 10^{-4}$	±0.55	±0.55
MC statistics		±0.75	±0.70
Total		+6.43	+8.31
		−4.17	−4.32

Table 6.2. Systematic errors for antiparticle signal modes.

Source	Variation	$\frac{\delta B_{3b}}{B_{3b}}$ (%)	$\frac{\delta B_{res}}{B_{res}}$ (%)
Target x center	+0.69 mm	0.38	−1.87
	−0.69 mm	−0.70	1.50
Target y center	+0.93 mm	−0.99	−3.00
	−0.93 mm	−3.31	−1.22
Momentum Spectrum, p_z	uniform	3.49	6.53
Momentum Spectrum, p_x, p_y	broader	1.45	1.87
Hyperon Magnet, B-field	+0.1 %	−0.82	−1.13
	−0.1 %	−0.56	−0.10
Analyzing Magnets, B-field	+0.1 %	1.48	1.45
	−0.1 %	−0.83	−0.49
α_Ω for $\Omega \to \Lambda K$	+0.0038	0.58	0.58
	−0.0038	−0.33	−0.33
α_Ξ for $\Xi \to \Lambda\pi$	+0.014	0.89	0.88
	−0.014	0.58	0.29
α_Λ for $\Lambda \to p\pi$	+0.013	0.22	0.19
	−0.013	1.43	1.62
Ω lifetime	+0.33 mm	1.08	0.82
	−0.33 mm	3.00	2.53
Λ lifetime	+0.6 mm	1.32	0.98
	−0.6 mm	2.04	1.28
K lifetime	+7.2 mm	0.87	0.87
	−7.2 mm	1.58	1.58
Ξ lifetime	+0.45 mm	0.14	0.27
	−0.45 mm	−0.63	−0.62
$B(\Omega^- \to \Lambda K^-)$	$\pm 0.7 \cdot 10^{-2}$	±1.03	±1.03
$B(\Xi^- \to \Lambda\pi^-)$	$\pm 3.5 \cdot 10^{-4}$	∓0.04	∓0.04
$B(K^- \to \pi^+\pi^-\pi^-)$	$\pm 3.1 \cdot 10^{-4}$	±0.55	±0.55
MC statistics		±0.76	±0.70
Total		+6.44	+8.32
		−4.07	−4.23

CHAPTER 7

CONCLUSIONS

A clean signal of 78 (24) events has been observed in the rare nonleptonic particle (antiparticle) decay modes $\Omega^{\mp} \to \Xi^{\mp}\pi^{\pm}\pi^{\mp}$ and $\Omega^{\mp} \to \Xi^{*0}_{1530}(\overline{\Xi^{*0}_{1530}})\pi^{\mp}$ using data collected with the HyperCP (E871) spectrometer during Fermilab's 1999 fixed-target run. Including contributions from both the direct 3-body and the resonance decay modes to the final state $\Xi^{\mp}\pi^{\pm}\pi^{\mp}$, we calculate

$$B(\Omega^- \to \Xi^-\pi^+\pi^-) = [4.32 \pm 0.56(\text{stat}) \pm 0.28(\text{syst})] \times 10^{-4}\,, \quad (7.1)$$

$$B(\Omega^+ \to \Xi^+\pi^-\pi^+) = [3.13 \pm 0.71(\text{stat}) \pm 0.20(\text{syst})] \times 10^{-4}\,. \quad (7.2)$$

This is the first result for the antiparticle mode. Our measurement for the particle mode agrees with the previous experimental result [3] and has order-of-magnitude better precision.

The relative contribution of each channel was extracted using the unbinned generalized log-likelihood Dalitz plot fit. The first actual measurement of the resonance-mode branching ratios is

$$B(\Omega^- \to \Xi^{*0}_{1530}\pi^-) = [4.55 \pm 2.33(\text{stat}) \pm 0.38(\text{syst})] \times 10^{-5}\,, \quad (7.3)$$

$$B(\Omega^+ \to \overline{\Xi^{*0}_{1530}}\pi^+) = [1.40 \pm 2.83(\text{stat}) \pm 0.12(\text{syst})] \times 10^{-5}\,, \quad (7.4)$$

together with the improved branching ratios for the 3-body mode,

$$B(\Omega^- \to \Xi^-\pi^+\pi^-) = [3.58 \pm 0.71(\text{stat}) \pm 0.23(\text{syst})] \times 10^{-4}\,, \quad (7.5)$$

$$B(\Omega^+ \to \Xi^+\pi^-\pi^+) = [2.91 \pm 0.99(\text{stat}) \pm 0.19(\text{syst})] \times 10^{-4}\,. \quad (7.6)$$

The resonance-mode branching ratio disagrees with the current PDG value [32], being ≈ 14 times smaller. The particle- and antiparticle-mode results are consistent with each other. The statistical uncertainty dominates over systematics.

Since the central value of the resonance-mode branching ratio is less than 2σ away from zero (we add statistical and systematic errors from equations (7.3) and (7.4) in quadrature), we also calculate the branching ratio upper limits at 90% confidence level:

$$B(\Omega^- \to \Xi^{*0}_{1530}\pi^-) \;<\; 7.61 \times 10^{-5}\,, \tag{7.7}$$

$$B(\Omega^+ \to \overline{\Xi^{*0}_{1530}}\pi^+) \;<\; 5.61 \times 10^{-5}\,. \tag{7.8}$$

APPENDIX A

LIST OF RUNS USED

Table A.1. List of Negative'99 runs used in the analysis.

3743	3762	3763	3769	3770	3777	3778	3786	3789	3794
3795	3802	3803	3809	3810	3818	3823	3824	3825	3831
3833	3854	3855	3874	3881	3882	3888	3889	3895	3896
3901	3902	3908	3910	3918	3919	3924	3925	3930	3931
3939	3941	3956	3957	3964	3965	3972	3973	3979	3980
3988	3989	4000	4015	4019	4023	4027	4032	4040	4047
4052	4053	4058	4062	4071	4076	4080	4085	4090	4095
4100	4110	4114	4119	4127	4131	4135	4139	4143	4148
4152	4165	4169	4173	4200	4204	4208	4215	4216	4244
4249	4253	4257	4270	4281	4286	4293	4297	4305	4311
4316	4320	4332	4344	4346	4353	4358	4364	4368	4372
4376	4380	4394	4398	4404	4408	4409	4414	4418	4424
4428	4432	4437	4441	4445	4447	4451	4455	4462	4466
4474	4478	4482	4489	4493	4497	4513	4518	4522	4524
4536	4541	4545	4629	4633	4635	4639	4641	4642	4644
4648	4652	4657	4661	4667	4671	4676	4695	4700	4704
4708	4714	4721	4722	4727	4732	4736	4740	4746	4750
4759	4765	4774							

Table A.2. List of Positive'99 runs used in the analysis (continued in next table).

3735	3739	3741	3742	3760	3761	3764	3767	3768	3771
3773	3775	3776	3780	3781	3784	3785	3790	3792	3793
3798	3799	3800	3801	3804	3805	3806	3807	3811	3814
3815	3816	3819	3820	3821	3822	3826	3827	3828	3830
3834	3835	3836	3852	3858	3859	3860	3864	3872	3884
3885	3886	3887	3890	3891	3892	3893	3894	3897	3899
3900	3903	3905	3906	3907	3911	3912	3913	3917	3920
3921	3922	3923	3926	3927	3928	3929	3932	3934	3935
3936	3938	3942	3950	3951	3953	3954	3955	3958	3959
3960	3961	3968	3969	3970	3971	3974	3975	3976	3977
3981	3982	3983	3986	3992	3993	3996	3998	4001	4003
4004	4009	4010	4011	4016	4017	4018	4020	4021	4029

Table A.3. List of Positive'99 runs used in the analysis (previous table continued).

4030	4031	4033	4034	4035	4037	4038	4039	4044	4045
4046	4049	4050	4051	4054	4055	4056	4059	4060	4061
4063	4064	4070	4072	4073	4074	4077	4078	4079	4082
4083	4084	4086	4087	4088	4089	4091	4092	4094	4097
4098	4099	4101	4103	4111	4112	4113	4115	4117	4118
4120	4121	4122	4129	4130	4132	4133	4134	4136	4137
4138	4140	4141	4142	4144	4145	4146	4147	4149	4150
4151	4155	4156	4163	4164	4166	4167	4168	4170	4171
4172	4174	4175	4176	4197	4198	4199	4201	4202	4203
4205	4206	4207	4209	4210	4211	4217	4218	4243	4245
4247	4248	4250	4251	4252	4254	4255	4256	4258	4259
4261	4266	4267	4268	4269	4272	4273	4274	4283	4284
4285	4289	4290	4294	4295	4296	4298	4299	4300	4306
4308	4309	4312	4313	4314	4317	4318	4319	4321	4328
4329	4331	4335	4336	4337	4338	4347	4349	4352	4355
4356	4357	4359	4360	4363	4365	4366	4367	4369	4370
4371	4373	4374	4375	4377	4378	4379	4381	4382	4386
4387	4395	4396	4397	4399	4400	4405	4406	4407	4410
4411	4412	4415	4416	4417	4420	4421	4423	4425	4426
4427	4429	4430	4431	4433	4435	4436	4438	4439	4440
4442	4443	4444	4448	4449	4450	4452	4453	4454	4456
4457	4460	4463	4464	4465	4468	4469	4470	4475	4476
4477	4479	4480	4481	4484	4485	4488	4490	4491	4492
4494	4495	4496	4500	4511	4512	4514	4515	4516	4519
4520	4521	4525	4528	4529	4530	4533	4534	4535	4537
4539	4540	4543	4544	4546	4547	4630	4631	4632	4636
4637	4638	4645	4646	4647	4649	4650	4651	4653	4655
4658	4659	4660	4662	4663	4664	4668	4669	4670	4673
4674	4677	4678	4679	4680	4684	4685	4694	4696	4697
4698	4705	4706	4707	4711	4712	4713	4715	4716	4717
4723	4724	4726	4728	4731	4733	4734	4735	4738	4739
4742	4745	4747	4748	4749	4751	4753	4756	4757	4760
4761	4762	4767	4768	4770	4771	4775	4776	4777	4784

APPENDIX B

FINAL EVENT SELECTION PLOTS FOR POSITIVE 99 DATA SUBSET

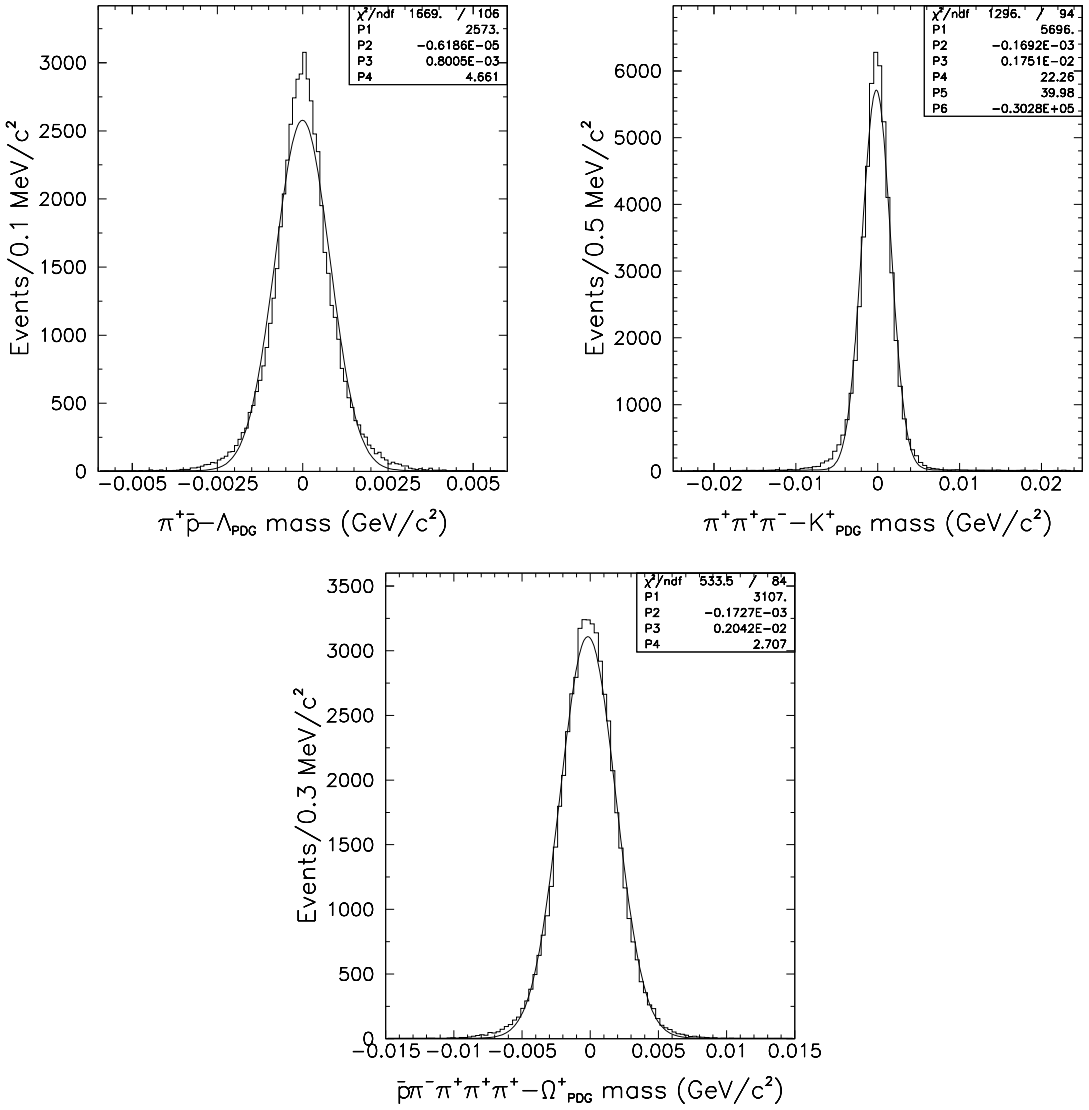

Figure B.1. Difference between reconstructed invariant mass with no cuts and PDG values for the normalizing-mode Pos99 MC. Solid line is Gaussian-plus-polynomial fit.

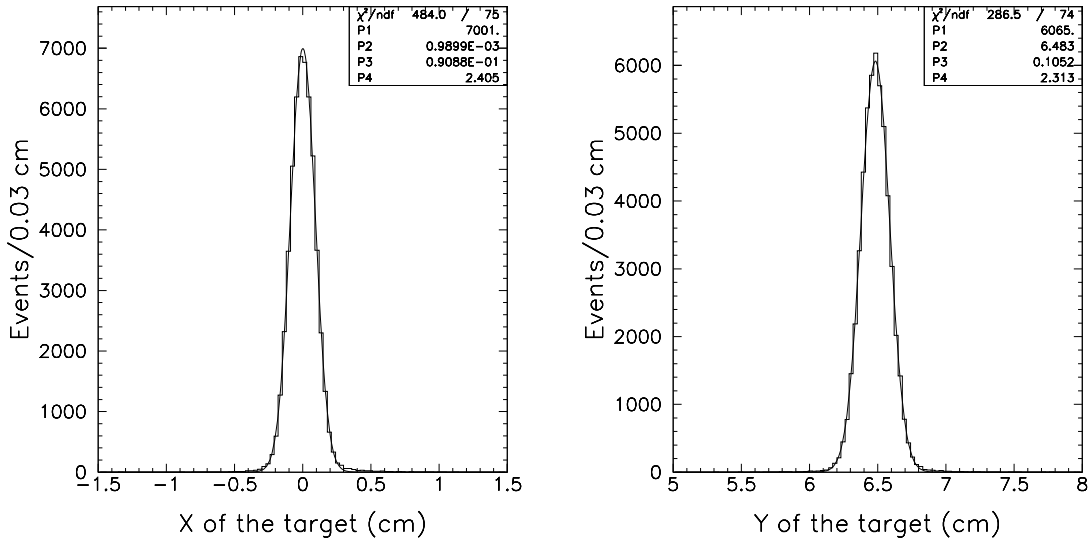

Figure B.2. X and Y positions of the Ω^+ at the target with no cuts for the normalizing-mode Pos99 MC. Solid line is Gaussian-plus-constant fit.

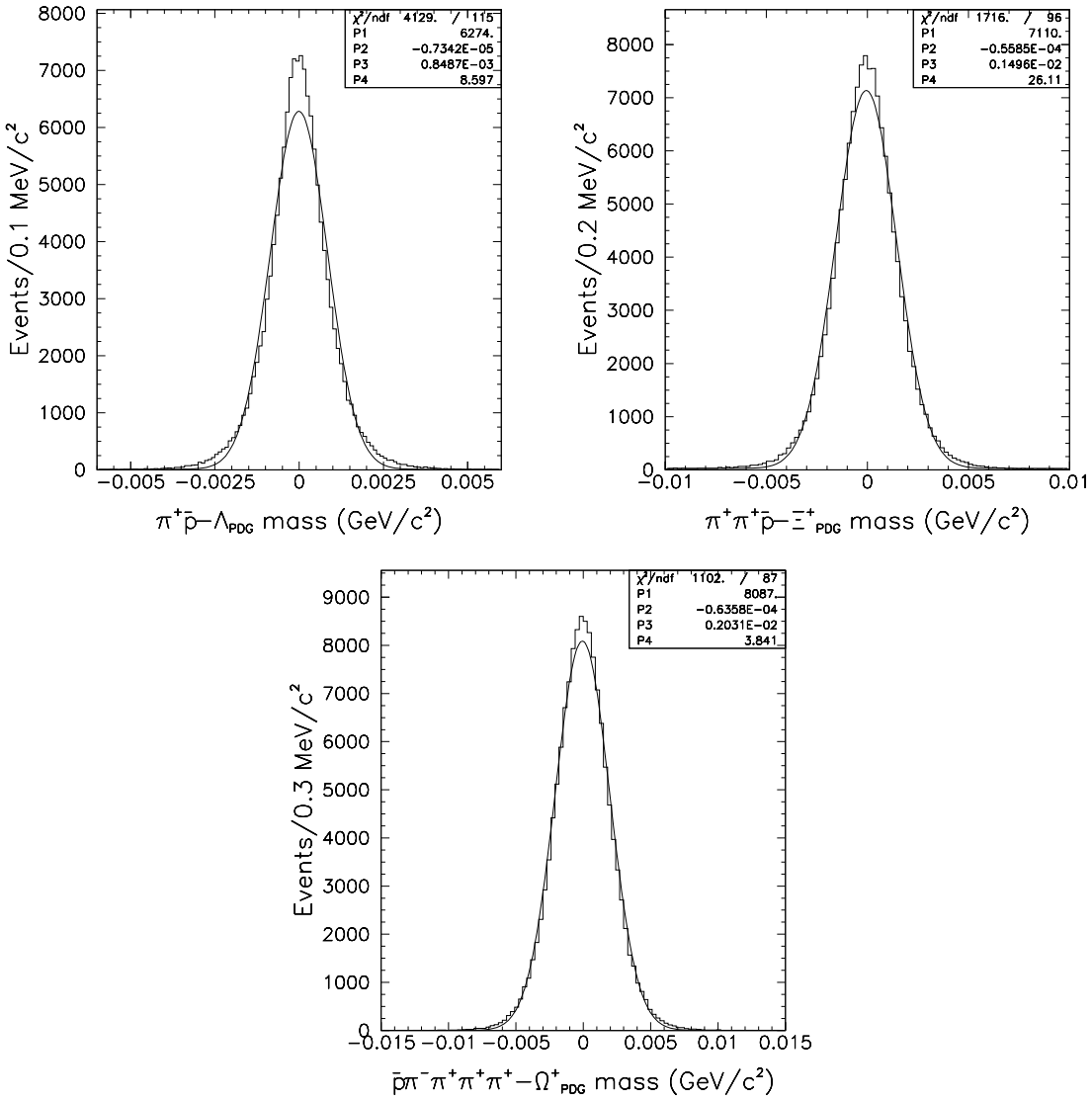

Figure B.3. Difference between reconstructed invariant mass with no cuts and PDG values for the signal 3-body-mode Pos99 MC. Solid line is Gaussian-plus-constant fit.

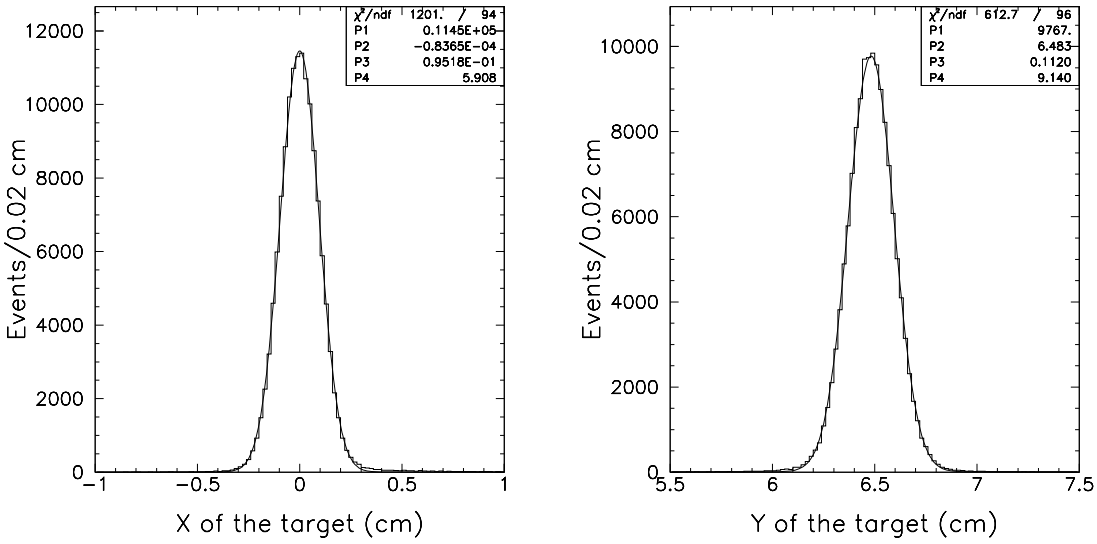

Figure B.4. X and Y positions of the Ω^+ at the target with no cuts for the signal 3-body-mode Pos99 MC. Solid line is Gaussian-plus-constant fit.

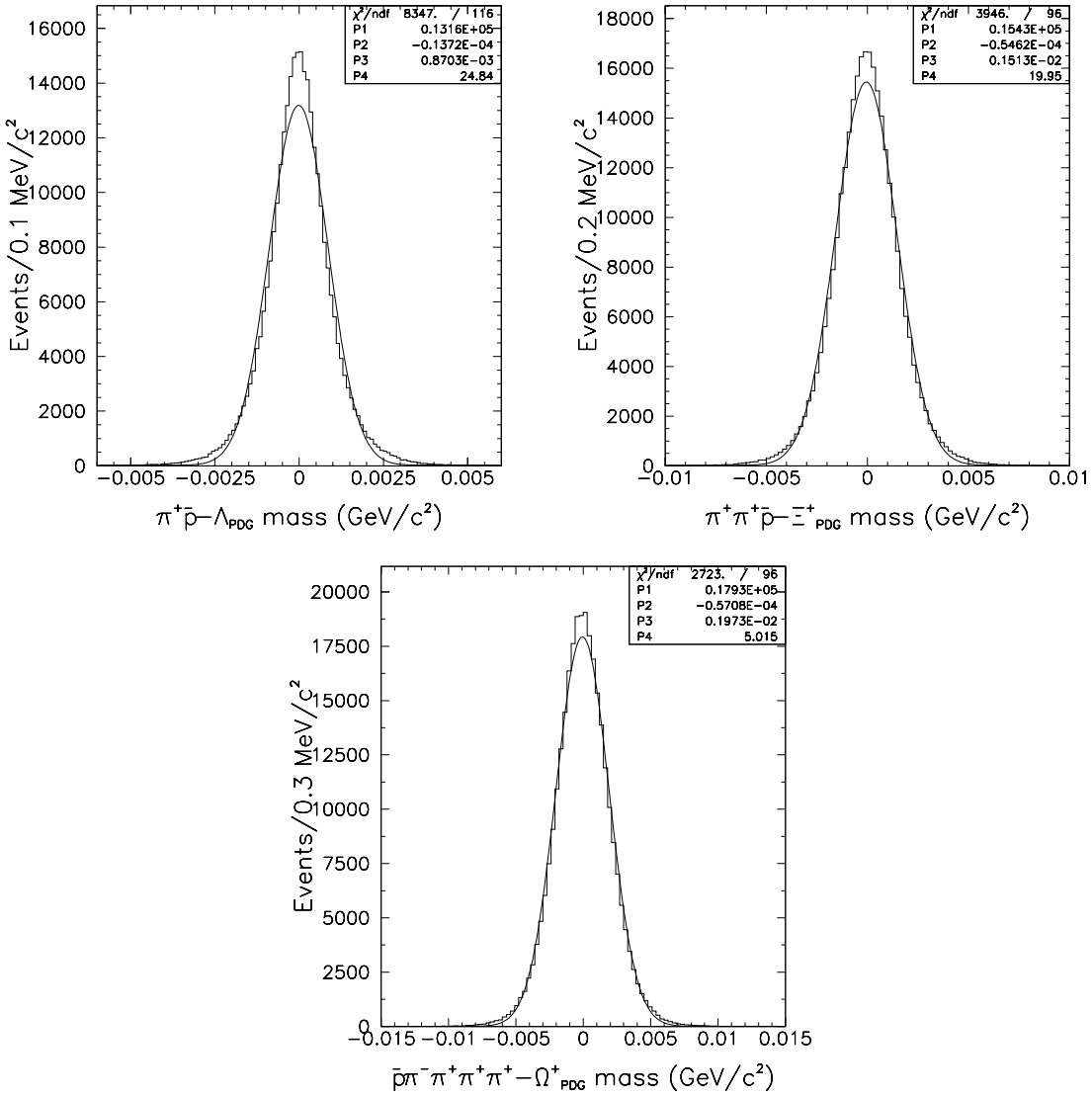

Figure B.5. Difference between reconstructed invariant mass with no cuts and PDG values for the signal resonance-mode Pos99 MC. Solid line is Gaussian-plus-constant fit.

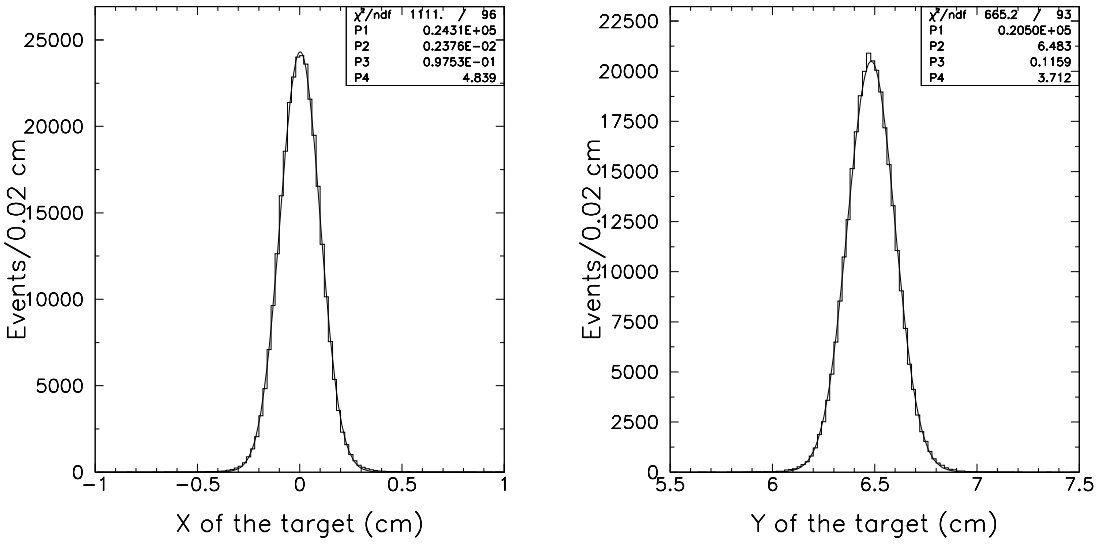

Figure B.6. X and Y positions of the Ω^+ at the target with no cuts for the signal resonance-mode Pos99 MC. Solid line is Gaussian-plus-constant fit.

APPENDIX C

MONTE CARLO TUNING AND COMPARISON WITH DATA PLOTS FOR POSITIVE 99 DATA SUBSET

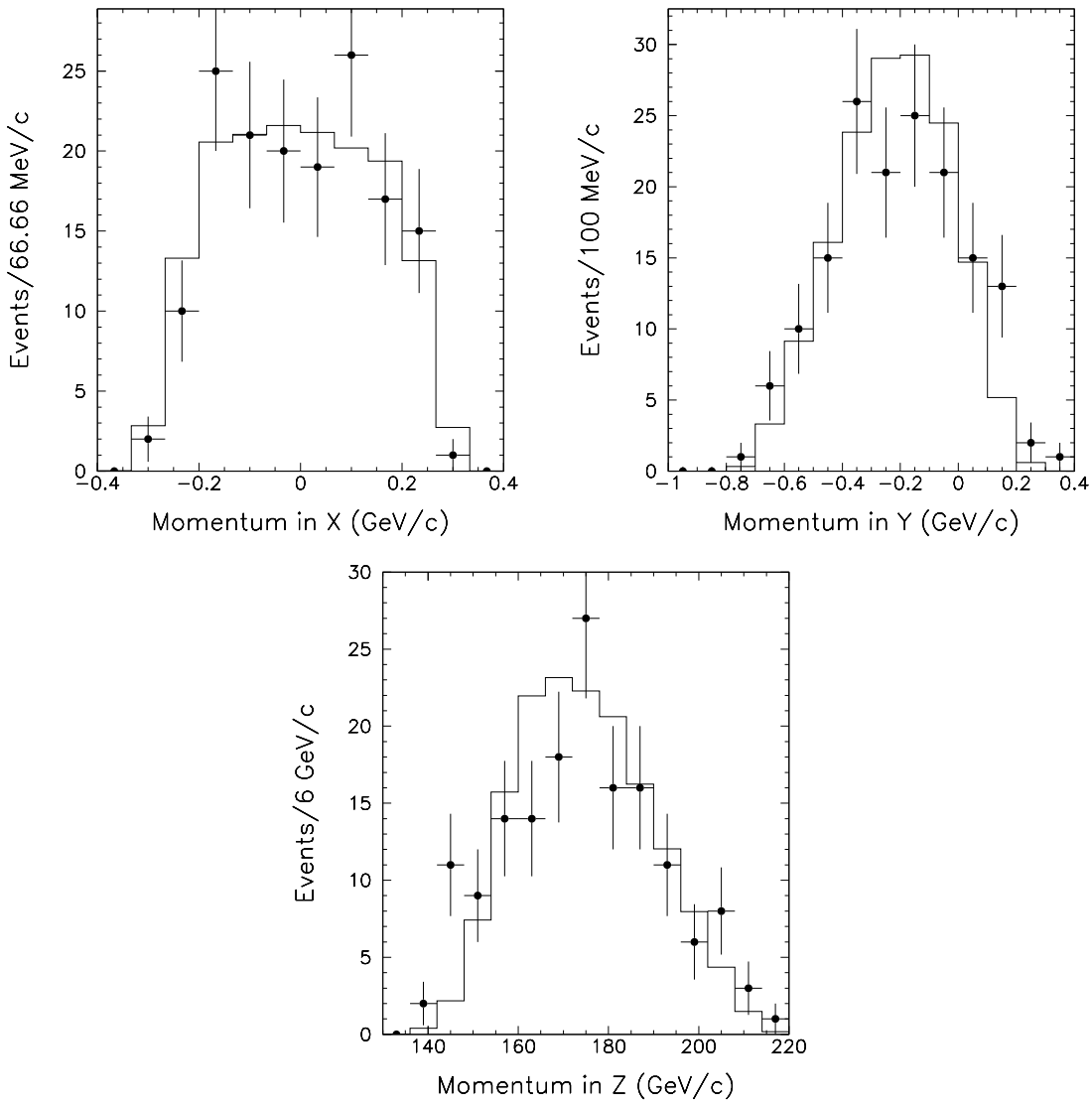

Figure C.1. Data (Pos99) and MC comparison for x, y, and z projections of the Ω^+ momentum after the cuts. Normalizing mode.

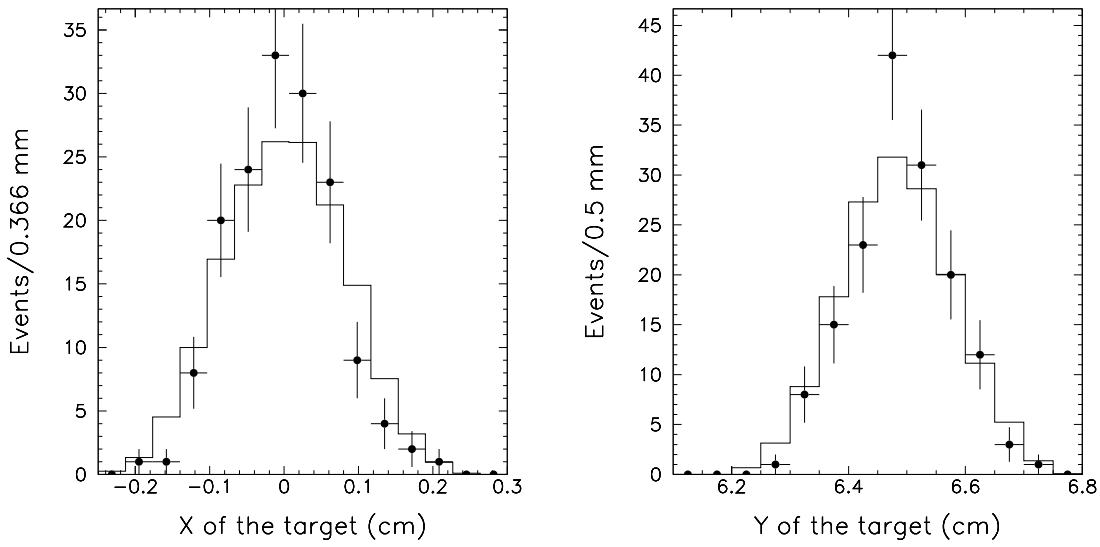

Figure C.2. Data (Pos99) and MC comparison for x and y positions of the Ω^+ at the target after the cuts. Normalizing mode.

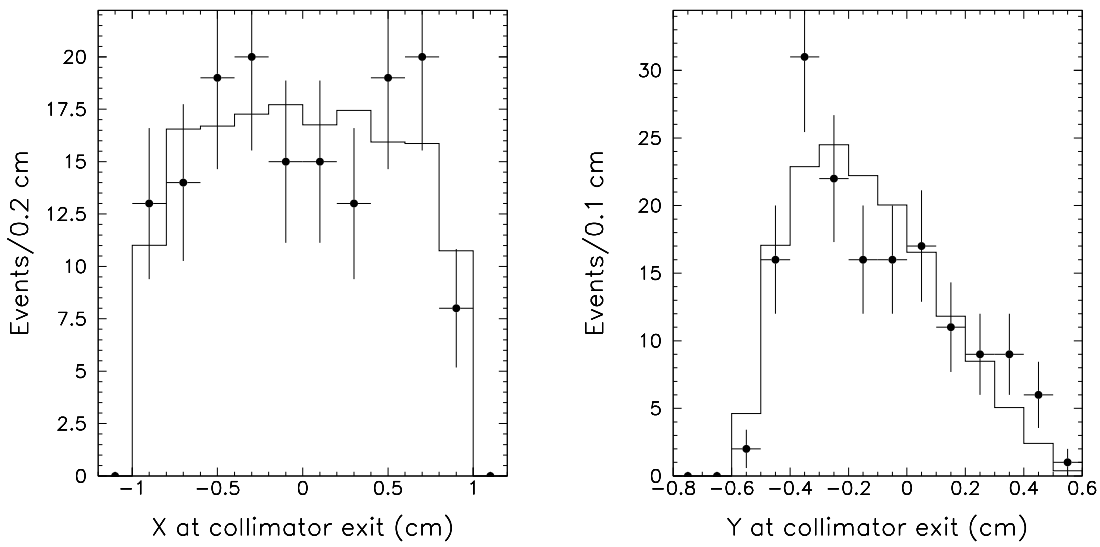

Figure C.3. Data (Pos99) and MC comparison for x and y positions of the Ω^+ at the collimator exit after the cuts. Normalizing mode.

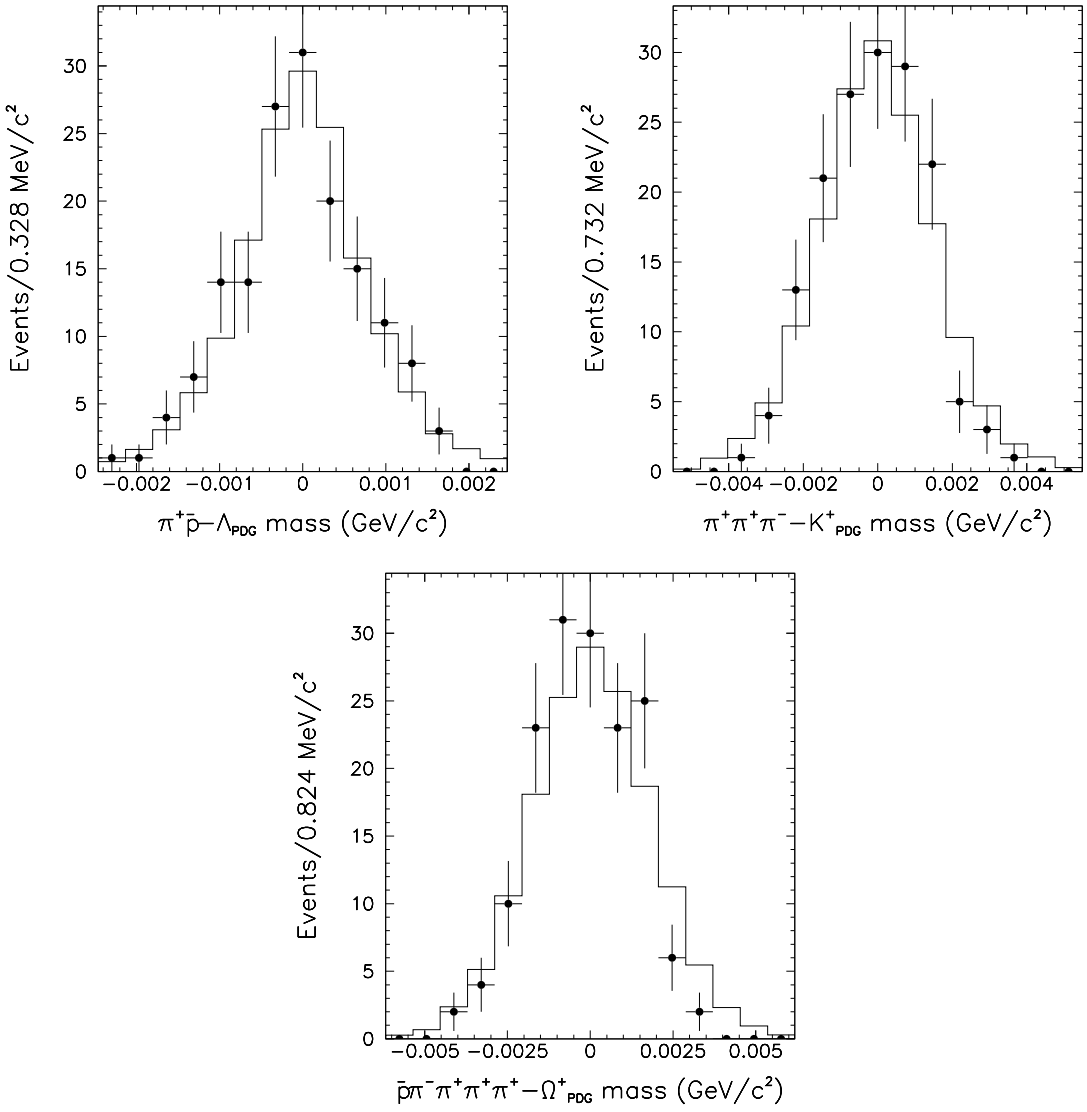

Figure C.4. Data (Pos99) and MC comparison for the difference between reconstructed invariant mass after the cuts and PDG values. Normalizing mode.

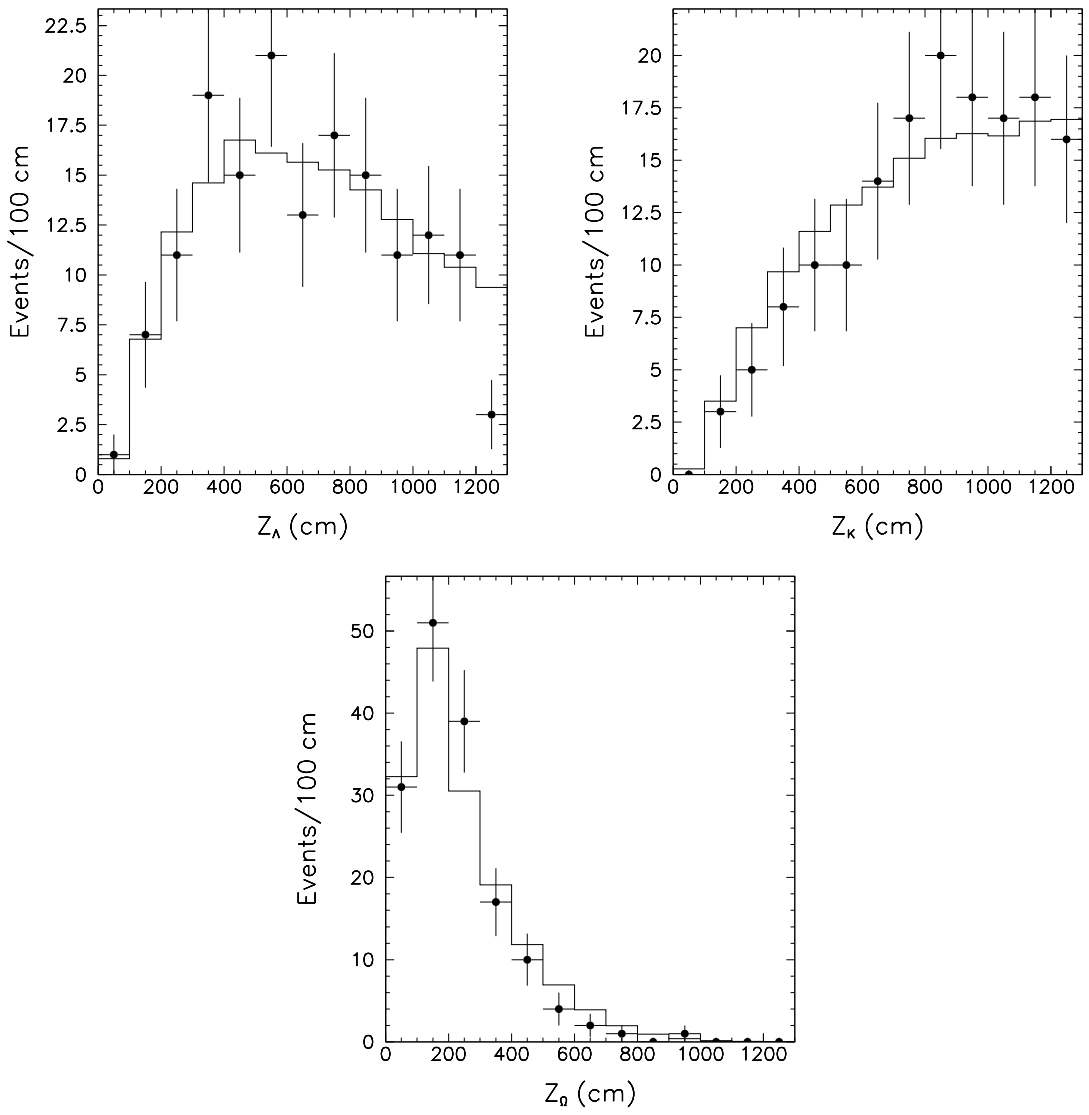

Figure C.5. Data (Pos99) and MC comparison for the z position of the decay vertex after the cuts. Normalizing mode.

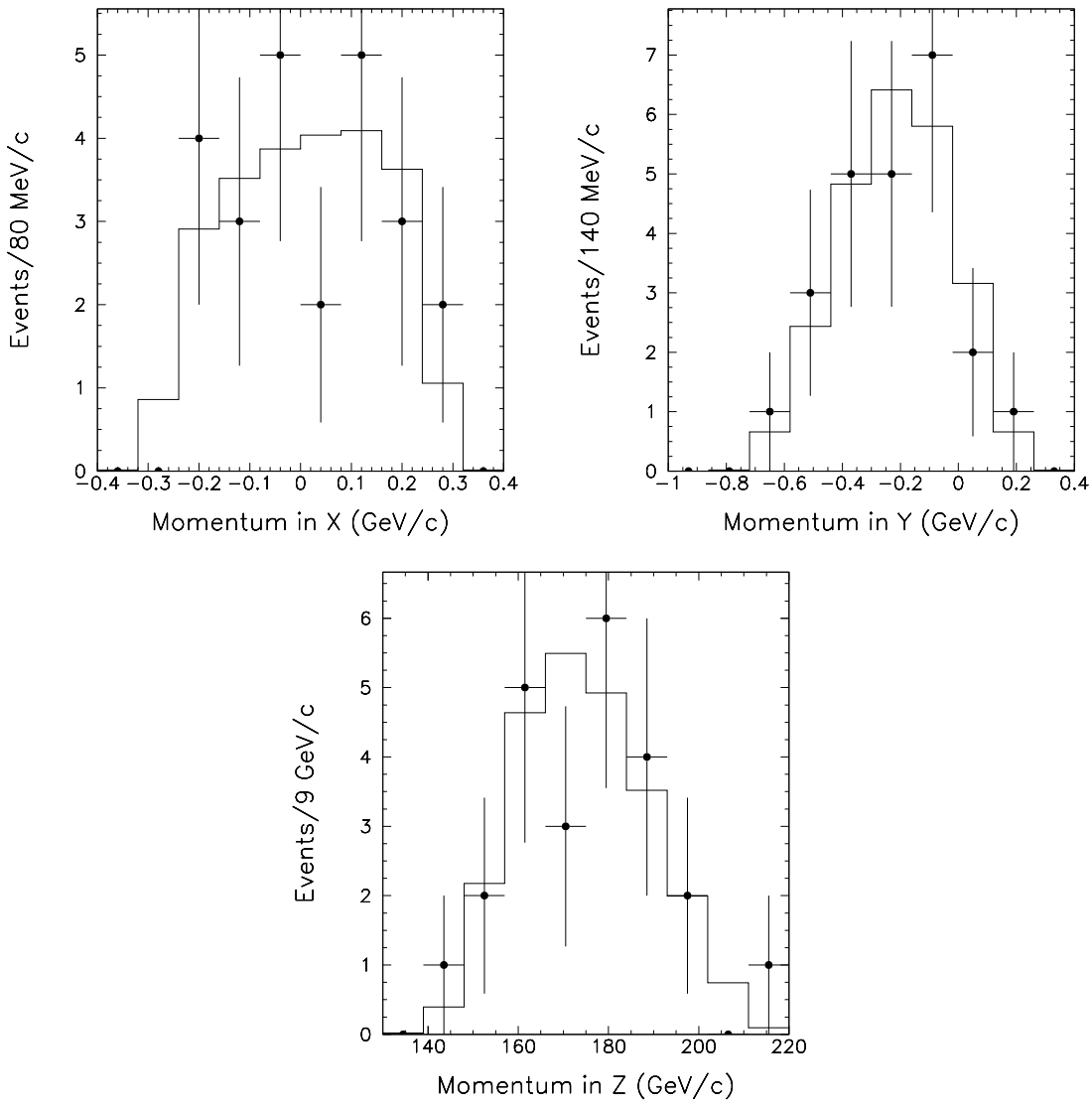

Figure C.6. Data (Pos99) and MC comparison for x, y, and z projections of the Ω^+ momentum after the cuts. Signal mode.

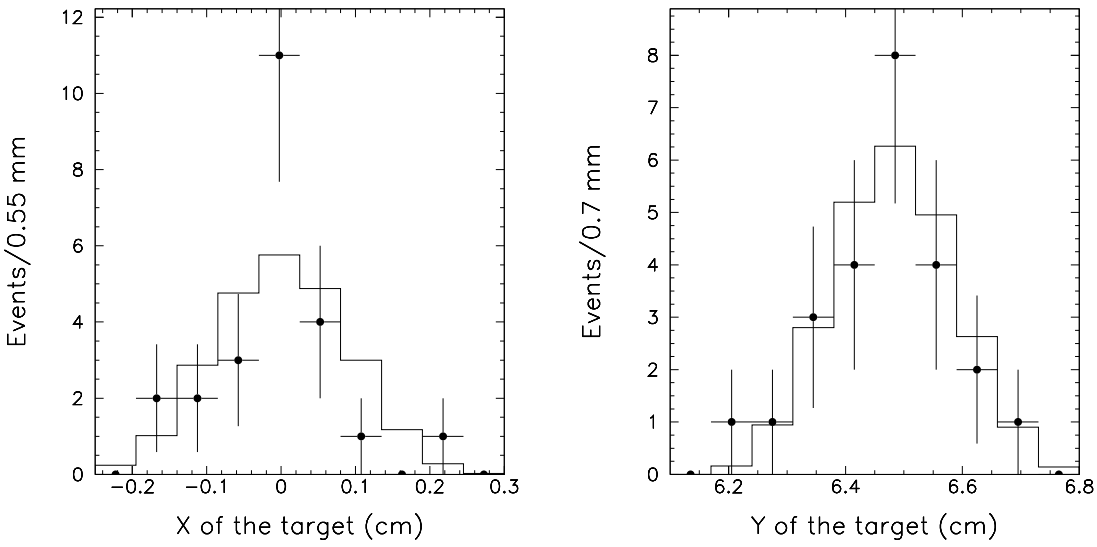

Figure C.7. Data (Pos99) and MC comparison for x and y positions of the Ω^+ at the target after the cuts. Signal mode.

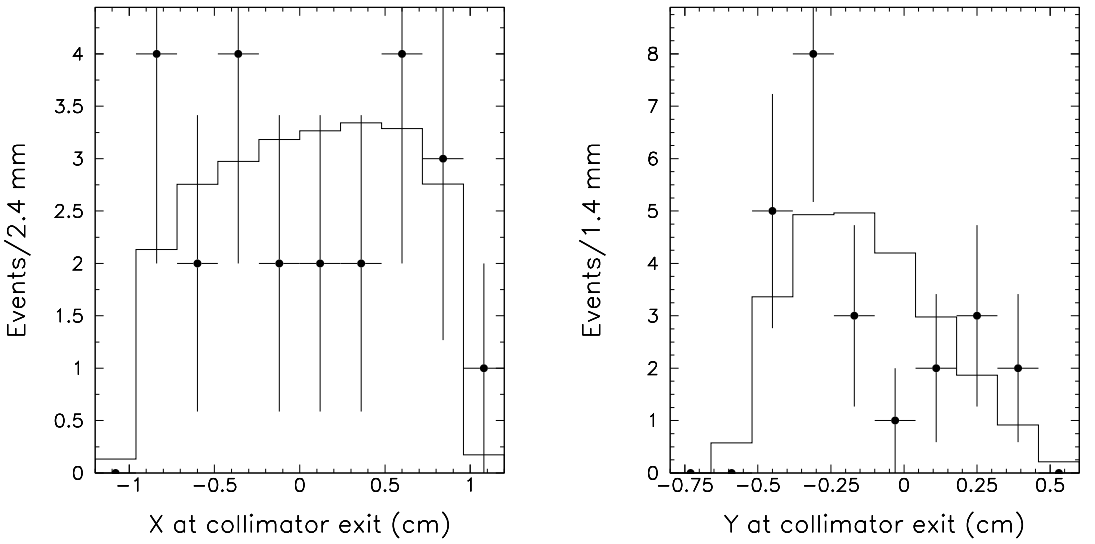

Figure C.8. Data (Pos99) and MC comparison for x and y positions of the Ω^+ at the collimator exit after the cuts. Signal mode.

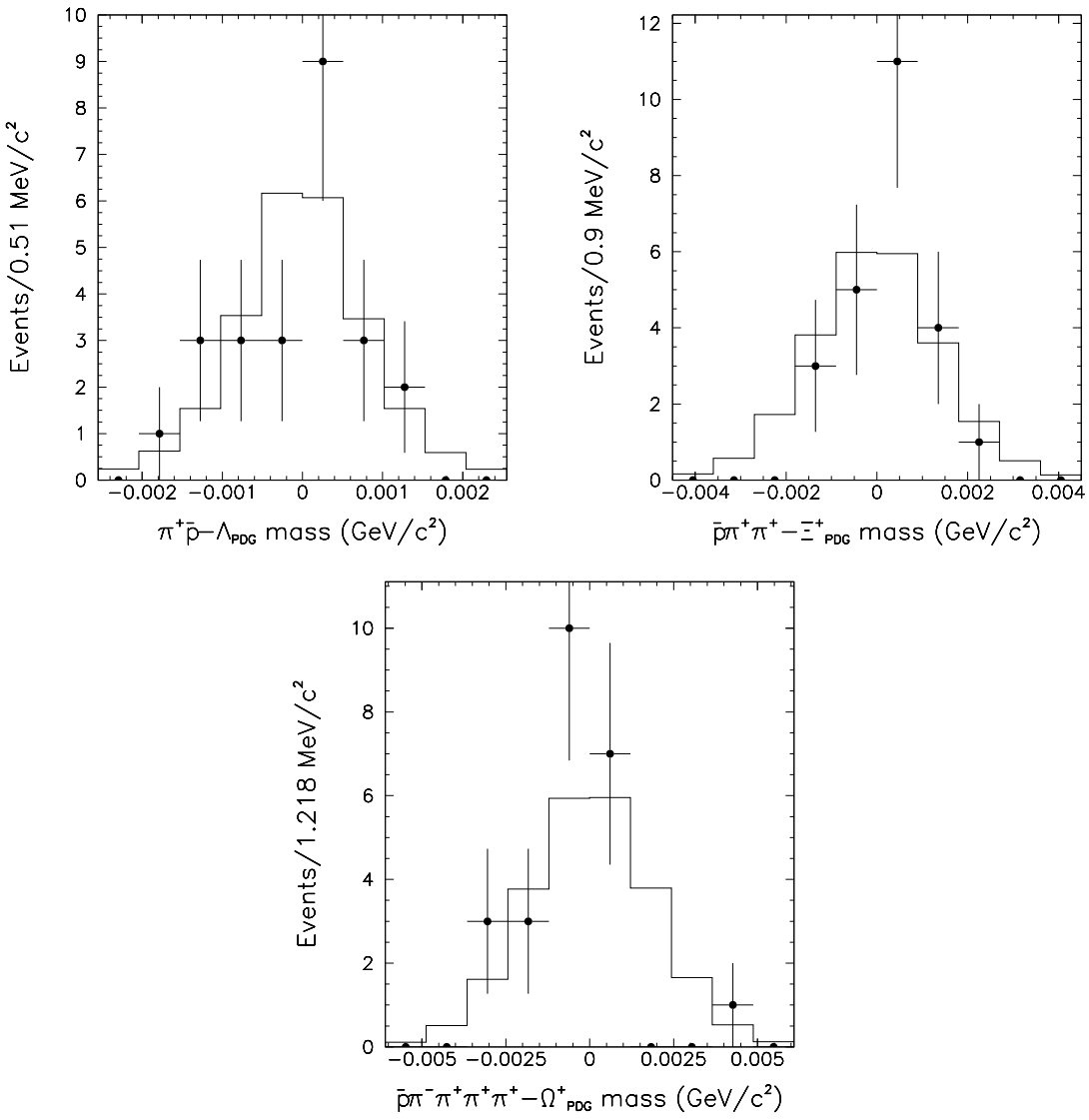

Figure C.9. Data (Pos99) and MC comparison for the difference between reconstructed invariant mass after the cuts and PDG values. Signal mode.

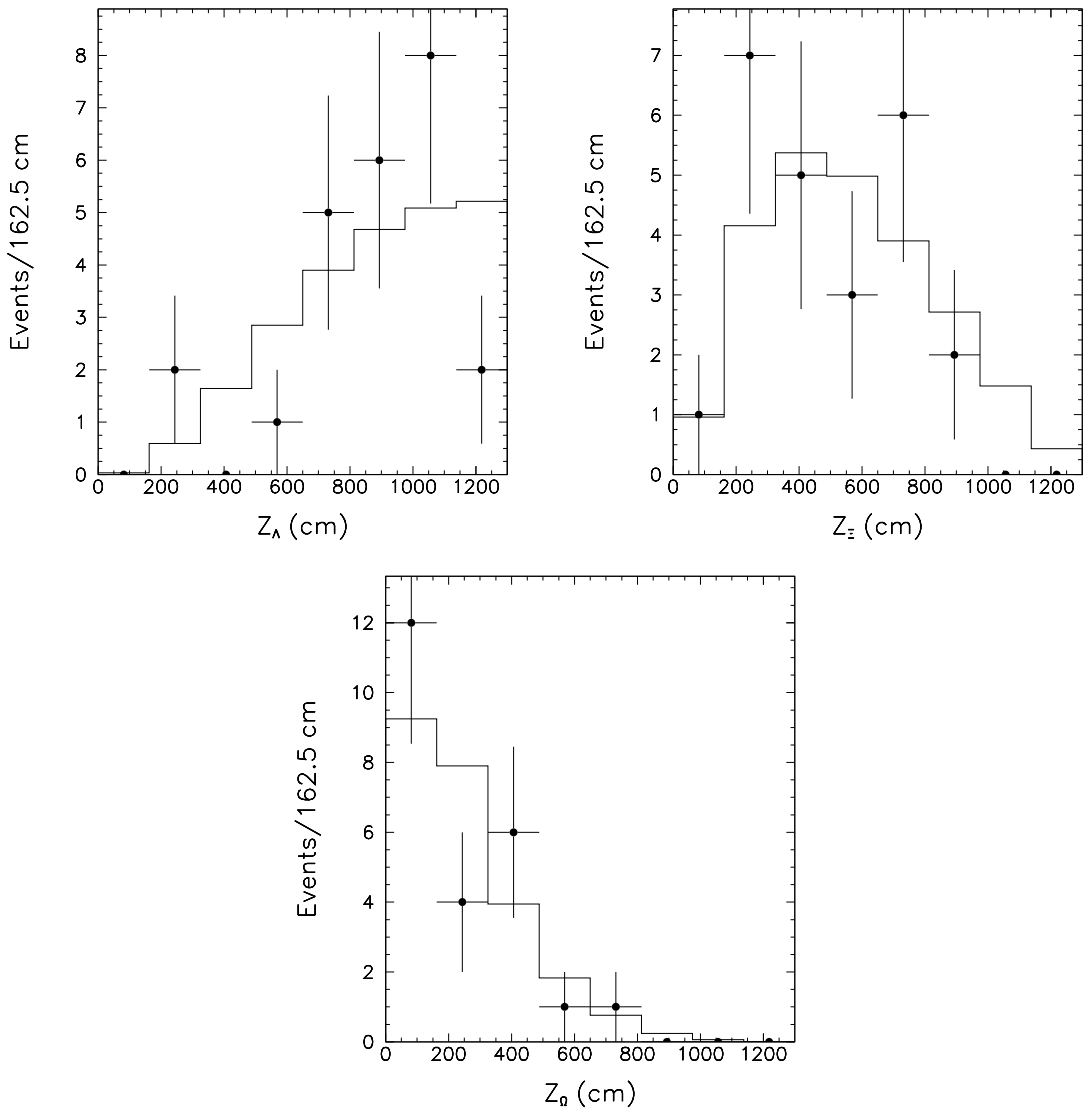

Figure C.10. Data (Pos99) and MC comparison for the z position of the decay vertex after the cuts. Signal mode.

APPENDIX D

MINUIT OUTPUT: FITS TO EXTRACT THE NUMBERS OF NORMALIZING AND SIGNAL MODE EVENTS

Negative99 normalizing mode data. MINOS command output:

```
FCN=  -1101.703     FROM MINOS     STATUS=SUCCESSFUL   231 CALLS
409 TOTAL EDM=  0.44E-07    STRATEGY= 2      ERROR MATRIX ACCURATE
  EXT PARAMETER                   PARABOLIC         MINOS ERRORS
  NO.   NAME        VALUE           ERROR      NEGATIVE      POSITIVE
   1  # signal      373.89         19.403       -19.073        19.734
   2  mean  (MeV)   1672.4       0.88119E-01  -0.88119E-01   0.88241E-01
   3  sigma (MeV)   1.6734       0.68727E-01  -0.66957E-01   0.70582E-01
   4  # bkg         7.1122         3.1106       -2.6968        3.5431
   5      5         1620.0       constant
   6      6         1700.0       constant
                                ERR DEF= 0.500
```

Positive99 normalizing mode data. MINOS command output:

```
FCN=  -334.2250     FROM MINOS     STATUS=SUCCESSFUL   242 CALLS
498 TOTAL EDM=  0.20E-12    STRATEGY= 2      ERROR MATRIX ACCURATE
  EXT PARAMETER                   PARABOLIC         MINOS ERRORS
  NO.   NAME        VALUE           ERROR      NEGATIVE      POSITIVE
   1  # signal      155.45         12.500       -12.162        12.828
   2  mean  (MeV)   1672.3       0.11860      -0.11882       0.11874
   3  sigma (MeV)   1.4692       0.84700E-01  -0.81089E-01   0.88717E-01
   4  # bkg         4.5509         2.2742       -1.9127        2.6670
   5      5         1620.0       constant
   6      6         1700.0       constant
                                ERR DEF= 0.500
```

Negative99 signal mode data. MINOS command output:

```
FCN=  -50.02664     FROM MINOS     STATUS=SUCCESSFUL   203 CALLS
466 TOTAL EDM=  0.47E-11    STRATEGY= 2      ERROR MATRIX ACCURATE
 EXT PARAMETER                   PARABOLIC         MINOS ERRORS
 NO.   NAME        VALUE           ERROR      NEGATIVE      POSITIVE
  1  # signal      74.000         8.8554       -8.5268        9.1904
  2  mean  (MeV)   1672.1        0.21817      -0.21841       0.21915
  3  sigma (MeV)   1.7724        0.15826      -0.14963       0.16855
  4  # bkg         32.000         6.0346       -5.6620        6.4182
  5      5         1650.0        constant
  6      6         1730.0        constant
                              ERR DEF= 0.500
```

Positive99 signal mode data. MINOS command output:

```
FCN= -0.2765267     FROM MINOS     STATUS=SUCCESSFUL   343 CALLS
508 TOTAL EDM=  0.81E-11    STRATEGY= 2      ERROR MATRIX ACCURATE
 EXT PARAMETER                   PARABOLIC         MINOS ERRORS
 NO.   NAME        VALUE           ERROR      NEGATIVE      POSITIVE
  1  # signal      22.727         4.7991       -4.4719        5.1384
  2  mean  (MeV)   1671.8        0.21656      -0.21867       0.21980
  3  sigma (MeV)   1.0181        0.15581      -0.13741       0.18464
  4  # bkg         4.2731         2.1394       -1.7988        2.5099
  5      5         1650.0        constant
  6      6         1730.0        constant
                              ERR DEF= 0.500
```

APPENDIX E

MINUIT OUTPUT: FIT TO EXTRACT PROPORTIONALITY COEFFICIENTS USING NEGATIVE99 DATA

Fit to the reconstructed invariant $p\pi^+\pi^-\pi^-$ mass:

```
COVARIANCE MATRIX CALCULATED SUCCESSFULLY FCN=   81.45359
FROM HESSE     STATUS=OK             10 CALLS      120 TOTAL
EDM=0.35E-15    STRATEGY= 2      ERROR MATRIX ACCURATE
  EXT PARAMETER                                   INTERNAL      INTERNAL
  NO.   NAME        VALUE           ERROR       STEP SIZE       VALUE
   1     3b        0.85055       0.12811       0.44417E-05   0.85055
   2     res       0.14945       0.86149E-01   0.29872E-05   0.14945
                                ERR DEF= 0.500
 EXTERNAL ERROR MATRIX.    NDIM=  50    NPAR=  2    ERR DEF= 0.500
  0.164E-01-0.551E-02
 -0.551E-02 0.742E-02
 PARAMETER  CORRELATION COEFFICIENTS
       NO.  GLOBAL     1     2
        1  0.49889  1.000-0.499
        2  0.49889 -0.499 1.000
ENTER MINUIT COMMAND:
mino
 MINUIT TASK:
 FCN=   81.45359
 FROM MINOS     STATUS=SUCCESSFUL    66 CALLS      186 TOTAL
 EDM=  0.35E-15    STRATEGY= 2      ERROR MATRIX ACCURATE
  EXT PARAMETER                  PARABOLIC         MINOS ERRORS
  NO.   NAME        VALUE           ERROR      NEGATIVE      POSITIVE
   1     3b        0.85055       0.12811      -0.12309       0.13315
   2     res       0.14945       0.86149E-01  -0.80346E-01   0.91920E-01
```

Two-dimensional Dalitz plot fit:

```
COVARIANCE MATRIX CALCULATED SUCCESSFULLY FCN=   336.1401
FROM HESSE     STATUS=OK             10 CALLS      664 TOTAL
EDM=  0.79E-13    STRATEGY= 2      ERROR MATRIX ACCURATE
  EXT PARAMETER                                   INTERNAL      INTERNAL
  NO.   NAME        VALUE           ERROR       STEP SIZE       VALUE
   1     3b        0.82768       0.12513       0.14274E-05   0.82768
   2     res       0.17232       0.85405E-01   0.12198E-05   0.17232
                                ERR DEF= 0.500
 EXTERNAL ERROR MATRIX.    NDIM=  50    NPAR=  2    ERR DEF= 0.500
  0.157E-01-0.507E-02
 -0.507E-02 0.729E-02
 PARAMETER  CORRELATION COEFFICIENTS
       NO.  GLOBAL     1     2
        1  0.47464  1.000-0.475
        2  0.47464 -0.475 1.000
ENTER MINUIT COMMAND:
mino
 MINUIT TASK:
 FCN=   336.1401
 FROM MINOS     STATUS=SUCCESSFUL    63 CALLS      727 TOTAL
 EDM=  0.79E-13    STRATEGY= 2      ERROR MATRIX ACCURATE
  EXT PARAMETER                  PARABOLIC         MINOS ERRORS
  NO.   NAME        VALUE           ERROR      NEGATIVE      POSITIVE
   1     3b        0.82768       0.12513      -0.12042       0.13037
   2     res       0.17232       0.85405E-01  -0.79763E-01   0.91299E-01
```

Fit to the $\cos\psi$ distribution:

```
COVARIANCE MATRIX CALCULATED SUCCESSFULLY FCN=   75.75967
FROM HESSE     STATUS=OK             10 CALLS       85 TOTAL
EDM=  0.32E-10    STRATEGY= 2      ERROR MATRIX ACCURATE
  EXT PARAMETER                                   INTERNAL      INTERNAL
  NO.   NAME        VALUE           ERROR       STEP SIZE       VALUE
   1     3b        0.89826       0.14504       0.27143E-04   0.89826
   2     res       0.10174       0.10404       0.19477E-04   0.10174
                                ERR DEF= 0.500
 EXTERNAL ERROR MATRIX.    NDIM=  50    NPAR=  2    ERR DEF= 0.500
  0.210E-01-0.952E-02
 -0.952E-02 0.108E-01
 PARAMETER  CORRELATION COEFFICIENTS
       NO.  GLOBAL     1     2
        1  0.63089  1.000-0.631
        2  0.63089 -0.631 1.000
ENTER MINUIT COMMAND:
mino
MINUIT TASK:
 FCN=   75.75967
 FROM MINOS     STATUS=SUCCESSFUL    60 CALLS      145 TOTAL
 EDM=  0.32E-10    STRATEGY= 2      ERROR MATRIX ACCURATE
  EXT PARAMETER                  PARABOLIC         MINOS ERRORS
  NO.   NAME        VALUE           ERROR      NEGATIVE      POSITIVE
   1     3b        0.89826       0.14504      -0.13950       0.15061
   2     res       0.10174       0.10404      -0.98474E-01   0.10960
```

APPENDIX F

MINUIT OUTPUT: FIT TO EXTRACT PROPORTIONALITY COEFFICIENTS USING POSITIVE99 DATA

Fit to the reconstructed invariant $\overline{p}\pi^-\pi^+\pi^+$ mass:

```
COVARIANCE MATRIX CALCULATED SUCCESSFULLY FCN=   54.40069
FROM HESSE     STATUS=OK             10 CALLS       87 TOTAL
EDM=  0.20E-10    STRATEGY= 2      ERROR MATRIX ACCURATE
  EXT PARAMETER                                   INTERNAL      INTERNAL
  NO.   NAME        VALUE           ERROR       STEP SIZE       VALUE
   1     3b        0.97267       0.24547       0.41726E-04   0.97267
   2     res       0.27330E-01   0.14446       0.49054E-05   0.27330E-01
                                ERR DEF= 0.500
 EXTERNAL ERROR MATRIX.    NDIM=  50    NPAR=  2    ERR DEF= 0.500
  0.603E-01-0.197E-01
 -0.197E-01 0.209E-01
 PARAMETER  CORRELATION COEFFICIENTS
       NO.  GLOBAL     1     2
        1  0.55636  1.000-0.556
        2  0.55636 -0.556 1.000
ENTER MINUIT COMMAND:
mino
MINUIT TASK:
FCN=   54.40069
FROM MINOS     STATUS=SUCCESSFUL    90 CALLS      177 TOTAL
EDM=  0.20E-10    STRATEGY= 2      ERROR MATRIX ACCURATE
  EXT PARAMETER                  PARABOLIC         MINOS ERRORS
  NO.   NAME        VALUE           ERROR      NEGATIVE      POSITIVE
   1     3b        0.97267       0.24547      -0.23081       0.26073
   2     res       0.27330E-01   0.14446      -0.12051       0.16823
```

Two-dimensional Dalitz plot fit:

```
COVARIANCE MATRIX CALCULATED SUCCESSFULLY FCN=   133.8691
FROM HESSE     STATUS=OK             10 CALLS      212 TOTAL
EDM=  0.84E-10    STRATEGY= 2      ERROR MATRIX ACCURATE
  EXT PARAMETER                                   INTERNAL      INTERNAL
  NO.   NAME        VALUE           ERROR       STEP SIZE       VALUE
   1     3b        0.92735       0.23844       0.65017E-04   0.92735
   2     res       0.72656E-01   0.14576       0.39746E-04   0.72656E-01
                                ERR DEF= 0.500
 EXTERNAL ERROR MATRIX.    NDIM=  50    NPAR=  2    ERR DEF= 0.500
  0.569E-01-0.182E-01
 -0.182E-01 0.212E-01
 PARAMETER  CORRELATION COEFFICIENTS
       NO.  GLOBAL     1     2
        1  0.52414  1.000-0.524
        2  0.52414 -0.524 1.000
ENTER MINUIT COMMAND:
mino
 MINUIT TASK:
 FCN=   133.8691
 FROM MINOS     STATUS=SUCCESSFUL    87 CALLS      299 TOTAL
 EDM=  0.84E-10    STRATEGY= 2      ERROR MATRIX ACCURATE
  EXT PARAMETER                  PARABOLIC         MINOS ERRORS
  NO.   NAME        VALUE           ERROR      NEGATIVE      POSITIVE
   1     3b        0.92735       0.23844      -0.22429       0.25314
   2     res       0.72656E-01   0.14576      -0.12093       0.16978
```

Fit to the $\cos\psi$ distribution:

```
COVARIANCE MATRIX CALCULATED SUCCESSFULLY FCN=   50.94555
FROM HESSE     STATUS=OK             10 CALLS       75 TOTAL
EDM=  0.11E-09    STRATEGY= 2      ERROR MATRIX ACCURATE
  EXT PARAMETER                                   INTERNAL      INTERNAL
  NO.   NAME        VALUE           ERROR       STEP SIZE       VALUE
   1     3b        0.73651       0.26109       0.39198E-04   0.73651
   2     res       0.26349       0.22014       0.33073E-04   0.26349
                                ERR DEF= 0.500
 EXTERNAL ERROR MATRIX.    NDIM=  50    NPAR=  2    ERR DEF= 0.500
  0.682E-01-0.375E-01
 -0.375E-01 0.485E-01
 PARAMETER  CORRELATION COEFFICIENTS
       NO.  GLOBAL     1     2
        1  0.65212  1.000-0.652
        2  0.65212 -0.652 1.000
ENTER MINUIT COMMAND:
mino
 MINUIT TASK:
 FCN=   50.94555
 FROM MINOS     STATUS=SUCCESSFUL    74 CALLS      149 TOTAL
 EDM=  0.11E-09    STRATEGY= 2      ERROR MATRIX ACCURATE
  EXT PARAMETER                  PARABOLIC         MINOS ERRORS
  NO.   NAME        VALUE           ERROR      NEGATIVE      POSITIVE
   1     3b        0.73651       0.26109      -0.24025       0.28153
   2     res       0.26349       0.22014      -0.20473       0.23523
```

BIBLIOGRAPHY

[1] Antipin, O., J. Tandean, and G. Valencia. "The Decay $\Omega^- \to \Xi^-\pi^+\pi^-$ in Chiral Perturbation Theory." *Phys. Rev. D* 76 (2007): 094024.

[2] Bourquin, M., and others. "First measurement of the Ω^- decay branching ratios." *Phys. Lett.* B88 (1979): 192–198.

[3] Bourquin, M., and others. "Measurement of Ω^- decay properties in the CERN SPS hyperon beam." *Nucl. Phys.* B241 (1984): 1–47.

[4] Burnstein, R. A., and others. "HyperCP: A high-rate spectrometer for the study of charged hyperon and kaon decays." *Nucl. Instrum. Meth. A* 541 (2005): 516–565.

[5] Byers, N., and S. Fenster. "Determination of spin and decay parameters of fermion states." *Phys. Rev. Lett.* 1 (1963): 52–55.

[6] CERN Program Library. "N-Body Monte-Carlo Event Generator." CERN Geneva, Switzerland, n.d., http://cernlib.web.cern.ch/cernlib/mc/genbod.html (accessed November 20, 2007).

[7] CERN Program Library Long Writeup Y250. "Statistical differences between histograms." CERN Geneva, Switzerland, 1994, http://wwwasdoc.web.cern.ch/wwwasdoc/hbook_html3/node94.html (accessed November 20, 2007).

[8] Commins, E. D., and P. H. Bucksbaum. *Weak interactions of leptons and quarks.* Cambridge University press, 1983.

[9] Duplancic, G., H. Pasagic, and J. Trampetic. "Rare $\Omega^- \to \Xi^0(1530)\pi^-$ decay in the Skyrme model." *Phys. Rev. D* 70 (2004): 077506.

[10] Finjord, J., and M. K. Gaillard. "Hyperon decays revisited." *Phys. Rev. D* 22 (1980): 778.

[11] Frodesen, A. G., O. Skjeggestad, and M. Tofte. *Probability and Statistics in Particle Physics.* Bergen: Universitetsforlaget, 1979.

[12] Goswami, D. N., and J. Schechter. "Theory of Ω^- decay." *Phys. Rev. D* 1 (1970): 290.

[13] D. Griffiths. *Introduction to elementary particles.* John Wiley & Sons, Inc., 1987.

[14] He, X. G., and G. Valencia. "$\Delta(I) = 3/2$ and $\Delta(S) = 2$ hyperon decays in chiral perturbation theory." *Phys. Lett.* B409 (1997): 469–473.

[15] James, F., and M. Roos. "Minuit: A System For Function Minimization And Analysis Of The Parameter Errors And Correlations." *Comput. Phys. Commun.* 10 (1975): 343.

[16] O. Kamaev. "Study of the decay $\Omega^- \to \Xi^-\pi^+\pi^-$ in the HyperCP experiment." *AIP Conf. Proc.* 842 (2006): 452–454.

[17] Kim, J., J. Lee, J. S. Shim, and H. S. Song. "Polarization effects in spin 3/2 hyperon decay." *Phys. Rev. D* 46 (1992): 1060–1063.

[18] Lee, T. D., and C. N. Yang. "General partial wave analysis of the decay of a hyperon of spin 1/2." *Phys. Rev.* 108 (1957): 1645–1647.

[19] Lu, L. C., and others. "Observation of parity violation in the $\Omega^- \to \Lambda K^-$ decay." *Phys. Lett.* B617 (2005): 11–17.

[20] Luk, K. B. *A study of the Ω^- hyperon.* Ph.D. thesis, FERMILAB-THESIS-1983-16, 1983.

[21] Luk, K. B., and others. "New measurements of properties of the Ω^- hyperon." *Phys. Rev. D* 38 (1988): 19–31.

[22] Lyons, L. *Statistics for nuclear and particle physicists.* Cambridge University press, 1986.

[23] Marshak, R. E., Riazuddin, and C. P. Ryan. *Theory of weak interactions in particle physics.* New York: Wiley-Interscience, 1969.

[24] Perkins, D. *Introduction to high energy physics.* Addison-Wesley publishing company, Inc., 1987.

[25] Pripstein, D., and others. "Search for flavor-changing neutral currents and lepton-family-number violation in two-body D0 decays." *Phys. Rev. D* 61 (2000): 032005.

[26] Rajaram, D., and others. "Search for the lepton-number-violating decay $\Xi^- \to p\mu^-\mu^-$." *Phys. Rev. Lett.* 94 (2005): 181801.

[27] Ravelo, G. J., and Q. A. Fontana. "Polarization in the non-leptonic weak decays of spin-3/2 hyperons." *Rev. Mex. Fis.* 48 (2002): 307–309.

[28] Sakurai, J. J. *Modern quantum mechanics.* Benjamin/Cummings publishing company, 1985.

[29] Solomey, N. "Ω^- hyperon decay modes with the HyperCP experiment at Fermilab." *Nucl. Phys. Proc. Suppl.* 115 (2003): 54–57.

[30] White, C. G., and others. "Search for $\Delta(S) = 2$ nonleptonic hyperon decays." *Phys. Rev. Lett.* 94 (2005): 101804.

[31] Wu, D., and J. L. Rosner. "Constituent quark description of nonleptonic hyperon decays." *Phys. Rev. D* 33 (1986): 1367.

[32] Yao, W. M., and others. "Review of particle physics." *J. Phys.* G33 (2006): 1–1232.

[33] Zech, G. *Comparing statistical data to Monte Carlo simulation: Parameter fitting and unfolding.* DESY-95-113, 1995.